Acoustic Imaging and Spectral Analysis for Assessing UAV Noise

I. Besnea

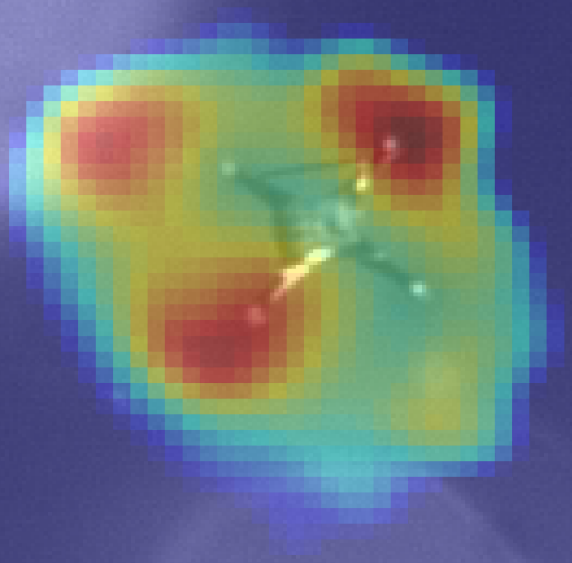

Technische Universiteit Delft

TU Delft

Acoustic Imaging and Spectral Analysis for Assessing UAV Noise

by

I. Besnea

to obtain the degree of
Master of Science in Aerospace Engineering
at the Delft University of Technology,
to be defended publicly on Tuesday April 7, 2020 at 15:00.

Prof. Dr. Dick G. Simons *Chair Holder*	Aircraft Noise and Climate Effects, Delft University of Technology
Dr. ir. Mirjam Snellen *Daily Supervisor*	Associate Professor, Aircraft Noise and Climate Effects, Delft University of Technology
Dr. Mihaela A. Mitici *Independent Member*	Assistant Professor Air Transport and Operations, Delft University of Technology

An electronic version of this thesis is available at http://repository.tudelft.nl/.

TU Delft

Preface

This report marks the end of my journey at TU Delft. I can say it was quite a rocky adventure full of ups and downs. However, I feel more confident than ever and I am now ready to tackle my next mission.

I would like to thank my daily supervisor Dr. Ir. Mirjam Snellen for offering me this engaging subject on drone noise and guiding me till the end. I would also like to thank Prof. Dr. Dick Simons for the feedback offered during the Green Light. Thank you, Ana, for your help with all the questions I had regarding multipoles and sound quality metrics. Thank you, Bieke and Max, for aiding me with the drone measurements at the windy military base in Den Helder.

I would like to thank my parents for supporting me every step of the way. Especially my mother for always keeping an eye on my health despite the physical distance between us.

Thank you, Roman, for never leaving my side even in my dreadful moments and always keeping me with my feet down to Earth. To Bieke and Claire, thank you for all the wonderful lunches and coffee breaks, and all the feedback and revisions given on my report.

Irina Besnea
Delft, March 2020

Executive Summary

With increasing Unmanned Aerial Vehicles (UAV) operations, tailored measures need to be implemented to integrate the massive employment of these vehicles in day-to-day operations. One of the current issues of UAVs is the noise emitted by these vehicles. The purpose of this research is to offer a doorway towards understanding the behavior of drone noise with changing operational and design parameters and to make way for the development of a drone noise prediction model. The radiated noise from four selected drones was experimentally measured under realistic environmental settings in an open field. The study dives through spectral analysis of a series of maneuvers, assesses the suitability of acoustic imaging algorithms for drone noise sources, explores adequate noise metrics, and lastly, identifies influential drone parameters essential for the modeling of drone noise in the future.

Spectrograms and power spectral density analyses unravel the frequency range of interest between 200 Hz to 3000 Hz. The spectral analysis in all cases has shown dominant harmonics of the blade passage frequencies of the rotors in this frequency range. Above this range, the ground reflection hinders the proper identification of noise sources. The frequency ranges are further investigated with four beamforming algorithms. As drone noise may exhibit complex radiation patterns due to interference of multiple rotors, sophisticated beamforming techniques (i.e. Functional, Dipole, and Quadrupole Beamforming) were implemented which are potentially superior to Conventional Beamforming in the setting of drone noise. The results of the beamforming algorithms have been verified with synthetic data. Notably, Functional Beamforming was found to perform best on a source if a correction for the expected source type is applied first, however, it is outperformed by other methods if the source type is not known *a priori*.

While all implemented algorithms yielded excellent results on synthetic data, their accuracy greatly decreases when applied to real-life data, which can be attributed to the multitude of external factors and imperfection in vehicle design, as well as the dependency of Dipole and Quadrupole Beamforming on prior information regarding the pole orientation on the rotors. Therefore, only Conventional Beamforming could be applied reliably. Analysis of Conventional Beamforming over snapshots of drones during different maneuvers shows that the rotors prove to be the main sources of noise in hovering and increasing height from Hover. The source identification, however, becomes unreliable with the non-static nature of the drone in the array plane (change in height).

To yield a complementary view on the sound characteristics of drones in specific maneuvers, the sound pressure levels and various sound quality metrics have been computed. The metrics reveal the effects of drone parameters (i.e. rotor size, distance to the observer, thrust settings, etc.), thus leading to a selection of possible candidates for a future noise model. This may be useful to assess the human psychoacoustic annoyance of drone noise in an environment where drones become a part of our everyday life.

List of Figures

List of Tables

Acronyms

Symbols

μUAV Micro UAV. 19, 34, 49–51

A

ACI Airport Council International. 1

B

BPF Blade Passage Frequency. 8, 39, 41, 42, 44, 45, 47, 50, 54
BVI Blade Vortex Interaction. 8, 9, 16
BWI Blade Wake Interaction. 8, 9, 16

C

CB Conventional Beamforming. 15, 23, 24, 30–38, 40, 43, 48, 52, 56
CSM Cross-Spectral Matrix. 24, 26

D

DAQ Data Acquisition System. 18
DB Dipole Beamforming. 25, 26, 29, 32–38, 52, 56
DFB Dipole Functional Beamforming. 32, 33, 35–38
DPL Dipole Characteristic Term. 25, 34

E

EASA European Union Aviation Safety Agency. 1, 67

F

FAA Federal Aviation Authority. 1
FB Functional Beamforming. 24, 30–38, 40, 48, 56
FWHM Full-Width at Half Maximum. 26

H

HSI High Speed Impulsive. 8, 9

L

LUAV Large UAV. 19, 20, 49–51

M

MTOM Maximum Take-Off Mass. 67
MUAV Medium UAV. viii, 19–21, 38–47, 49–51

N

NaN Not a Number. 20

P

PBL Power Band Level. 6
PSD Power Spectral Density. 6, 22, 43
PSF Point Spread Function. 14, 25
PWL Power Watt Level. 53

Q

QB Quadrupole Beamforming. 26, 29, 33–38, 52, 56
QFB Quadrupole Functional Beamforming. 33–37
QPL Quadrupole Characteristic Term. 29

R

RMS Root Mean Square. 13
RPM Revolutions Per Minute. 8, 41, 45, 50, 51, 53–55

S

SPL Sound Pressure Level. 6–8, 15, 16, 20–22, 24, 27, 30, 38, 44–47, 49–51, 53–55, 71
SUAV Small UAV. 19, 20, 37–42, 44–51

U

UAV Unmanned Aerial Vehicle. 5, 7–9, 15, 16, 19, 20, 30, 38, 40, 45, 46, 53–56, 67

List of Symbols

Latin Symbols

a	Radius of sphere $[m]$
B	Source Autopower $[Pa^2]$
c	Speed of Sound $[m/s]$
C	Cross-Spectral Matrix $[Pa^2]$
$\mathbf{d}$	Dipole Distance Vector $[m]$
$\mathbf{D}$	Quadrupole Distance Vector $[m]$
DI	Directivity Index
$Diam$	Rotor Diameter $[m]$
DPL	Dipole Characteristic Term
$\mathbf{f}$	Frequencies Vector $[Hz]$
FS	Fluctuation Strength $[vacil]$
FS_5	FS exceeded 5% of the time $[vacil]$
$\mathbf{g}$	Steering Vector $[1/m]$
g_{acc}	Gravitational Acceleration $[m/s^2]$
H	Absolute Humidity
I	Sound Intensity $[W/m^2]$
I_0	Reference Sound Intensity $(10^{-12}[W/m^2])$
k	Wave Number $[1/m]$
K	Tonality $[t.u.]$
K_5	Tonality exceeded 5% of the time $[t.u.]$
L	Array Aperture $[m]$
m	Mass of the UAV $[kg]$
M_t	Tip Mach Number
N	Overall Loudness $[sone]$
N_5	Loudness exceeded 5% of the time $[sone]$
$NFFT$	Number of sample points
N_f	Number of frequencies in the range
N_b	Number of blades per rotor
N_p	Number of propellers
N_s	Number of sources
$\mathbf{p}$	Acoustic Pressure $[Pa]$
$\mathbf{P}$	Vector of Complex Acoustic Pressures $[Pa]$
$\mathbf{p_e}$	Effective Sound Pressure $[Pa]$
p_{e0}	Reference Effective Pressure $(2 \times 10^{-5}[Pa])$
P_{br}	Propulsion Power of drone $[kW]$
PA	Psychoacoustic Annoyance
Q	Volume Velocity
QPL	Quadrupole Characteristic Term
$\mathbf{r_m}$	Distance to microphone array $[m]$
R	Roughness $[asper]$
R_5	Roughness exceeded 5% of the time $[asper]$
RL	Rayleigh Limit $[m]$
r_F	Fresnel Distance $[m]$
RH	Relative Humidity
s	Source Strength $[Pa]$
S	Sharpness $[acum]$
S_5	Sharpness exceeded 5% of the time $[acum]$
v_0	Surface Velocity Amplitude $[m/s]$
$\mathbf{w}$	Weight Vector
W	Acoustic Power $[W]$
W_0	Reference Acoustic Power $(10^{-12}[W])$
T	Length of the Signal $[s]$
$Temp$	Temperature $[K]$
TR	Thrust $[N]$
$\mathbf{U}$	Unitary Matrix of eigenvectors
V	Velocity $[m/s]$
z	Height of Source (Scan Grid Height) $[m]$

Greek Symbols

α	$\sqrt{(\mathbf{M}\cdot\mathbf{r}/r)^2+\beta^2}$
α_{atm}	Atmospheric Absorption Coefficient
β	$\sqrt{1-\lvert\boldsymbol{M}\rvert^2}$
γ	Coefficients of PA equation
Γ	Coefficients of Potential Noise Model
$\Delta\mathbf{t}$	Delay Vector [s]
η	Air Density Dependent Coefficient
θ	Angle of Radiation (with respect to noise source) [°]
λ	Wave Length $[m]$
ν	Beamforming exponential parameter
ξ	Grid Vector
ρ_∞	Air density
σ	Component of Matrix containing eigenvalues of CSM
Σ	Matrix containing eigenvalues of CSM
ω	Angular frequency = $2\pi f$ [rad/s]

Subscript

0	Reference
ν	Used ν parameter
av	Average
di	Dipole
h	Frequency index
i	Central
j	Scan grid point index
l	Source index
m	Microphone index
$mono$	Monopole
qua	Quadrupole

Superscript

*	Complex Conjugate Transpose

Contents

1 Introduction

Even a brief look over several drone-related news outlets and non-scientific article creators, as well as Federal Aviation Authority (FAA)'s reports on the number of drone sightings [1] shows a drastic increase of drone usage, from both a military and a civil point of view. This trend is supported by the statement *"Drone operations are expected to surpass the number of manned aircraft operations..."* by the Airport Council International (ACI) [2]. Despite the broad applicability of these vehicles, adjacent issues inevitably arise with the need for solid integration measures as it is a complex process that includes all points of view: legislative, environmental, operational and so on. For example, it was brought to light that drone noise can have an impact on human annoyance comparable to car traffic [3].

In the latest drone related conference hosted by the European Union Aviation Safety Agency (EASA), Amsterdam Drone Week in December 2019, it has been highlighted by EASA Executive Director Patrick Ky that *"We have had feedback from other countries around the world where there are regular drone operations that the concern of the population is not that much about privacy, is not that much about safety, but it's very, very much about noise"*[4]. Noise from these vehicles has clearly become a global issue in the matter of implementing daily operations over populated areas.

Unfortunately, very few studies have been published to date with regard to drone noise. In consequence, this research strives to bring forth elemental knowledge with respect to drones' sound behavior, spectra and sources of noise.

1.1. Research Objective

Analyzing the available state-of-the-art literature regarding drone noise uncovers a substantial lack of fundamental research. Existing studies work towards understanding each rotor element separately, while integrative analyses on drone noise as a whole has barely been done. Therefore, models which could be used to predict drone noise based on drone characteristics (number of rotors, blade passage frequency, etc.) are not available but highly desired. This study aims to gather pieces of the puzzle together and to fill the gaps by focusing on insights obtained from dedicated measurement campaigns.

The objective of this research is to set the fundamental understanding of drone noise. The spectrum of the noise and the behavior within different frequency ranges will be studied, and appropriate beamforming techniques will be used to determine the main sources of noise on the drone. The directivity of sound will be analysed and the appropriate metrics for this type of noise will be defined and explained. Lastly, the dependency of drone noise on varying operational (height, thrust, etc.) and design (number of rotors, weight, etc.) parameters is investigated. In conclusion, the aim of this thesis is to bring forth a detailed and complete analysis on drone noise behavior and serve as a starting point for future studies by suggesting appropriate analysis methodologies and appropriate metrics to quantify drone noise.

1.2. Research Structure

The research objective can be divided into the following research goals:

1. Explore spectral components of drone noise;

2. Investigate the dependency of noise levels as a function of several operational and design parameters;
3. Determine appropriate imaging algorithms;
4. Determine appropriate noise metrics;
5. Investigate potential key variables for a future drone noise prediction model.

Therefore, following the thesis' investigation scope, two main research questions, along with their sub-questions, arise. In this section, they will be presented in a logical order in which they must be answered chronologically. Thus, the first questions is:

What is the behavior of drone noise?

This is a fundamental inquiry for this research. Answering it is a crucial first step in developing a flexible model. Its adjacent sub-questions are:

- What are the main noise sources and their sound levels?
- What is the directionality of drone noise?
- Which flight parameters influence the noise levels and how do they influence the noise levels?

Knowing the noise levels of the main sources indicates the possible influence of an additional rotor (or of changes in the drone frame), while understanding the directionality sheds light on how to approach and regulate certain operational procedures (i.e. hovering, forward flight, descend and ascend) in the future. Naturally, these questions lead to the second set of queries.

What are suitable noise metrics to asses the impact of drones on human annoyance?

This question has the following adjacent sub-questions:

- Which metrics are suitable to assess drone noise?
- How can the annoyance of drone noise on human perception be quantified?

By the end of the study, the field will be supplemented with information regarding drone noise spectra, dependable parameters, suitable imaging and analysis techniques, and appropriate noise metrics. All in all, it will put the basics of a future model for the research to come. Thus, with the proper understanding combined with the metrics found from the main questions, investigations can proceed for assessing the overall impact on a bigger scale (i.e. surrounding airports, cities, etc.) and improve the current legislative measures (see Appendix B).

1.3. Report Structure

While modeling based on principles from physics is possible, such an approach might be out of reach to date. Therefore, a top-down approach is chosen, in which the focus is on measurements in order to understand noise characteristics. Nevertheless, it is important to have an understanding of the typical noise sources on drones before proceeding to measurements. Therefore, the theoretical background necessary for the research is introduced in chapter 2. This includes a description of commonly used drones, followed by a summary of sound quality and noise annoyance metrics which are used to quantify the results of the research. Afterward, the various multipole contributions to the complex radiation pattern of rotors are summarized and beamforming techniques are presented, which will be applied to drone noise.

Chapter 3 outlines the materials and methods used in the research. In the first part, the experimental set-up is illustrated. Measurements were taken with an acoustic array consisting of 64 microphones, allowing for acoustic imaging, where sources can be localized in space through beamforming. Both conventional and sophisticated beamforming algorithms are detailed, as well as the use of synthetic data for the validation of these aforementioned algorithms.

Subsequently, chapter 4 presents the relevant outcomes of the research. It starts by discussing the empirical development of Quadrupole Beamforming. Afterward, the outcomes of applying the beamforming techniques to synthetic data are illustrated. Next, the results of applying the beamforming algorithms to

real-life measurements are presented and thus, the sources of noise on the drones are determined. In the following part, the variation in noise levels with changing angle and distance is assessed. Lastly, the common values of the sound quality metrics for different operations and drones are exhibited.

Lastly, the report finalizes with chapter 5 dedicated to discussing appropriate modeling parameters for drone noise, summarizing the conclusions and offering a set of recommendations and outlooks.

2

Theoretical Background

Throughout this chapter, the required supporting concepts will be explained along with their applicability to the purpose of the research. First, the process behind selecting the drone type of interest is clarified. Afterward, the commonly mentioned and discussed metrics are briefly introduced as they will be used to quantify the results of the analysis. The reasoning behind the need for imaging techniques is described alongside the main findings from the supporting literature regarding rotor noise.

2.1. Unmanned Aerial Vehicles of Interest

An Unmanned Aerial Vehicle (UAV), also known as a drone, is an aircraft without human pilots on board, as its name suggests. Drones are usually classified by either type or size. This section dives into these details and concludes with the selection of the UAVs of interest for the research.

When distinguishing drones by type, the lift generating system is the defining aspect. Thus, UAVs can be Fixed-Wing, Hybrid or Rotary (see Figure 2.1).

(a) Fixed-Wing [5] (b) Hybrid [6] (c) Rotary [7]

Figure 2.1: Types of Drones

A fixed-wing UAV makes use of sturdy wings in combination with forward speed to generate lift, in a similar fashion to the conventional airplane, while rotary UAVs make use of rotary wings to generate lift, similarly to helicopters. Both fixed-wing and rotary drones have certain advantages. For example, rotary drones do not need a landing-strip and can hover in the air. However, fixed-wings fly faster, have a larger operating range and are less noisy. Hybrid Drones try to take the best of both worlds (i.e. they take-off and land vertically, but also fly greater ranges), by using a combination of fixed planar wings and vertical fans. Since both hybrid and fixed-wing UAVs are not readily available to the common civil user, it appears that in the future, Urban Air Mobility will mostly make use of multi-rotor drones. Thus, only the latter is taken into consideration for this study.

From a size point of view, UAVs are segmented into the categories of Table 2.1. This type of categorization is predominantly specific to the multi-rotors.

The most widely used types of drones are small and medium four-rotor UAVs (also known as quadcopters). Most studies and publications assess quadcopter capabilities. In addition, the available UAVs for this thesis' measurements are mainly quadcopters. For these reasons, this type of drone will be the main interest for the rest of the report and the measurements were performed using such vehicles.

Classification	Weight [kg]	Application
Micro	< 5	Recreational Purposes and Sport
Small	5 - 10	Filming and Photography
Medium	50 - 200	Carry Professional Cameras and Small Parcels
Large	200 - 2000	Heavy Cargo
Supersize	> 2000	Human Transportation and Heavy Cargo

Table 2.1: Drones Classified by Size and Their Corresponding Applicability

2.2. Noise Annoyance Metrics

There is a multitude of methods to quantify the effect of noise. Next to the commonly used Sound Pressure Level (SPL), several metrics such as loudness, roughness, tonality, fluctuation strength and sharpness were proposed to describe the noise of a quadcopter [8, 9]. Each of these metrics is designed to illustrate certain spectral characteristics of sound, thus, they are called "Sound Quality Metrics". This section will describe each of these quantities, while an in-depth mathematical description is out of the scope and dives too deep into the Psychoacoustics field for this introduction. The Sound Quality Metrics in this thesis are calculated using the Audio Assessment Module described in [10]. The majority of the module metrics are expressed as "exceeded 5% of the time" (the value which is exceeded only 5% of the total recorded time) as this value offers a reasonably good measure of human perception [11].

A basic and objective way of expressing the sound level of an acoustic signal is through the Sound Pressure Level (SPL) [12]. This metric will predominantly be used throughout the study. The values are expressed in decibels (dB). The definition of the SPL in the time domain is:

$$\text{SPL} = 10\log_{10}\frac{p_e^2}{p_{ref}^2} \tag{2.1}$$

where the reference pressure p_{ref} is equal to $2\times10^{-5}\ Pa$, the pressure at the threshold of the human ear [12], and p_e is the effective sound pressure, computed from the time series of recorded pressure values

$$p_e^2 = \sqrt{\sum_{t=1}^{T} p(t)^2}, \tag{2.2}$$

where T denotes the number of data points in a given time chunk.

In case the SPL is calculated over the whole beam-width of frequencies, it is denoted as the Overall Sound Pressure Level (OSPL),

$$\text{OSPL} = 10\log_{10}\left(\frac{p_e^2}{p_{ref}^2}\right) \tag{2.3}$$

When calculated from the signal in the frequency domain (in octave bands), the expression is:

$$\text{OSPL} = 10\log_{10}\sum_{i=1}^{n} 10^{\text{SPL}(f_i)/10} \tag{2.4}$$

where f_i is the center frequency of the 1/3-octave band and $SPL(f_i,\theta)$ is the corresponding Power Band Level (PBL) of the frequency band. The PBL can be determined per frequency band as:

$$\text{PBL}(f_i) = \text{SPL}(f_i) = 10\log_{10}\left[\frac{PSD(f)\Delta f}{p_{e0}^2}\right] \tag{2.5}$$

where Δf is the difference between the upper and lower bounds of the frequency bands and $PSD(f)$ is the Power Spectral Density (PSD) measured in Pa^2/Hz. The PSD is equal to $\frac{|P(f)|^2}{T}$ where $P(f)$ is the Fourier Transform of the signal and T is the length of the signal. The PSD plotted over the frequency range portrays the so-called spectra of the sound. This type of plot will be predominantly used in the results chapter (chapter 4).

2.2.1. Overall A-weighted Sound Pressure Level

Non-linear frequency selectivity of the ear plays an important role in loudness metrics. The A-weighted metric was developed to approximate the fact that the human hearing system perceives high frequency sound as louder than the low-frequency sound of the same SPL [12]. When assessing noise, higher frequencies are weighted more heavily than low frequencies. This weighting factor is defined as [12]:

$$\Delta L_{\mathrm{A}}(f_i) = -145.528 + 98.262 \log f_i - 19.509 (\log f_i)^2 + 0.975 (\log f_i)^3 \tag{2.6}$$

where f_i is the center frequency of the 1/3-octave band. $\Delta L_{\mathrm{A}}(f_i)$ is applied to the $SPL(f_i)$, the corresponding Power Band Level of the frequency band, and the Overall A-weighted SPL is calculated in logarithmic scale [dBA] as:

$$\mathrm{OASPL} = 10 \log_{10} \sum_{i=1}^{n} 10^{\frac{\mathrm{SPL}(f_i) + \Delta \mathrm{L_A}(f_i)}{10}} \tag{2.7}$$

As mentioned before, this metric is important as it best resembles the human perception of noise. Thus, it will be predominantly used throughout the results section in combination with the other sound quality metrics for comparison.

2.2.2. Loudness (N)

Loudness is the subjective perception (i.e. cannot be measured directly) of the magnitude of a sound and it is a function of intensity, frequency and duration [13]. Studies such as [14] and [15] worked on experiments with human subjects and focused on Loudness. The levels are usually defined in *phon* on the logarithmic scale and *sone* on the linear scale. For non-stationary sounds, average loudness is not the best measure of how subjects will perceive the noise, because it does not exemplify how subjects will rate the overall loudness of a time-varying sound [16]. For many sounds where loudness varies with time, it has been found that the *"Loudness exceeded 5% of the time"*(N_5) often is a reasonably good measure of perceived loudness. The latter is also used in the description of the results (as in the case of the rest of the sound quality metrics).

2.2.3. Sharpness (S)

A sound is considered sharp if it has more high rather than low frequency content. Therefore, Sharpness (or Spectral Balance) gives higher frequencies more weight than lower frequencies in a normalized calculation to predict the frequency location of the center of the loudness spectrum. A narrow band noise with 1 kHz center frequency, 160 Hz bandwidth, and a SPL of 60 dB would produce a Sharpness of 1 *acum*, the unit of measure for sharpness [11]. Simply, it can be said that a high frequency noise is sharp, while a low frequency noise is not.

2.2.4. Roughness (R)

Roughness (measured in *asper*) is perceived for sounds with rapid loudness fluctuations (15 to 300 Hz). By definition, a tone with a center frequency 1 kHz, sound pressure level 60 dB and a 100% amplitude modulated at 70 Hz, produces a Roughness of 1 *asper*. For a tone with a frequency of 1 kHz or above, the maximal roughness of a tone is found to be at a modulating frequency of 70 Hz. For frequencies below 1 kHz, the maximal roughness is found to be at increasingly lower modulation frequencies [11].

2.2.5. Fluctuation Strength (FS)

In contrast to Roughness, the Fluctuation Strength represents the perceived strength of slow fluctuations in loudness (up to 20 Hz after which Roughness takes over). The unit of measure is *vacil* which is produced by a tone with sound pressure level 60 dB, 1 kHz center frequency and with a 100% amplitude modulation at 4 Hz (maximum perception) [11].

2.2.6. Tonality (K)

Tonality is concerned with the presence or absence of tones of a sound [11]. This metric is quantified using several types of equations and methods, however, the Audio Assessment Module makes use of Aures' tonality. A reason for this is because in the case of sounds that include a harmonic series of tones with a low fundamental frequency, i.e. buzz-saw noise, only Aures' tonality metric is capable of capturing it [10]. Tonality is of great importance when discussing UAV noise due to it being generated under the periodic motion of the propellers. The results in this thesis are expressed in *tonality units [t.u.]*.

2.2.7. Psychoacoustic Annoyance (PA)

The Psychoacoustic Annoyance expresses the overall human annoyance response to certain sounds [11]. It has been developed through empirical means and integrates the aforementioned sound quality metrics into an overall score of the annoyance (see Equation 2.8).

$$PA_{mod} = N_5(1 + \sqrt{\gamma_0 + \gamma_1 w_s^2 + \gamma_2 w_{FR}^2 + \gamma_3 w_T^2}) \tag{2.8}$$

where N_5 is the Loudness exceed 5% of the time and w_s, w_{FR} and w_T are the weighting factors corresponding to Sharpness (Equation 2.9), Roughness and Fluctuation Strength (Equation 2.10), and Tonality (Equation 2.11), respectively.

$$\begin{gathered} w_s = 0.25(S - 1.75)\log_{10}(N_5 + 10) \text{ for } S > 1.75 \\ w_s = 0 \text{ for } S < 1.75 \end{gathered} \tag{2.9}$$

$$w_{FR} = \frac{2.18}{(N_5)^{0.4}}(0.4FS + 0.6R) \tag{2.10}$$

$$w_T^2 = \left[\left(1 - e^{-\gamma_4 N_5}\right)^2 \left(1 - e^{-r_s K_s}\right)^2\right] \tag{2.11}$$

S, FS and R denote the Sharpness, Fluctuation Strength, and Roughness, respectively. K_5 is the Tonality exceeded 5% of the time and the γ coefficients are used to fit the model results to subjective annoyance ratings from the Audio Assessment Module [10].

2.3. Rotor Noise

Knowledge about the basic components of rotor noise is important since the main lift system for our drones of interest are rotors. Throughout this section, the basic noise source components and propagation directivity of rotors will be described in depth. Related experimental research on rotor noise, although scarce, manages to give an initial overview of how certain design parameters influence the power of the emitted noise. This section will also present an overall summary of how rotor characteristics change the emitted sound pressure levels and how this can be used in the thesis research. In general, rotors suffer from similar trade-offs between the efficiency of flight and noise as for any type of aerial vehicle. Whatever improvements are done to increase flight performance will entice an increase in the SPL values. For example, a bigger rotor diameter would result in higher efficiency of flight but also increased noise.

With regards to the number of blades per rotor, in general, the higher the number, the higher the Blade Passage Frequency (BPF), f_1, according to [12]:

$$f_1 = N_b \frac{RPM}{60}, \tag{2.12}$$

where N_b is the number of blades per rotor and RPM the Revolutions Per Minute of the rotor. Since higher frequencies are better subjected to atmospheric attenuation (see Appendix D), the overall levels of noise are expected to be lower than in the case of fewer blades per rotor.

Another recurring conclusion throughout the literature concerns the frequency range. It has been observed that usually rotor noise is dominant for frequencies from 200 to around 3000 Hz. This statement was tested with the experimental measurements of this research (section 4.3).

Noise originating from rotors can be divided into sound coming from the electric motor (usually observable at high frequencies) and the rotor noise (Figure 2.2). Nowadays, rotary UAVs are equipped with silent motors, in such a way that this component can be considered insignificant in comparison to the propeller noise. The latter can be categorized in broadband and tonal noise. Broadband noise is created by random fluctuations of the forces on the blade, caused by turbulence. The most prominent example is the trailing-edge noise (also called broadband self-noise). Broadband noise prediction is difficult due to the complexity of the turbulent nature of the noise source.

Tonal noise is related to thickness, loading, Blade Vortex Interaction (BVI), Blade Wake Interaction (BWI) and High Speed Impulsive (HSI) noise.

The aforementioned noise sources do not emit equally strong in all directions. Figure 2.4 presents this directivity in relation to the rotor orientation.

Thickness noise is significant in hover and forward flight [18], propagates along the rotor disk plane (Figure 2.4) and is mainly caused by the fluid displacement (Figure 2.3(a)). Loading noise is radiated in directions

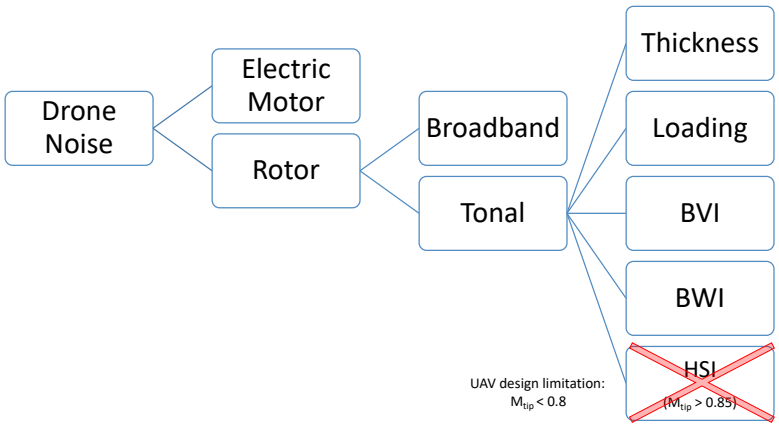

Figure 2.2: The noise generated by a drone is generated by either the electric motor system or the rotors. From theory, rotor noise is also composed of broadband and tonal noise components such as Thickness, Loading, BVI, BWI and HSI.

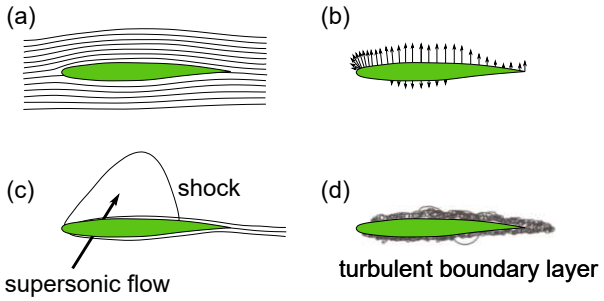

Figure 2.3: Generation of Noise Components on a Blade as adapted from [17]: a) In the case of Thickness noise, b) For Loading Noise, c) For HSI and d) For Broadband Noise

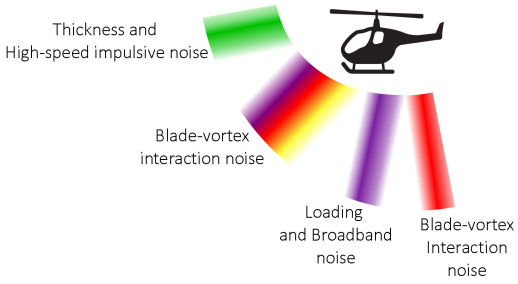

Figure 2.4: Noise components direction of propagation with respect to the drone (Note: Colors are used for a better understanding of the direction of propagation. They however, do not represent anything specific)

perpendicular to the propeller plane, being dominant in the hemisphere under the propeller (Figure 2.4) and is caused by an acceleration of the force distribution on the fluid as the blade passes (Figure 2.3(b)). BVI noise is a significant source of noise in descent and hover flights since it is generated by the interaction of the shed tip vortex with the following blade, while the BWI noise occurs due to the turbulent wake of a previous blade interacting with the next one (Figure 2.4). High Speed Impulsive (HSI) noise appears in trans-sonic flight conditions with advancing tip Mach numbers above 0.85. It is physically generated by shock waves in the flow field around the rotor (Figure 2.3(c)) and it propagates in all directions along the rotor disk plane (Figure 2.4). However, it is a known design restriction that UAVs must not exceed tip Mach number values of 0.8, thus removing HSI noise from the scope of this thesis [19].

In reality, each blade of each rotor contributes a monopole, dipole and quadrupole term to the total radiated noise. Those single sources are, however, not distinguishable on such small vehicles as drones. In consequence, with assumptions extracted from helicopter and rotor noise publications [20],[21],[18], this

thesis treats each rotor as the superposition of one mono-, di- and quadrupole as depicted in Figure 2.5.

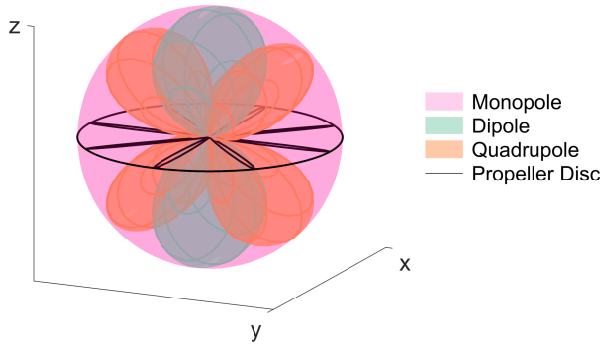

Figure 2.5: Simplified Illustration of the Monopole, Dipole and Quadrupole Distribution on a Propeller. The Monopole (pink) has an omnidirectional propagation, the Dipole (light blue) with a cosine propagation along the Z axis, and the Quadrupole (orange) has a $\sin\theta\cos\theta$ direction of propagation

2.3.1. Monopole

By definition, a monopole is a point noise source which radiates equally in all directions (see Figure 2.6). It is the simplest type of source and it stands as a build-up component for more complex types, such as dipoles and quadrupoles.

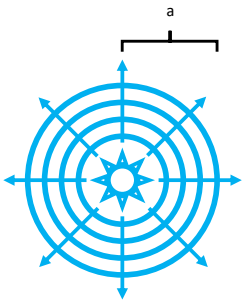

Figure 2.6: Monopole Geometry (where a defines the radius of the source sphere)

In order to express the pressure field of a such source, first, the difference between the near- and far-field will be described. In far-field, a point source can be defined by $ka \ll 1$ where a is the radius of the source sphere and k is the wave-number equal to $\frac{2\pi f}{c}$, with f the frequency in Hz and c the speed of sound in m/s. Simply stated, a source takes the form of a point source if it is sufficiently far away or sufficiently small. Figure 2.7 visualizes the sound wave arriving from a monopole source to a microphone array in both near -and far-field. The spherical wave can be approximated as a planar wave in the latter case and spherical spreading does not have to be taken into consideration anymore. This far-field approximation is also called the 'Fraunhofer approximation'. To make a proper distinction of when the switch is made between near- and far-field, the Fresnel distance must be calculated (Equation 2.13 with f the frequency, L the aperture of the array and c the speed of sound). This value serves as a boundary limit which, if not exceeded, the acoustic wave cannot be considered planar (thus the Fraunhofer approximation cannot be applied) [12].

$$r_F = \frac{fL^2}{c} \tag{2.13}$$

Considering these concepts, the generalized expression for the radiated pressure p of this noise source in far-field takes the form [12]:

$$p(r,t) = i\frac{Q\rho_\infty ck}{4\pi r}e^{i(\omega t - kr)} \tag{2.14}$$

where i is the imaginary number, $Q = 4\pi a^2 v_0$ is the product of the surface area and the surface normal velocity amplitude, ρ_∞ is the air density, r is the distance to observer, θ is the angle of observation, ω is the

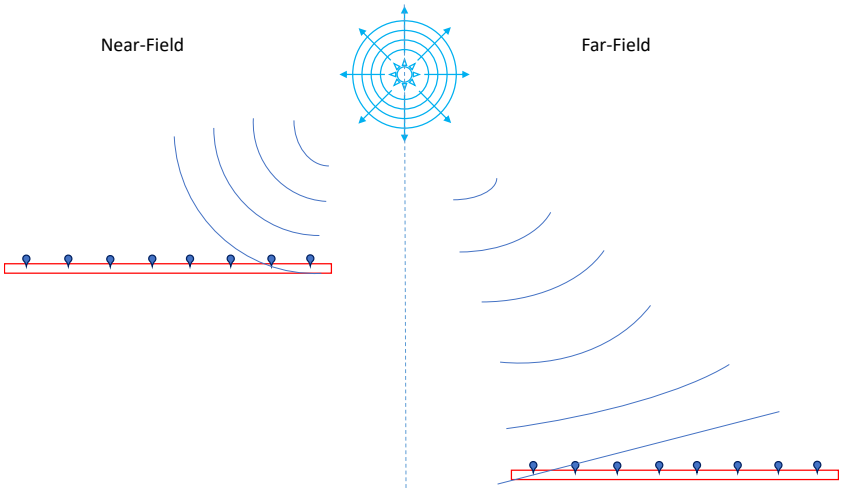

Figure 2.7: Comparison of a wave geometry for near (left) and far-field (right) delimited by the dotted vertical line. The blue curved lines represent the propagation of the sound wave. In the near-field case, the curvature of the waves is still significant until the moment of reception. In the case of far-field, the waves are considered as planar at the reception instance.

frequency, $k = \frac{\omega}{c}$ is the wave number and t denotes time. The magnitude (amplitude) of the pressure is the real part of Equation 2.14.

$$|p(r,t)| = \frac{Q\rho_\infty ck}{4\pi r} \tag{2.15}$$

For plane waves, $I(r) = \frac{|p|^2}{2\rho_\infty c}$ [12] and it is known that $p_e^2 = \frac{|p|^2}{2}$, so the acoustic intensity of the monopole becomes [12]:

$$I(r) = \frac{\rho_\infty c}{32\pi^2}\left(\frac{Qk}{r}\right)^2 \tag{2.16}$$

The radiated sound power is equally distributed over the surface of a sphere with radius r (thus $W = 4\pi r^2 I$) such that the radiated sound power (amount of sound energy emitted per unit time) of a monopole becomes [12]:

$$W = \rho_\infty c\frac{Q^2k^2}{8\pi} = \frac{\rho_\infty Q^2\omega^2}{8\pi c} \Rightarrow W \sim \omega^2 \tag{2.17}$$

For a fixed Q, the power thus varies with the square of the frequency [12].

2.3.2. Dipole

By definition, a dipole source is comprised of two monopole sources of equal strength but opposite phase [12], positioned at a small distance d from each other (Figure 2.8a) which satisfies the relation $kd \ll 1$.

The total sound pressure is described in the far-field, i.e. assuming that the two lines connecting the monopoles and the observation point (the two purple arrows in Figure 2.8a) can be considered parallel. In addition, the weak dependence of the amplitude of the sound pressure on the position of the monopoles is ignored. The phase difference, however, cannot be ignored [12].

Thus, with θ being the angle between the dipole axis and the line connecting the dipole and the observation point in the direction of the purple lines, the total sound pressure is given as [12]:

$$p(r,\theta,t) = i\frac{Q\rho_\infty ck^2d}{4\pi r}\cos(\theta)e^{i(\omega t-kr)} \tag{2.18}$$

The magnitude takes the form [22]:

$$|p(r,\theta,t)| = \frac{Q\rho_\infty ck}{4\pi r}kd\cos\theta \tag{2.19}$$

Knowing the pressure, the intensity of the dipole reads [12]:

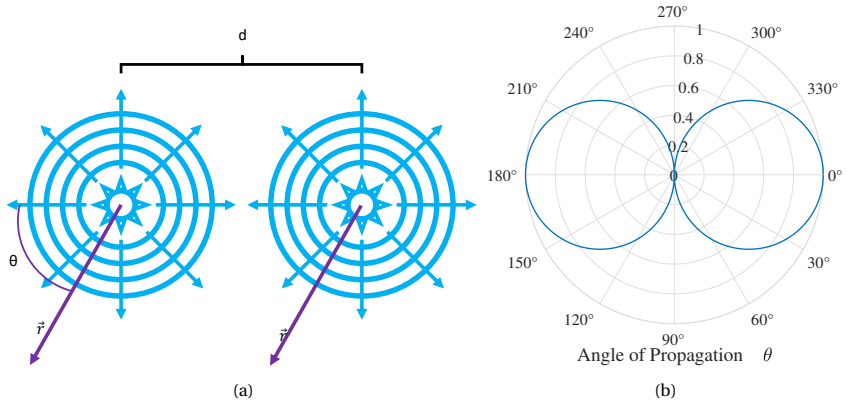

Figure 2.8: Dipole Geometry (a) with the poles (blue) placed at a distance $\boldsymbol{d}$ with respect to each other. The direction of observation is visualized by the purple arrows positioned at angle θ from the dipole axis (in direction of vector $\boldsymbol{d}$). Its radiation pattern follows the shape in (b).

$$I(r,\theta) = \frac{|p|^2}{2\rho_\infty c} = \frac{\rho_\infty c Q^2 k^4 d^2 \cos^2\theta}{32\pi^2 r^2} \tag{2.20}$$

The radiation pattern (i.e. acoustic intensity as a function of angle) follows a $\cos^2\theta$ dependence. Normal to the dipole axis ($\theta = 90°$, and 270°) the sound pressure is zero (see Figure 2.8b).

Finally, the total radiated power of the dipole varies with the frequency to the fourth power [22]:

$$W = \frac{\rho_\infty Q^2 \omega^4 d^2}{24\pi c^3} \Rightarrow W \sim \omega^4 \tag{2.21}$$

In summary, the dipole pressure field is related to the monopole pressure field as:

$$p_{di} = p_{mono} kd \cos(\theta) \tag{2.22}$$

Since the dipole derivation stands for $kd \ll 1$, the dipole strength is lower than that of two separate monopoles.

2.3.3. Quadrupole

A quadrupole source consists of two dipole sources of equal strength but of opposite phase, obtaining the geometry of four monopoles with alternating phase at the corners of a rectangle (Figure 2.9a).

These monopoles are separated by distances d and D (Figure 2.9a), which are both small compared to the wavelength (in this study's case). With θ the angle as indicated in the figure, the far-field total sound pressure of the quadrupole is given by [12]:

$$p(r,\theta,t) = i\rho_\infty c \frac{Qk^3}{8\pi r} dD \sin(2\theta) e^{i(\omega x - kr)} \tag{2.23}$$

The magnitude is [22]:

$$|p(r,\theta,t)| = \frac{Q\rho_\infty ck}{4\pi r} k^2 dD \cos\theta \sin\theta \tag{2.24}$$

The directional radiation pattern (Figure 2.9b) now follows a $\sin^2(2\theta)$ dependence, so in the directions $\theta = 0°, 90°, 180°$ and 270° the sound pressure is zero. Furthermore, the radiated intensity of the source is:

$$I(r,\theta) = \frac{|p|^2}{2\rho_\infty c} = \frac{\rho_\infty c Q^2 k^6 d^2 D^2 \sin^2(2\theta)}{128\pi^2 r^2} \tag{2.25}$$

The total radiated power of the quadrupole depends on the 6^{th} power of the frequency [22]:

$$W = \frac{\rho_\infty Q^2 \omega^6 d^2 D^2}{60\pi c^5} \Rightarrow W \sim \omega^6 \tag{2.26}$$

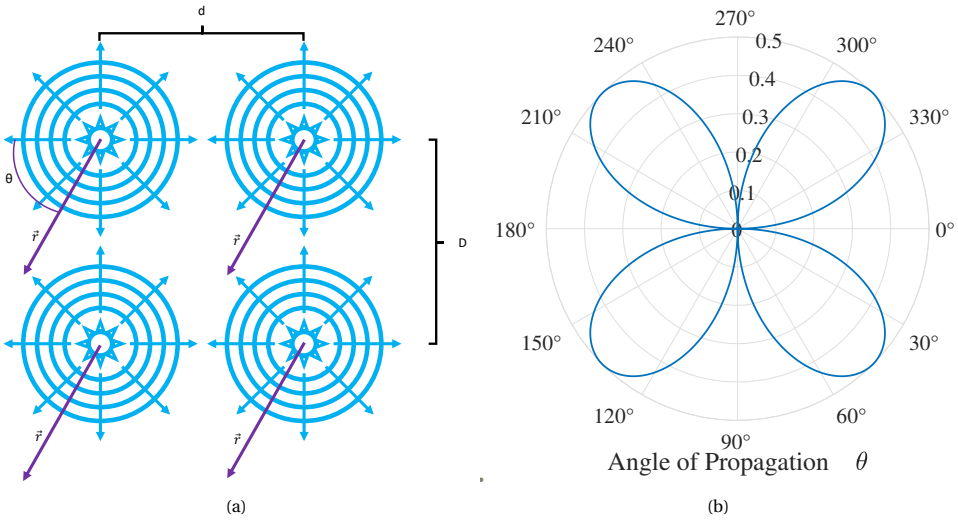

Figure 2.9: Quadrupole Configuration (a) with the poles (blue) placed at a distance ***d*** (horizontally) and ***D*** (vertically) with respect to each other. The direction of observation is visualized by the purple arrows positioned at angle θ from the quadrupole plane (defined by vectors ***d*** and ***D***). Its radiation pattern follows the shape in (b).

In conclusion, the quadrupole pressure depends on the monopole pressure field as:

$$p_{qua} = p_{mono} k^2 dD \cos(\theta) \sin(\theta) \tag{2.27}$$

The quadrupole is, thus, an even less efficient radiator of noise as compared to the dipole and monopole [22].

2.4. Imaging Techniques

One important purpose of this research is to determine the exact sources of noise and their amplitudes with the correct location on a multi-copter structure. A common approach is using imaging techniques such as beamforming.

Beamforming is a common method of spatial filtering through signal processing, which makes use of either time delays (time-domain beamforming) or phase differences (frequency domain beamforming) in signal wave arrivals at the sensors [23]. This most basic beamforming technique is Delay-and-Sum. Given a scan grid of points at the height of the source, the delay from each grid point to the sensors (i.e. microphones) is computed. The signals are then corrected for these delays and summed. This is done for all grid points. In case a source is present at a certain grid point, delay-and-sum will result in the signals for all microphones adding up constructively. This is theoretically the true location of the source. A more explicit visualization of this process is shown in Figure 2.10, along with the following steps [24]:

1. The sound of each source arrives at the receivers along different paths.

2. The signals caught by the receivers are comparable in waveform, however, they show different arrival times, proportional to the traveled distances. The delays can be resolved from the speed of sound, the separation between the receivers, and the sound sources.

3. In Figure 2.10, the Beamformer focuses on where source 1 (in red) is located. The signal of every receiver is delayed by accounting for the travel times per grid point. Thus, the signal components of source 1 in all channels are in phase, whereas the signal components originating from source 2 (blue) remain out of phase.

4. The delayed signals of all channels are summed and lastly, the total signal is standardized by the number of receiver channels. The amplitude of the signal component of source 1 in the summed signal is as strong as the first amplitude of source 1 and the signal components from source 2 are negligible. The Root Mean Square (RMS) or maximum value can be computed from the time signal and depicted in the acoustic map.

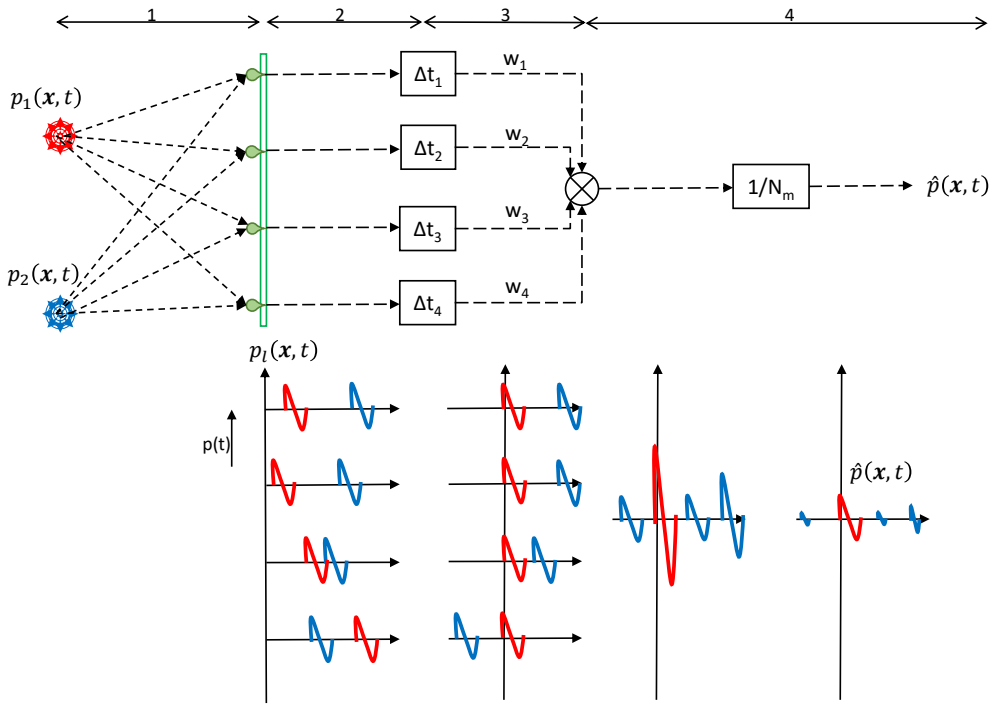

Figure 2.10: Beamforming Delay-and-Sum Method as adapted from [24]. Source 1 (p_1) is colored red, Source 2 (p_2) is colored blue and the microphone array is green. This illustration depicts the steering at the location of Source 1

The acoustic image obtained when a source is present is called Point Spread Function (PSF). Taking all the microphone signals and summing them up will result into levels specific to each individual point of the scan grid (see Figure 2.11). With the source above the measuring array, constructive interference occurs and thus the same result would be present if beam-steered (i.e. applying the appropriate microphone delays) towards the source located exactly above the array. With beam-steering, the focus can be shifted around the scan grid of points on a desired location. The shape in Figure 2.11 presents a main lobe and side lobes as the source resembles a first order Bessel Function. To increase clarity, these lobes can be manipulated. For example, the main lobe width can be reduced by either increasing the dimensions of the array, or by beamforming at higher frequencies. On the other side, the myriad of side lobes can be reduced by increasing the number of microphones.

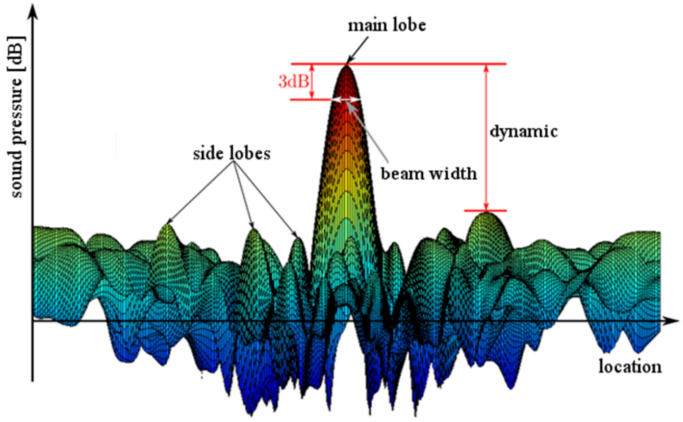

Figure 2.11: Visualization of the PSF and the resulting beamformer pattern of a single source, with indicated components, such as side lobes and main lobes [25]. The concepts of beam-width and dynamic range are also represented. The first is the broadness of the main lobe corresponding to the amplitude 3dB below the maximum. The latter is the difference between this maximum peak and the highest side-lobe.

In conclusion, beamforming is a common imaging technique used in aviation for aircraft flyovers, landings, or takeoffs. However, a question emerges: will it be easily applicable to UAV operations, considering the change of a multitude of factors? UAVs have random trajectories and are operating at much lower heights than aircraft. In addition, considering the diverse types of noise sources present on the rotors, will this affect the imaging performance? Conventional Beamforming (CB) techniques are designed to locate and determine the amplitudes of the monopole, and less those of dipoles and quadrupoles.

The performance of CB on both a monopole source and a dipole source can be observed in Figure 2.12. In the illustration, both a monopole and a dipole source were created and their position was moved along the surface of a sphere. Thus, the distance to the microphones stays constant, while the angles of observations vary. The illustration shows the cases of overhead position (at 90°), 60°, 45° and 30°. In the case of the monopole source, CB performs well and its omnidirectional behavior is observable as it does not vary the emitted strength with varying angle of observation. The apparition of side-lobes in the 30° case may be due to the assumed microphone array geometry and its resolution limitations. In the case of a dipole (constructed with its poles along the z-axis, directed in the paper plane), approximately 1dB decay is observed with decreasing angle. This can be explained by the cosine directivity of the dipole. In this example, the directivity of the dipole's radiation pattern cannot be observed due to its constant orientation along the z-axis. The same side lobes are present in the case of 30°, as in the monopole case, however, these are not observable due to the selected dynamic range.

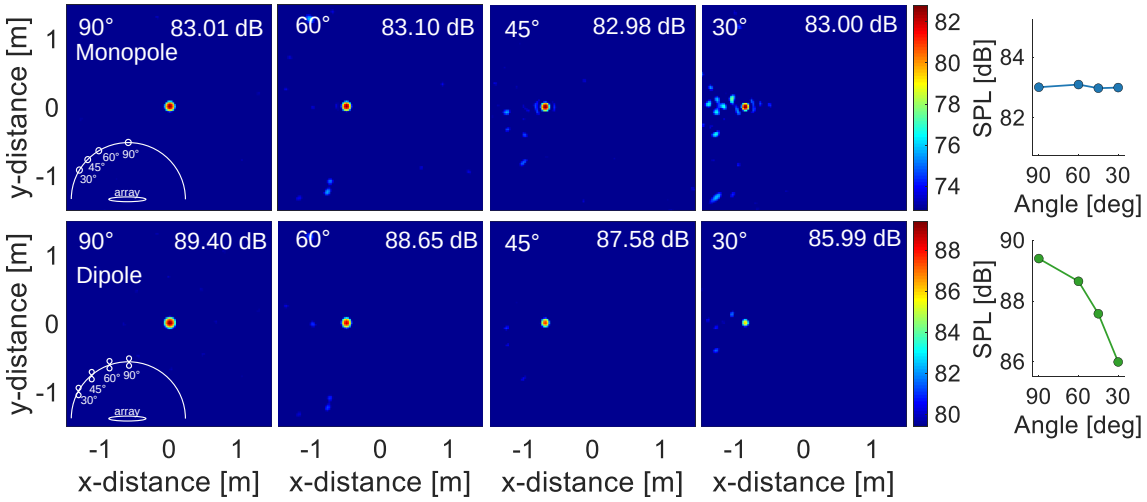

Figure 2.12: Comparison of of the performance of Conventional Beamforming on a monopole source (above) and a dipole source (below) for various angles of observation (90°, 60°, 45° and 30°). Maximum SPL over Angle is shown on the right side.

The purpose of the beamforming algorithm is to correct for the angle and output the correct strength of the source. With the correct beamforming technique applied, the output for the dipole should be as accurate as possible, regardless of the angle of observation. Hence, this research strives to investigate the performance of this technique, and if possible develop an augmentation to the algorithms to allow for dipole and quadrupole analysis. These augmentations will be detailed in the first part of the results chapter (section 4.1).

2.5. Concluding Remarks and Outcomes of the Literature Study

In summary, this chapter brought forth the basic concepts of this study. The multi-copters of interest have been defined, the commonly expressed metrics have been exemplified, to allow for comparisons later on. The main noise sources of rotors have been explained due to their relation to the issue of multi-copters and might present a good starting point for the research. Lastly, the noise location matter is solved through imaging techniques. However, their efficiency will be investigated and rectified.

From rotor noise-related literature, the following reoccurring patterns have been observed:

- The frequency range on which UAVs manifest noise is low, between 300 and 2000 Hz [26].
- The angle of observation (θ) is very important in describing rotor noise and it is dominant in the underside hemisphere of the rotor (direction of loading noise propagation) [27].

- Counter-rotating rotors (as in the case of drones) have been discovered to generate around 2dB more noise than the co-rotary propellers. This is probably due to enhanced interference, and BVI and BWI noise [28].
- Face-to-face rotors (as in the design of some multi-rotors - i.e. Neo octocopter) present higher noise levels than zero tilt or back-to-back cases. This is due to the extended range of noise when discussing angles of observation [28].
- The bigger the separation between the propellers or between propellers and supporting arm/body, the lower the SPLs. This is most likely due to less interference, and BVI and BWI noise [29].
- The SPL increases with the number of rotors, blades, thrust power, rotor diameter, and rotational speed, as all these parameters determine the same effect of lift gain (and thus drag gain as well). Thus, with regards to design, there will always be a trade-off between noise and efficiency of flight [28].
- A typical noise value for an UAV has not been determined as this can differ substantially from model to model, depending on the size, number of rotors and other design and operational parameters.

3

Materials and Methodology

This chapter will bring forth the methods and materials used in the research analysis and the motivation behind their application.

3.1. Experimental Set-Up

A series of measurements have been performed on two separate occasions. The first series of measurements were taken in TU Delft's Cyberzoo on the 2nd of May 2019. On the 10th of September 2019 at the Naval Military Base of Den Helder a second series was performed. The same measurement equipment was used on both occasions (microphones, array panels, acoustic and optical cameras, laptops). However, different drones were flown each time.

3.1.1. Measurement Equipment

A simplified set-up of the equipment is shown in Figure 3.1a. The drone flies above the microphone array which is installed upon 16 wooden panels with suspension legs and topped with absorbent foam. The purpose of the foam is to prevent any possible reflections from the surface of the wooden panels. The overall area of this wooden structure is 4 by 4 meters.

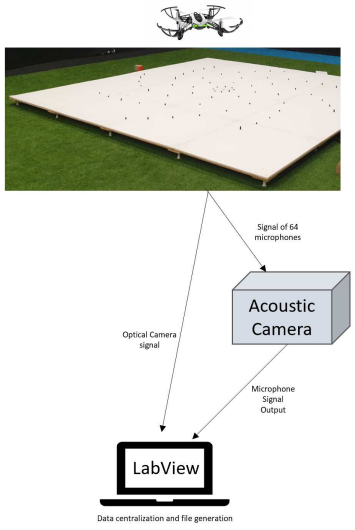

(a) Equipment Set-Up

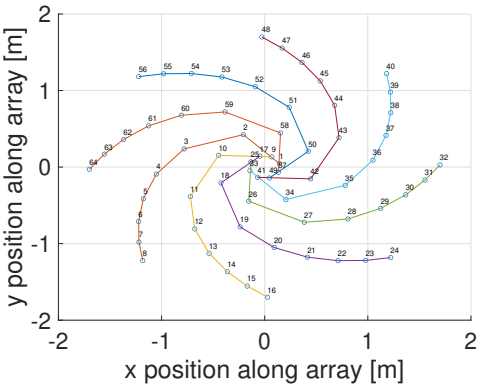

(b) Experimental Microphone Array

Figure 3.1: Equipment used in the Measurements. (a) A simplified illustration of the experimental set-up: The drones will fly above the microphone array (white plane in photo); the signals of the microphones are processed by the acoustic camera and the data is centralized in the laptop equipped with Labview, which also collects the optical camera signal coming directly from the device installed in the middle of the microphone array. (b) A bottoms-up view of the Underbrink microphone array on the white panels from Figure 3.1a.

For the measurements, 64 microphones were placed in an Underbrink array. This type of pattern is visualized in Figure 3.1b. It has been observed that this type of array outperformed the other analyzed popular beamforming arrays in both resolution and the ability to reject false sources (such as high side lobes) over a large frequency range [30]. During the actual measurements at Den Helder, due to strong winds, sponge windshields were placed on top of each microphone.

In the center of the panels, there is an optical camera assembled such that it can capture the optical images of the overhead vehicle. The camera is directly connected to a laptop equipped with LabView. The microphones are all centralized to the Data Acquisition System (DAQ). This acoustic camera converts analog waveforms into digital signals meant for further processing.

3.1.2. Locations and Weather Conditions

The measurements in Den Helder took place on the 10th of September 2019. The array was placed at 52°57′ 40.93"N latitude and 4°47′36.52"E longitude (see Figure 3.2). The elevation, taken from Google Earth, at these coordinates reads 4.63 m. This is important information since the one of the drone's geolocation at periodic time points is available. Using this information, the time when the drones are above the panel can be determined and an accurate scan grid can be defined. The corresponding atmospheric conditions are presented in Table 3.1 and can potentially be used in a future study on drone noise modeling to determine the impact of the atmospheric sound attenuation on the day of the experiment (according to Appendix D). In the case of the Cyberzoo campaign, the measurement took place indoors in a noisy and uncontrolled environment. As a result, the exact atmospheric conditions were not registered.

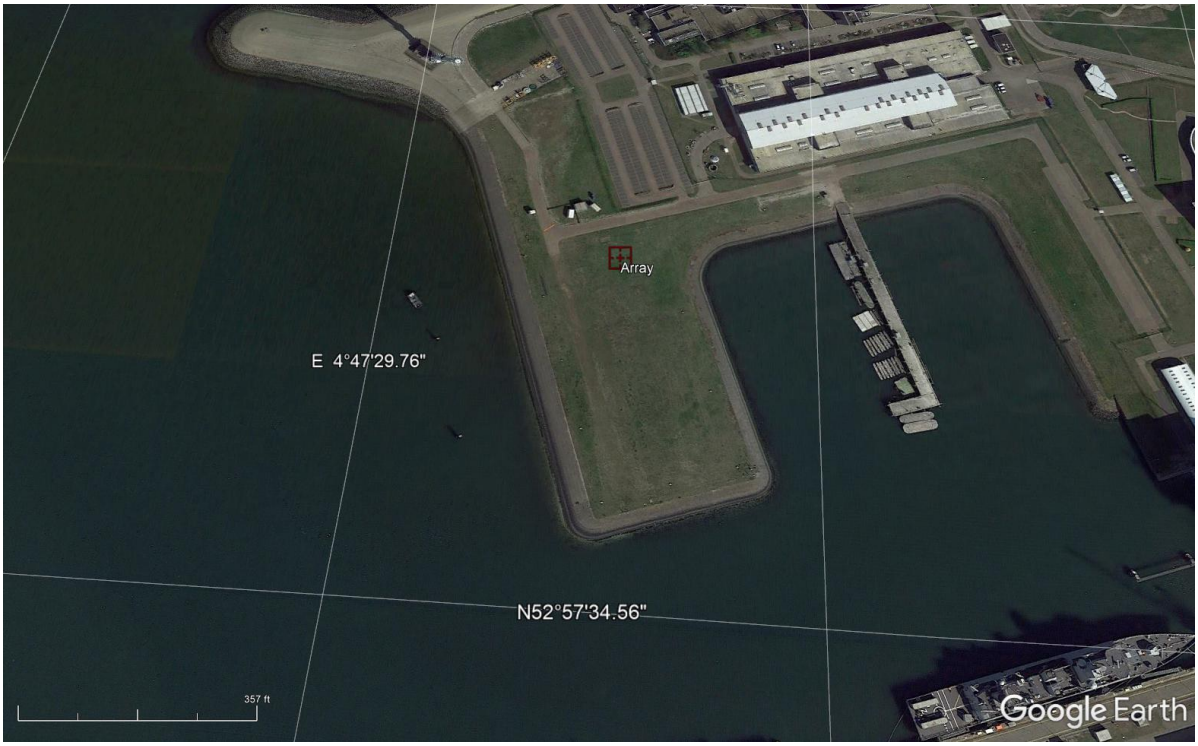

Figure 3.2: Location of the Den Helder Measurements from 10th September 2019. The Array is marked with the red cross-box.

GPS Time	Temperature [°C]	Humidity RH [%]	Wind Direction	Wind Speed [kts]
13:07:09	17.1	74	South-West	5.8
14:39:04	16.7	74	West-South-West	6
15:55:42	17.3	71	South-West	5.4

Table 3.1: Atmospheric Conditions on Day of Den Helder Experiment

3.1.3. Drones Used in the Measurements

Four drones were used throughout the measurements (Table 3.2). The four drones represent four classes of size from micro to large UAV with a wide range of applicabilities.

Drone	Parrot	Phantom	Spyder	Neo
Location	CyberZoo	Den Helder	Den Helder	Den Helder
Type	Quadcopter	Quadcopter	Quadcopter	Octocopter
Size	Micro (μUAV)	Small (SUAV)	Medium (MUAV)	Large (LUAV)
Mass [kg]	0.063	1.38	5.8	7.2
Size [m]	0.18	0.48	0.928	1.1
Rotor Diameter [m]	0.075	0.240	0.365	0.457
Blades per Rotor	2	2	2	2
Purpose	Preparatory Test	Most common	Counter-UAV	Heavy Military

Table 3.2: Specifications of all drones used in the experiments. From now onward, they will be referred to according to their size (e.g. μUAV for the Parrot)

(a) Parrot Mambo Fly [31] (b) DJI Phantom 4 [7] (c) Spyder RH4 [32] (d) AceCore Neo [33]

Figure 3.3: Drones Used in Den Helder Experiment (a) μUAV, (b) SUAV, (c) MUAV, (d) LUAV

3.1.4. Operations and Trajectories

In the case of the quadcopters, the maneuvers specified in Table 3.3 below were used. However, the LUAV (co-axial octocopter) had a prearranged trajectory that could not follow the desired route. Thus, in many of the recordings, the drone cannot be detected on the optical camera. The trajectories of both MUAV and LUAV at Den Helder have been uploaded into Google Earth and assessed. These routes can be seen in Figure 3.4. In the case of the SUAV and the μUAV the exact trajectories are not known as the log files were not available.

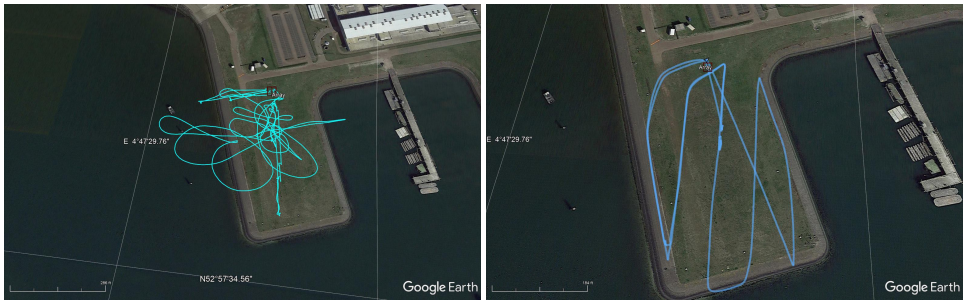

(a) Trajectory of the MUAV during the experiments (b) Trajectory of the LUAV during the experiments

Figure 3.4: Flown Routes of MUAV and LUAV at Den Helder

For the Cyberzoo campaign, the experiment was a first test and thus, took place in uncontrolled conditions. In the end, the viable sample from this measurement is a diagonal fly-over at approximately 0.6 m above the microphone array.

No.	Maneuver	Context
1.	Hover Over Panel	At 3m for 5s
2.	Increase Altitude	From 3m to 10m
3.	Increase Altitude	From 10m to 20m
4.	Increase Altitude	From 20m to 30m
5.	Fly-away	At 30 m
6.	Fly-over	From 30m to 20m
7.	Fly-over	From 20m to 10m
8.	Fly-over	At 10m

No.	Maneuver	Context
1.	Hover Over Panel	At 3m for 5s
2.	Increase Altitude	From 3m to 5m
3.	Increase Altitude	From 5m to 10m
4.	Increase Altitude	From 10m to 4m
5.	Fly-away	At 4 m
6.	Fly-over	At 4 m
7.	Fly-over (Full-Thrust)	At 4 m

Table 3.3: List of Flight Maneuvers for MUAV (left) and SUAV (right)

Correlating drone log files with measured data

The log files have been made available by the operators of the measured drones for the Spyder (MUAV) and Neo (LUAV). Unfortunately, there was a discrepancy for both sets of log files concerning the sequencing of events and time stamps. To mitigate these issues, the files have been correlated with the noise measurements such that the OSPL values correspond to the norm of the distance vector, as it is expected that distance is inverse propotional to the noise levels. To do this, first, the OSPL in the time domain for all MUAV measurements have been computed. Three log files containing the UAV positions were present, starting and ending at time instants which include the starting and ending timestamps of the measurement session. Since the sampling frequency in the log files was equal to 2 Hz, the chunk lengths in calculating the OSPL have also been selected as 0.5 seconds. This is done such that the number of computed SPL values corresponds to the number of log samples. The empty space between measurements has been replaced by NaN values. The same procedure was done for the empty space between log files inside a set. The below diagram (Figure 3.5) shows the relation between times of the log files and the times of the measured acoustic data.

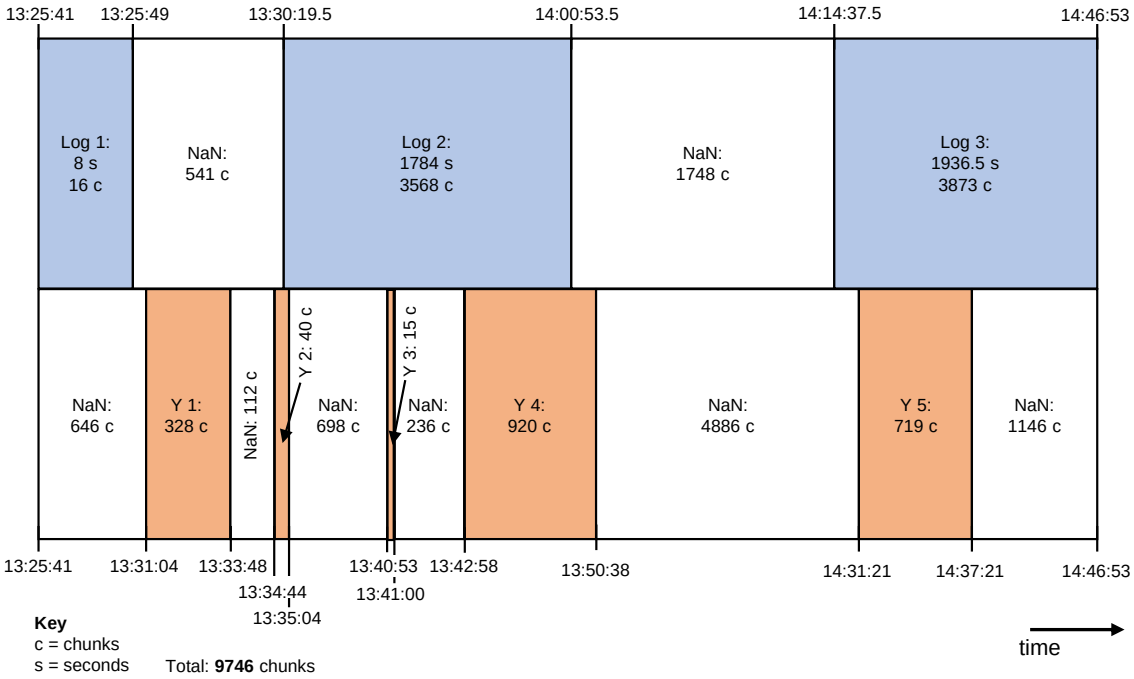

Figure 3.5: Initial synchronization of position log files from the MUAV (blue) and the measured acoustic data (orange)

After the correlation calculations, it seems that the corrected files should be positioned 349 chunks (174.5 seconds) after their original timestamps (see Figure 3.6). In order to verify this, the OSPL was compared with the height and the angle of observation for the drone, besides the distance (Figure 3.7). The outcome presents a coherent match, as the fluctuation in the levels can be correspondent to the position of the drone at all times. With this mismatch out of the way, the data is ready for processing.

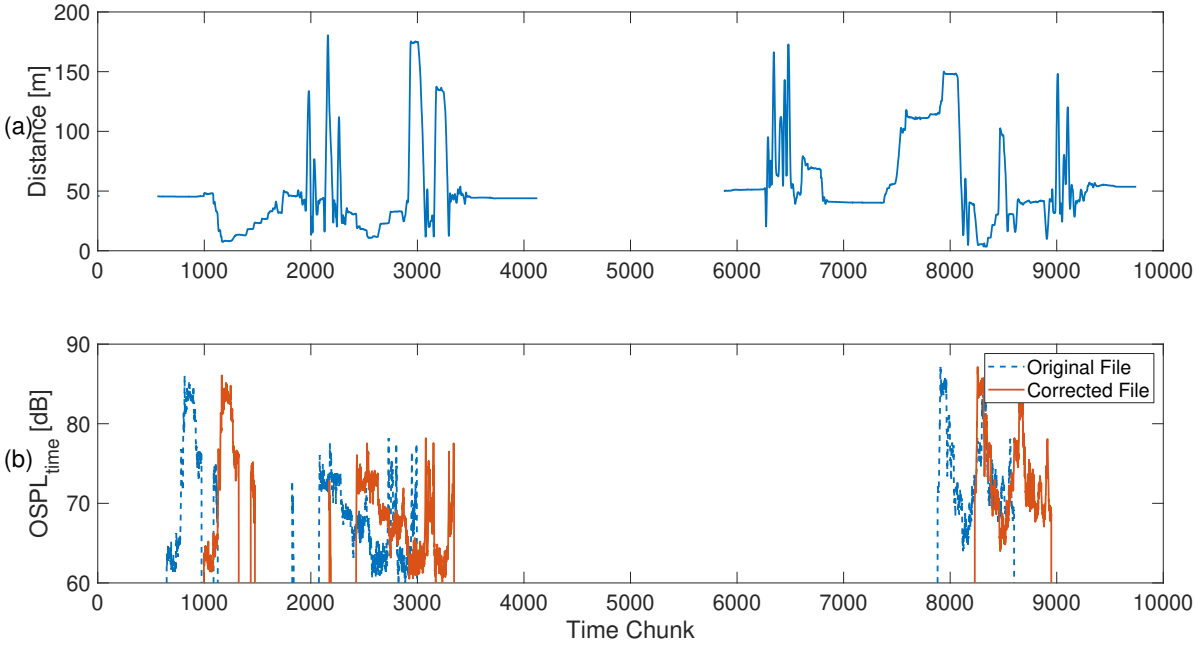

Figure 3.6: Correlating the distance values from the MUAV log file (a) to the OSPL values in time domain (b) computed from the acoustic data. The original acoustic file is sequenced in blue and the corrected acoustic data with a lag of 174.5 seconds (= 349 chunks) in orange

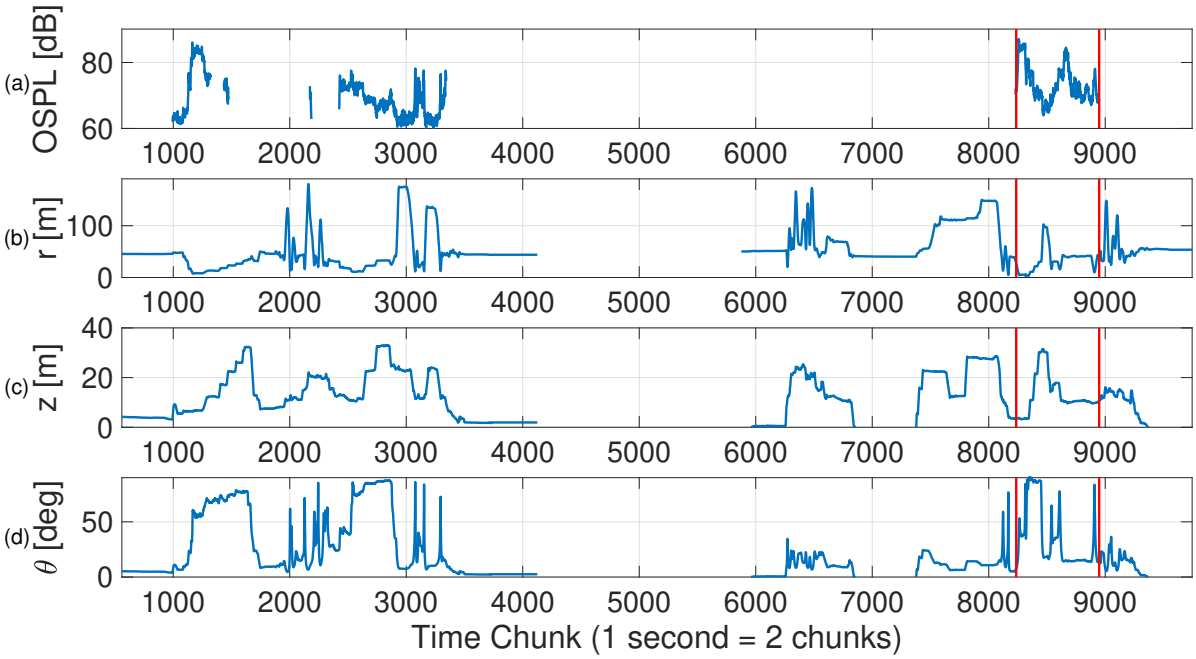

Figure 3.7: Correlation of log files (with computed r distance (b), z height (c) and θ angle of observation (d)) with corresponding OSPL from the measurements (a). The selected experiment of interest is framed by the red limits.

3.2. Spectral Analysis

As microphones tend to wear out over time, the first important step is filtering out the faulty microphones, such that corrupted data can be ignored. Finding the faulty microphones can be done easily by plotting the signal received by each microphone. Figure 3.8 represents the OSPL in frequency domain (sampled from a short time snapshot of 0.5 seconds) over each microphone for the frequency range up until the Nyquist frequency (or folding frequency) of 25,000 Hz (since the sampling frequency of the signal is 50,000 Hz). Frequencies beyond this limit are aliased (replicated at other positions in the whole spectrum) and treated as lower frequencies. This effect can be mitigated by using an 'anti-aliasing' filter (or a 'low-pass' filter) that blocks

everything above the Nyquist frequency [34]. Six microphones were non-functional, respectively numbers 21, 32, 40, 46, 62 and 63 (location visible in Figure 3.1b).

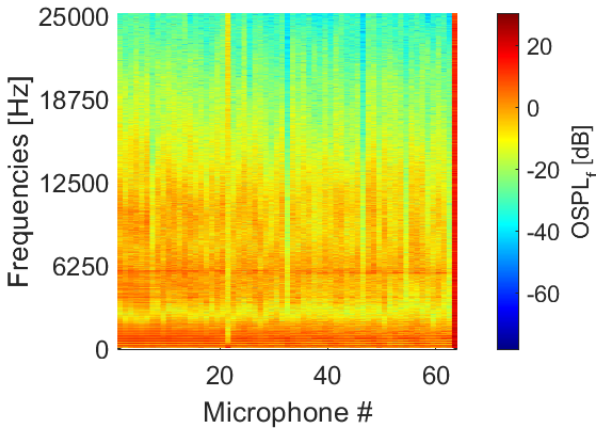

Figure 3.8: Frequency domain OSPL per Microphone and Frequency shows the faulty microphones 21, 32, 40, 46, 62 and 63.

Using the functional microphones, the resulting spectrum of the recorded noise is analyzed. Peaks in the energy spectrum denote relevant frequencies which can be further characterized. The analysis was done based on spectral information. This represents the frequency spectrum as a function of time. Besides, analyzing a spectrogram uncovers a multitude of other characteristics present in the data (i.e. ground reflection, Doppler effect, etc.).

When calculating the spectrogram of a signal, certain inputs must be specified, such as windowing, overlapping and number of samples. The windowing defines the length of the segments into which the signal is divided. The overlap specifies the percentage of the overlapping segments. Lastly, the number of discrete Fourier transform points (NFFT) is also specified. For this research, the results containing the spectrograms of the measured data were produced using the settings of Table 3.4.

Windowing	Overlap	NFFT
Hamming	85%	4096

Table 3.4: Spectrogram Settings

Windowing and weighting methods are often used to enhance the quality of the received signal. These signal analysis techniques are used to reduce the effect of side lobes in a signal, at the expense of broadening the main lobe as can be seen in Figure 3.9, by smoothing out the signal. With the side lobes reduced, the true source is more readily detectable when applying the imaging techniques.

Another way of assessing the spectra is done by plotting the Power Spectral Density (PSD) over the frequencies as described in section 2.2. This takes away the sense of the temporal behavior, but it will still show a clear overview of the behaviorism in the frequency domain.

MATLAB's *'pwelch'* function has been applied to visualize a smoothed plot of the signal by windowing using Welch's method [35]. Windowing returns the PSD estimate of the input signal found using Welch's overlapped segment averaging estimator. The signal is divided into the longest possible segments to obtain as close to 8 segments as possible (but not exceeding this number) with a 50% overlap. Each segment is windowed with a Hamming window. The estimate of the spectral density is averaged to obtain the PSD estimate.

3.3. Beamforming Techniques

Knowing the frequencies of interest, the focus can now be shifted to beamforming techniques. As mentioned in the previous chapter, the purpose of imaging is to observe the specific sources of noise on the drone and their corresponding strength.

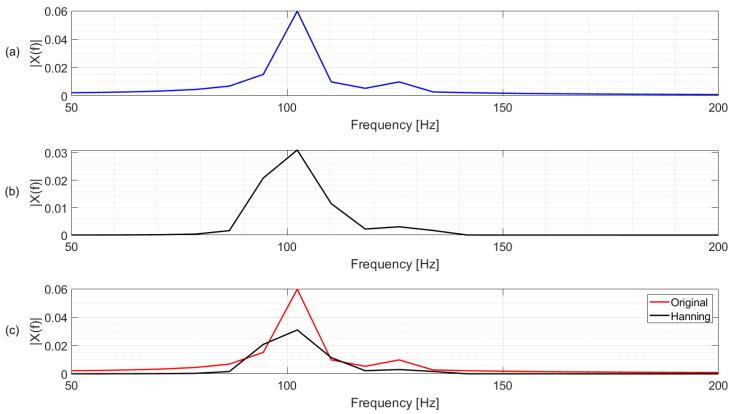

Figure 3.9: Effects of Hamming Windowing on a Signal with Side lobes

3.3.1. Conventional Beamforming (CB)

Conventional Beamforming is one of the basic beamforming techniques known and used in aviation-related issues to visualize the noise sources of a vehicle. The sources considered by CB are assumed to be monopoles. The derivations in this chapter are strongly oriented on [34] and [36]. The pressure field of a monopole source perceived at a specific microphone m, in time domain, can be expressed as:

$$p_m(t) = \frac{r_0}{||\mathbf{r_m}||} p_0\left(t - \Delta t_m\right), \tag{3.1}$$

with p_m the perceived pressure at microphone m, p_0 is the acoustic pressure at a reference distance of $r_0 = 1\ m$, the time point t, Δt_m the time delay specific to the microphone, and r_m is the distance vector from the source to the receiver. As explained in section 2.4, the delay can be easily computed by dividing r_m by the speed of sound c such that $\Delta t_m = \frac{\|\mathbf{r_m}\|}{c}$.

When considering a moving source, this delay must be corrected as:

$$\Delta t_m = \frac{-\mathbf{r_m}\cdot\mathbf{M} + \sqrt{(\mathbf{r_m}\cdot\mathbf{M})^2 + \|\mathbf{r_m}\|^2\beta^2}}{c\beta^2} \tag{3.2}$$

with $\mathbf{M}$ the Mach speed vector of the source, and $\beta = \sqrt{1 - \|\mathbf{M}\|^2}$. The derivation of this expression can be found in Appendix A.

When considering a signal at frequency f, Equation 3.1 becomes [34]:

$$P_m(f) = \frac{r_0}{\|\mathbf{r_m}\|} P_0(f) e^{-2\pi i f \Delta t_m} = P_0(f) g_m(f) \tag{3.3}$$

with P_0 and P_m the Fourier transforms of the pressures in Equation 3.1. Rewriting this equation (see right side of Equation 3.3), the steering vector component g_m per microphone can be defined. The steering vector $\mathbf{g}$ contains the phase shifts corresponding between all microphones and the source.

As $P_0(f)$ is unknown, the aim of beamforming is to find this source strength along with its location (contained in $\mathbf{g}$). This is done via a cost function commonly denoted with J, evaluated at each grid position as $J = \|\mathbf{P} - P_0(f)\mathbf{g}\|^2$, where $\mathbf{P}$ is the pressure vector containing all P_m components. Using the least square method, this function is minimized. The minimization yields the amplitude estimate:

$$\hat{P}_0(f) = \frac{\mathbf{g}^*\mathbf{P}}{\|\mathbf{g}\|^2} \tag{3.4}$$

where $*$ designates the complex conjugate transpose, in this case of the steering vector $\mathbf{g}$. Now B, the beamforming output is calculated as:

$$B = p_{eff}^2 = \frac{1}{2}\left|\hat{P}_0(f)\right|^2 = \frac{1}{2}\hat{P}_0(f)\hat{P}_0^*(f) \tag{3.5}$$

By substituting Equation 3.4 into Equation 3.5, the defining equation of CB is determined as:

$$B(f) = \frac{1}{2}\frac{\mathbf{g}^*\mathbf{P}}{\|\mathbf{g}\|^2}\left(\frac{\mathbf{g}^*\mathbf{P}}{\|\mathbf{g}\|^2}\right)^* = \frac{1}{2}\frac{\mathbf{g}^*\mathbf{P}\mathbf{P}^*\mathbf{g}}{\|\mathbf{g}\|^4} = \mathbf{w}^*\mathbf{C}\mathbf{w} \tag{3.6}$$

where $\mathbf{w}$ is the weight vector equal to $\frac{\mathbf{g}}{\|\mathbf{g}\|^2}$, and $\mathbf{C}$ is the Cross-Spectral Matrix (CSM) (or covariance matrix) equal to $\frac{1}{2}\mathbf{P}\mathbf{P}^*$.

As the source location is unknown, Equation 3.6 is applied to a wide range of possible locations. This range constitutes the so-called "Scan plane", large enough to approximately contain the possible location of the sources. A grid is defined over this Scan plane and B is computed at each grid point j with coordinate $\boldsymbol{\xi_j}$. Thus for each microphone positioned at vector $\mathbf{x_{m,O}}$ from the center of the array, the distance vector to each scan grid point becomes $\mathbf{r_m} = \mathbf{x_{m,O}} - \boldsymbol{\xi}_j$. As a consequence, the steering vector elements expand into $g_m(\boldsymbol{\xi}_j, f)$ leading to the expansion of B from Equation 3.6 into $B(\boldsymbol{\xi}_j, f)$, giving the source plot of the sound source at frequency f. Unfortunately, CB suffers from low spatial resolution at low frequencies and high spatial aliasing at high frequencies. These effects can be mitigated by applying incoherent averaging of the beamform results over the frequencies (see Equation 3.7), thus preserving a good resolution and eliminating side-lobes occurring at a single frequency.

$$B_{incoh}\left(\boldsymbol{\xi}_j\right) = \frac{1}{N_f}\sum_{h=1}^{N_f} B\left(\boldsymbol{\xi}_j, f_h\right) \tag{3.7}$$

where N_f is the number of elements in the frequency range.

The CB results are converted to SPL levels via:

$$\mathrm{SPL}_{CB}(f) = 10\log_{10}\left(\frac{B\left(\xi_j, f\right)}{p_{ref}^2}\right) \tag{3.8}$$

3.3.2. Functional Beamforming (FB)

Functional Beamforming is an adaptation building up upon the CB in order to increase the spatial resolution and obtain a more clean source map. The derivations in this chapter are strongly oriented on [23]. The main approach behind this method consists of a deconvolution of the CSM into its eigenvalues and eigenvectors, as defined in the equation of the Equation 3.9.

$$\mathbf{C} = \mathbf{U}\Sigma\mathbf{U}^* \tag{3.9}$$

where $\mathbf{U}$ is the unitary matrix of $\mathbf{C}$'s eigenvectors and Σ is the diagonal matrix of $\mathbf{C}$'s eigenvalues, σ. After dismantling the cross spectral matrix as such, an exponential parameter ν can be applied:

$$\boldsymbol{C}^{\frac{1}{\nu}} = \boldsymbol{U}\,\mathrm{diag}\left(\sigma_1^{\frac{1}{\gamma}}, \ldots, \sigma_N^{\frac{1}{\nu}}\right)\boldsymbol{U}^* \tag{3.10}$$

The above, yields the following equation for Functional Beamforming (FB):

$$\mathbf{B}_\nu(\boldsymbol{\xi}_j) = \left[\mathbf{w_j}^*\mathbf{C}^{\frac{1}{\nu}}\mathbf{w_j}\right]^\nu = \left[\mathbf{w_j}^*\mathbf{U}\Sigma^{\frac{1}{\nu}}\mathbf{U}^*\mathbf{w_j}\right]^\nu \tag{3.11}$$

where $\mathbf{w}$ is the weight vector defined as:

$$\mathbf{w}_j = \frac{\mathbf{g}_j}{\left\|\mathbf{g}_j\right\|^2} \tag{3.12}$$

Expanding Equation 3.11 to give a more detailed comprehension:

$$B_\nu\left(\boldsymbol{\xi_j}\right) = \left(\frac{g_j^* C^{\frac{1}{\nu}} g_j}{\left\|g_j\right\|^4}\right)^\nu = \left(\frac{g_j^* U\Sigma^{\frac{1}{\nu}} U^* g_j}{\left\|g_j\right\|^4}\right)^\nu \tag{3.13}$$

Considering a specific source location of strength s_l and knowing that $\mathbf{C} = \frac{1}{2}\mathbf{P}\mathbf{P}^*$ and $\mathbf{P} = s_l\mathbf{g_l}$, the above equation can be expressed as:

$$B_v(\boldsymbol{\xi_j}) = \left(\frac{g_j^* g_l \left(\frac{1}{2} s_l^2\right)^{\frac{1}{v}} g_l^* g_j}{\|g_j\|^4} \right)^v = \frac{1}{2} s_l^2 \left(\frac{\left\|g_j^* g_l\right\|^2}{\|g_j\|^4} \right)^v \tag{3.14}$$

The relation $\left(\frac{\left\|g_j^* g_l\right\|^2}{\|g_j\|^4} \right)$ is also known as the Point Spread Function (PSF). This PSF has the value 1 in the correct location and smaller than 1 values in the other locations. Thus when powering up to this exponential parameter, the correct location keeps its value 1, while the others are greatly reduced. This produces a "clean-up" of the scan plane, with the true strength and location of the source clearly distinguishable from the fake sources.

Thus, since the value of the function is 1 at the correct source position and lower than one in all other positions, powering it by the exponent v will lower the power at the side-lobe and sharpen the beamformer peaks at the correct noise location. ([23])

3.3.3. Dipole Beamforming (DB)

As mentioned before, in this thesis, the assumption of the multipole source types on a rotor take the form as presented in Figure 2.5. In an overview over a drone, this can be illustrated as in Figure 3.10.

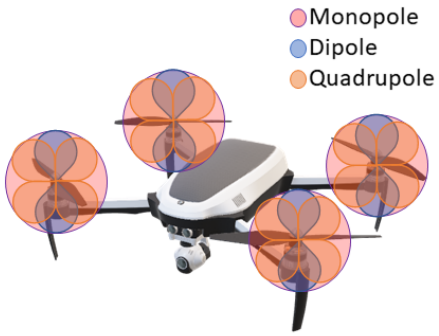

Figure 3.10: Multipole Noise Sources Distributed on a Drone (idealized illustration)

Since Conventional and Functional Beamforming only consider monopole sources, this new issue could be mitigated through Dipole Beamforming. The methodology explained in this subsection is primarily based on the work presented in [37]. The main idea around Dipole Beamforming revolves around correcting with the ratio of the dipole versus the monopole pressure fields. This ratio is defined as the Dipole Characteristic Term which in literature is commonly denoted as DPL and equal to:

$$\mathrm{DPL_m}(f) = -i\omega \mathbf{d} \cdot \nabla(\Delta t_m) \tag{3.15}$$

where $\mathbf{d}$ is the distance vector between the poles containing the distances on x-, y- and z-axis, which should satisfy the relation $kd << 1$ as discussed in subsection 2.3.2. $\nabla(\Delta t_m)$ is the gradient of delay vector and $\omega = 2\pi f$. Appendix A provides a detailed derivation of this equation.

The beamforming correction mainly revolves around modifying the steering vector elements g_m (see right side of Equation 3.3). Thus it is actually reduced to multiplying the monopole steering vector with the ratio between the DPL and the norm of $\mathbf{d}$, distance vector between the dipoles. This is supposed to directly identify the true dipole with its strength rather than just correct the monopole location. Hence, the correction adapts the steering vector equation as follows:

$$g_{di,m}(f) = \frac{e^{-2\pi i f \Delta t_m} \mathrm{DPL_m}(f)}{\|\mathbf{r_m}\| \|\mathbf{d}\|} = g_{mono,m}(f) \frac{DPL_m(f)}{\|\mathbf{d}\|} \tag{3.16}$$

These beamforming corrections can be then implemented in Equation (3.6) and Equation (3.11) to generate both Conventional and Functional Beamforming plots.

It should be noted that the algorithm in [37] requires knowledge of the dipole orientation on the scan grid. Thus the approximate positioning is an input to DB. Within the thesis, this shall be taken into account (considering dipole noise generation on the rotor disk - Figure 2.5). However, this issue may give rise to some errors as the exact positioning of the dipoles/quadrupoles of a rotor is not always initially known.

3.3.4. Scan grid detector

In order to determine the physical size of the scan grid in the focal plane of the drone as recorded by the optical camera, a scan grid detector has been developed. This detector takes 31 frames of the optical images around the selected time point of analysis. The video is cut to the frame of interest. The median of the frames, in time, is subtracted thereby removing the relatively static background image (slowly moving clouds, etc.). The pixel values of the whole video are normalized to 1 and the difference between subsequent frames is taken.

Since the background is moving much slower than the drone, this subtracts most of the background, while the drone will remain visible. Afterward, the drone can be (roughly) segmented by simple thresholding. This method requires replacing each pixel in the image with a black pixel if the image intensity is less than some fixed constant (selected 0.5 in this case), or a white pixel if the image intensity is greater than that constant. The segmentation across the whole video is summed and the masks (the segmentation at each frame) are connected to yield the path (trajectory) of the drone. The video is then looped frame by frame and the drone is fitted to an anisotropic Gaussian (i.e. directional Gaussian where the standard deviations along x-axis and y-axis can differ). The drone diameter is estimated as the Full-Width at Half Maximum (FWHM) of the Gaussian. The fit of the Gaussian to the drone gives the standard deviations in both 2D directions. Afterward, the FWHM from these values is computed. Finally, the pixel size is computed as $\frac{Diam}{FWHM}$, where $Diam$ is the real diameter of the drone in meters (FWHM is given in pixels). Because the drone is not always in focus or the image appears blurry, the pixel size is determined for 15 images before and after the image of interest and the average (± standard deviation) pixel size over the video segment is computed.

3.3.5. Validation with Synthetic Data

As the beamforming algorithms have been described in depth, it is possible to apply them to real-life data. However they must first be verified for correct implementation. In addition, since their performance on a clean scan grid must be assessed for all the types of noises, synthetic data has been generated, consisting of monopoles, dipoles or quadrupoles on predefined locations.

Synthetic data was generated first for one noise source (either a mono-, di- or quadrupole) and afterward for 4 noise sources mimicking a quadcopter. Using this data, the performance of functional and conventional beamforming was tested. Afterward, both the DB and QB implementations were tested in a "conventional" context and accompanied by the functional beamforming adaptations.

Zero amplitude is set on the whole scan grid, except for the positions and strengths where monopoles were set as input. These powers (s_l) will be used to construct the synthetic Cross Spectral Matrix knowing:

$$\mathbf{C} = \frac{1}{2}\mathbf{P}\mathbf{P}^* \tag{3.17}$$

where $\mathbf{C}$ is the Cross-Spectral Matrix (CSM) and $\mathbf{P}$ contains the Fourier transforms of the pressure. Considering the source at point $j = l$ of the scan grid, with strength s_l, the received signal takes the form $\mathbf{P} = s_l\mathbf{g_l}$ and thus $\mathbf{C}$ becomes:

$$\mathbf{C_l} = \frac{1}{2}s_l\mathbf{g_l}\mathbf{g_l}^* s_l = \frac{1}{2}s_l^2\mathbf{g_l}\mathbf{g_l}^* \tag{3.18}$$

This is valid for the case of only one noise source. However, when multiple sources are created, the CSM for each source is calculated using Equation 3.18, and afterwards, they are summed into the total CSM:

$$\mathbf{C_{total}} = \sum_{l=1}^{N_s}\mathbf{C_l} \tag{3.19}$$

Substituting this into Equation 3.6 and steering at grid point $\boldsymbol{\xi_j}$ yields:

$$B(\boldsymbol{\xi}_l) = \frac{1}{2}s_l^2 \tag{3.20}$$

For dipoles and quadrupoles, the same technique is applied, however with a small modification to the inputted amplitudes in the cross matrix, using Equation 2.22 and Equation 2.27. Thus the monopole signal $s_l\mathbf{g_l}$ is multiplied with $k\|\mathbf{d}\|\cos(\theta)$ for the dipole and with $k^2\|\mathbf{d}\|\|\mathbf{D}\|\cos(\phi)$, for the quadrupole, where ϕ is the angle between the vector $\|\mathbf{r_m}\|$ and the quadrupole axis.

Determining Expected Source Strengths

To determine the initial strength which needs to be input such that the final beamforming plot shows a certain strength in dB, an inverse way of determining the equation is performed. Substituting Equation 3.20 into the following,

$$SPL = 10log10(\frac{B}{p_{ref}^2}) \tag{3.21}$$

the relation shown below is generated:

$$s_l = \sqrt{2p_{ref}^2 10^{\frac{SPL}{10}}} \tag{3.22}$$

When looking at the theory from the subsection 2.3.2 it can be determined that in the case of a dipole, the strength shall be multiplied by as following:

$$s_{di} = s_{mono}k\|\mathbf{d}\| \tag{3.23}$$

Similarly, for a quadrupole (as assessed from subsection 2.3.3), the strength shall be determined as:

$$s_{quad} = s_{mono}k^2\|\mathbf{d}\|\|\mathbf{D}\| \tag{3.24}$$

When using the same value of the reference monopole to construct a dipole and a quadrupole, the expected real output strength (in dB) for both the dipole and the quadrupole follow the trends from Figure 3.11. Thus building a dipole using two monopoles of strength 83 dB (as done in [37]) as its poles yields a dipole of strength 60 dB. When building a quadrupole, the output will be approximately 49 dB.

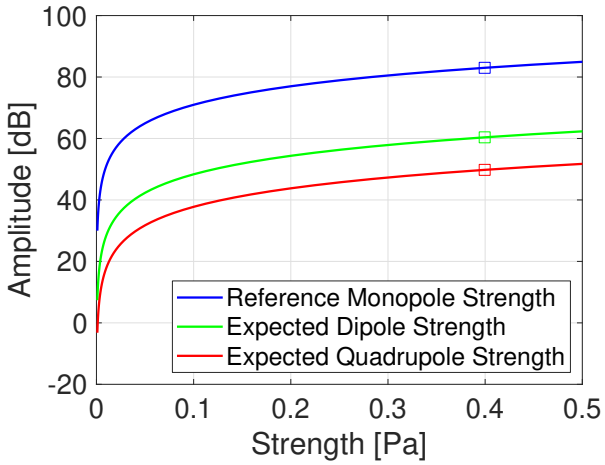

Figure 3.11: Beamforming output for a source monopole, dipole and quadrupole in dB versus the input pressure strength of the monopole [Pa]. The square markers are corresponding to the sources built with 83 dB monopoles (as selected in [37])

3.4. Concluding Remarks

In conclusion, this chapter served as an explanation of the used methods and materials for the research. These methods are later validated with simulated data and the results are exposed, explained and assessed (see section 4.5). This will lead to a set of conclusions regarding the necessary approaches to identify source locations and source strengths. Beamforming methods have been introduced which are be further developed and validated in section 4.3.

4

Results and Discussion

This chapter presents the main outcomes of analyzing the measurements described in subsection 3.1.4. First, the beamforming results are presented, starting with the synthetic data and followed by the application on real-life data. Afterward, each drone operational maneuver is analyzed and the noise sources on the drones are identified. Following, the noise behavior with respect to the change in design parameters is presented. The potential modeling variable are also described and explained. Lastly, the chapter ends with results from comparing different noise metrics (as presented in the section 2.2) and concluding which would be the appropriate quantity for drones.

4.1. Development of a Quadrupole Beamforming algorithm

Quadrupole noise sources are typical for rotor noise, and thus also for drone noise. Based on the fact that a quadrupole consists of two dipoles pulsating out of phase (subsection 2.3.2), a new beamforming algorithm can be constructed analogously to the Dipole Beamforming (and its derivation from Appendix A). This can be done by assuming the monopoles in the derivations as the dipoles of the quadrupole. This will be referred to as Quadrupole Beamforming (QB).

Similarly as in the DB algorithm, the ratio between the dipole and the quadrupole pressure field is calculated and applied to the original steering vector. This aims to correct the monopole location and strength such that it shows the real values.

This pressure field ratio will be called the Quadrupole Characteristic Term (denoted as QPL) and will be determined as:

$$\mathrm{QPL_m}(f) = -i\omega \mathbf{D} \cdot \nabla(\Delta t_m) \tag{4.1}$$

where $\mathbf{D}$ is the distance vector between the dipole poles of the source, containing the distances on x-, y- and z-axis, which should satisfy the relation $kD \ll 1$ as discussed in subsection 2.3.3. $\nabla(\Delta t_m)$ is the gradient of delay vector and $\omega = 2\pi f$.

Next, the steering vector is corrected in a similar fashion as before:

$$g_{quadru,m}(f) = \frac{e^{-2\pi i f \Delta t_m}\mathrm{QPL_m}(f)}{\|\mathbf{r_m}\|\|\mathbf{D}\|} = g_{di,m}(f)\frac{QPL_m(f)}{\|\mathbf{D}\|} = g_{mono,m}(f)\frac{DPL_m(f)QPL_m(f)}{\|\mathbf{d}\|\|\mathbf{D}\|} \tag{4.2}$$

This steering vector is afterward replaced in Equation 3.6 and Equation 3.11 and beamforming proceeds as usual.

4.2. Analysis of Synthetic Data

In order to verify the implementation and performance of the monopole conventional and functional beamforming, as well as the newly implemented dipole and quadrupole beamforming, synthetic data is generated. First, the algorithms will be tested for one source and varying poles. Afterward, a synthetic drone will be simulated using approximate parameters as in the real-life measurements. Using the method from subsection 3.3.5 to determine the beamforming output, it is expected that for a reference monopole of 83 dB, the output of a dipole will be approximately 60.37 dB output and for a quadrupole, approximately 49.79 dB. These

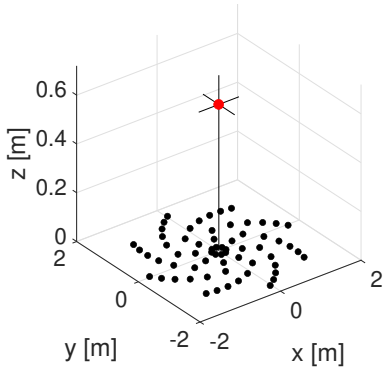

Figure 4.1: Overview on Synthetic Source Position (red - source; black - microphone array)

Element	Value
Source Location (XYZ) [m]	[0,0.005,0.6]
Frequency [Hz]	2000
Mach Flow Speed (XYZ)	[0.1, 0, 0]
Dipole Distance [m]	[0,0.002, 0]
Monopole strength (s_l) [dB]	83

Table 4.1: Simulation Parameters of Synthetic Data used in [37]

values are expected for the case of one source noise. In the case of a simulated UAV, the reference monopole will be selected with a value of 60 dB. This would theoretically result in a 37.37dB SPL for a dipole and 26.79 dB SPL for the quadrupole. The accuracy of the beamforming is expected to decrease as it is expected that interference between the four sources will influence the outputs.

4.2.1. One Noise Source

Simulation parameters were chosen as in [37] (see Figure 4.1) in order to mimic the published results (according to Table 4.1). The simulated 3D environment is shown in Figure 4.1.

First, a monopole is simulated and visualized through both conventional and functional beamforming.

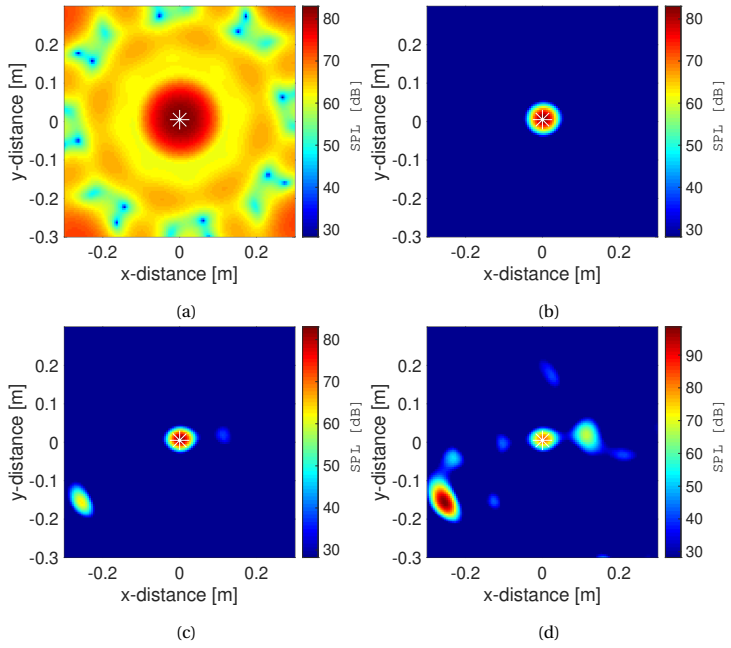

Figure 4.2: Performance of Functional Beamforming for varying ν parameter: (a) $\nu = 1$ which is corresponding to the Conventional Beamforming; (b) $\nu = 20$; (c) $\nu = 40$; (d) $\nu = 50$.

The location is modified in order to observe the performance of the algorithms for different source locations and the limits of the functional beamforming method are tested by changing ν, the functional beamforming exponential parameter (Figure 4.2).

CB (corresponding to FB with $\nu = 1$) and FB up until $\nu = 46$ detect both the correct strength and correct location. For higher values of ν, the source location is still correct, however, apparition of spontaneous sidelobes overpowers the source and thus the strength and location of the true source are lost. For this reason, the rest of the research will make use of $\nu < 40$ as the exponential parameter values for FB.

When testing the location in Figure 4.3 it can be observed that the CB easily detects the correct source location with the given source strength. This validates the correct implementation of the CB algorithm. An equally good performance can be observed for the functional beamforming method.

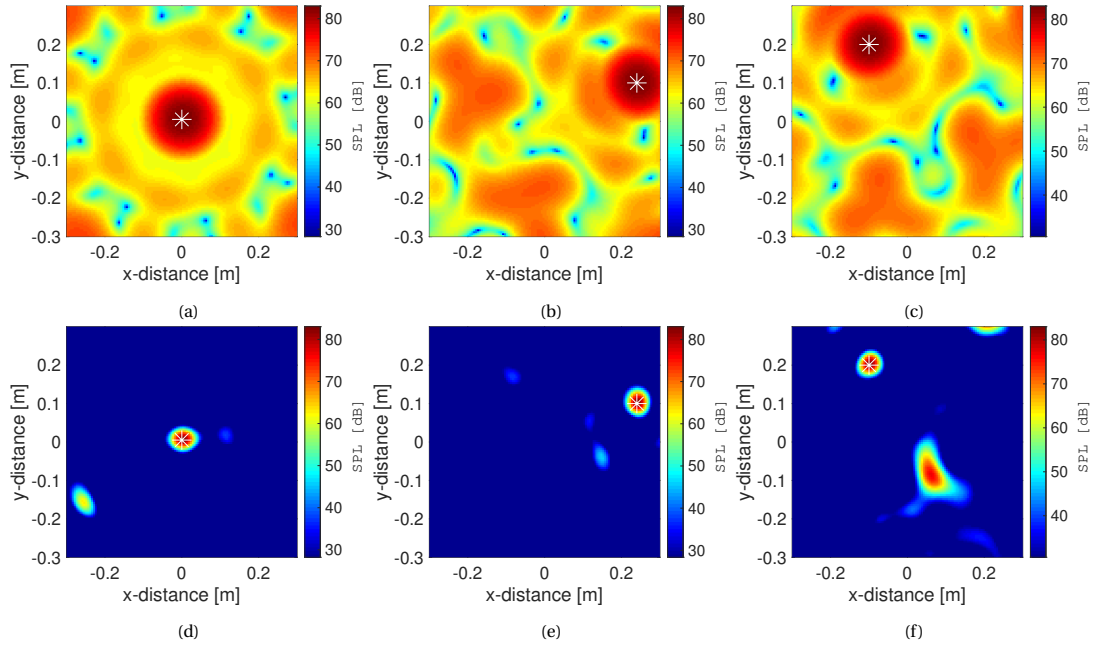

Figure 4.3: Beamforming plots of Conventional and Functional Beamforming ($\nu = 40$) for three different source positions: (a) CB at [0, 0.05] (b) CB at [0.24, 0.1] (c) CB at [-0.1, 0.2] (d) FB at [0, 0.05] (e) FB at [0.24, 0.1] (f) FB at [-0.1, 0.2]

Next, CB and FB are applied to a dipole synthetic noise source (Figure 4.4). As aforementioned, CB is developed such that it takes into account only monopole noise sources. As a consequence, it is expected to have a decrease in performance when encountering a multipole.

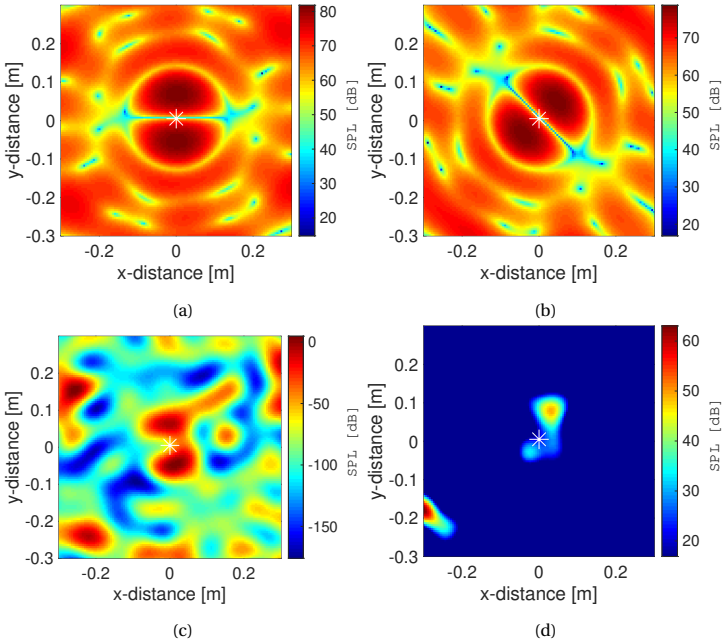

Figure 4.4: Performance of Conventional and Functional Beamforming ($\nu = 40$) on a Dipole Noise Source: (a) Dipole visualized with CB (b) Dipole visualized with CB - slight inclination (c) Dipole visualized with FB (d) Dipole visualized with FB - slight inclination

The two poles of the dipole along with their orientation are discovered (Figure 4.4a). Changing the orientation also accurately changes the beamforming plot (Figure 4.4b). For the FB, a sudden decrease in performance can be observed and this might be due to its sensitivity to mismatches in the steering vector (Figure 4.4c and Figure 4.4d).

When using the DB method, the location of the dipole is correctly found (Figure 4.5a). The dipole is now resolved and the powers are consistent with the ones in the reference publication [37]. Also, the same behavior as in the publication, i.e. the appearance of side lobes, can be noticed. Those can be, however, suppressed by adapting FB with DB. The decent performance of the functional beamforming appears to have been restored as the strength and location are accurately detected and the side-lobes have disappeared (see Figure 4.5b).

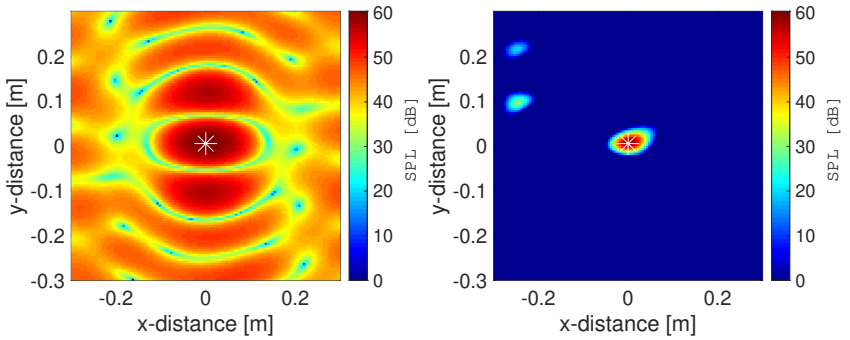

(a) (b)

Figure 4.5: Performance of Dipole Beamforming (a) and Dipole Functional Beamforming (b) ($\nu = 40$) on a Dipole Noise Source

Next, DB is tested in relation to the angle of observation (Figure 4.6). In comparison to the initial situation (compare Figure 2.12) the strength levels computed by DB are approximately the same as in the overhead position (at $\theta = 90°$), with insignificant variation. This is in contrast to the situation from Figure 2.12 where the strength was not constant with varying angle of observation. Beside that, the output was only showing the strength of the reference monopoles and not the real output. This has now been corrected with DB, and thus the correct strength of the dipole can be identified regardless of the observation point. This proves the applicability of DB algorithm as a reliable tool to assess the real strength of a noise source, when dealing with a dipole. In the case of 30°, the similar pattern of side-lobes appears as in Figure 2.12. This can be attributed to the resolution limitations of the microphone array geometry considered in this plots. The geometry is the same as the pattern used in the measurements.

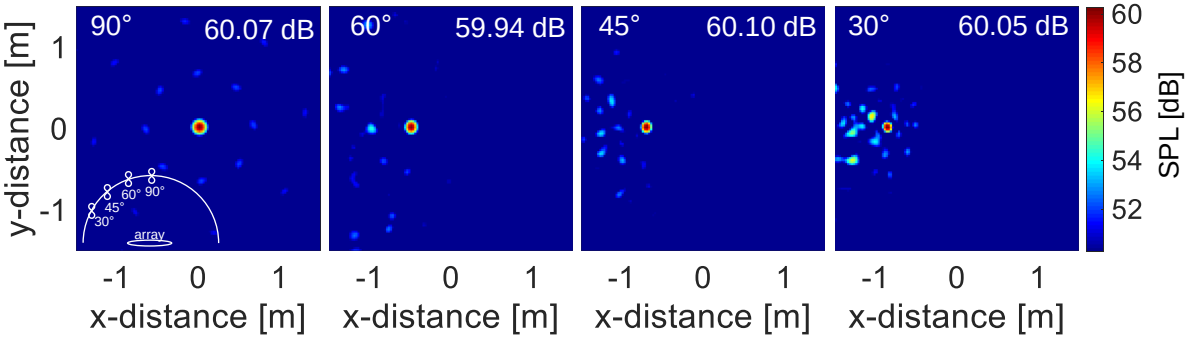

Figure 4.6: Performance of Dipole Beamforming on a dipole when varying the angle of observation. As opposed to the situation in Figure 2.12, where CB was resulting in different values of the dipole source with this angle change, DB mitigates this issue and the correct value of the source is identified.

Finally, the performance of CB on a quadrupole source is assessed. As in the case of the dipole, the four monopoles of the quadrupole are distinguishable and their orientation can be switched and still be observed in the beamforming plot with a strength close to the reference monopoles (Figure 4.7a,b). Analogous to DB, the performance of the functional beamforming decreases, with extremely inaccurate amplitudes, a lot of side-lobes and a loss of location (Figure 4.7c and Figure 4.7d).

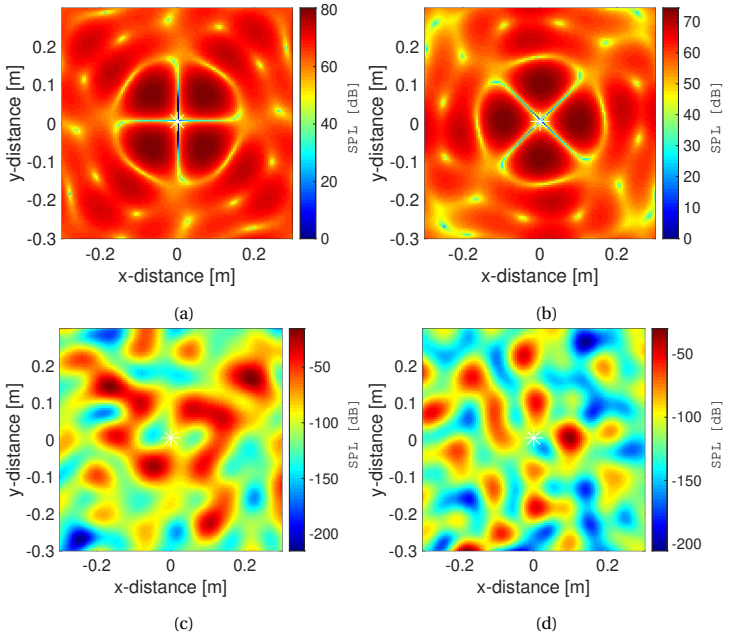

Figure 4.7: Performance of Conventional and Functional Beamforming ($\nu = 40$) on a Quadrupole Noise Source (a) Quadrupole visualized with CB (b) Quadrupole visualized with CB - slight inclination (c) Quadrupole visualized with FB (d) Quadrupole visualized with FB - slight inclination

Next, the performance of the DB is tested on this quadrupole noise source (Figure 4.8). The two dipoles are distinguished and the output beamforming strength is reasonable, as they are given as two dipoles of 60.28 dB each, consistent with the outcome from Figure 4.5a.

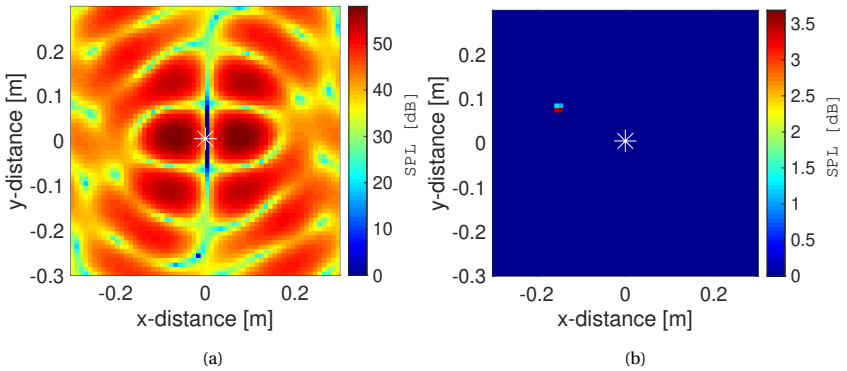

Figure 4.8: Performance of Dipole Beamforming (a) and Dipole Functional Beamforming (b) ($\nu = 40$) on a Quadrupole Noise Source

With the QB method, the quadrupole is resolved (Figure 4.9a), and the powers seem correct as they match the estimated expected strength from Figure 3.11. Again, side-lobes appear around the real location, however they do not overpower it. This can be mitigated with the Quadrupole Functional Beamforming: FB regains its accuracy when coupled within QFB as the side-lobes are eliminated (see Figure 4.9b).

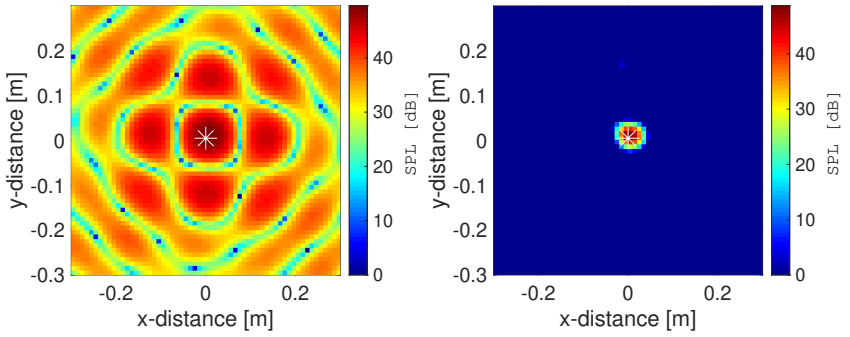

(a) (b)

Figure 4.9: Performance of Quadrupole Beamforming (a) and Quadrupole Functional Beamforming (b) ($\nu = 40$) on a Quadrupole Noise Source

4.2.2. Multiple Sources (Synthetic UAV)

The purpose of this section is to observe the potential effect of interference between these sources spaced close to each other for all the cases, being mono-, di-, and quadrupoles.

The benefits of developing the QB algorithm can be more objectively assessed when dealing with a multitude of sources positioned close to each other, as in the case for a drone. The results for direct CB, DB, and QB shall be presented, skipping the signal correction from [37], as the DPL implementation for both dipole and quadrupole has been proven correct by the results in subsection 4.2.1. The distance parameters have been chosen to match the μUAV. The reference monopoles have been selected as 60 dB. The dipole separation has been selected as $\mathbf{d} = [0, 0, 0.002]\,m$ in order to imitate the real-life directionality of this source on a rotor plane on the z-axis. However, for the quadrupole, the separation has been selected as $\mathbf{D} = [0.002, 0, 0]\,m$, which may or may not be the case in real situations. However they do satisfy the far field approximations $kd \ll 1$ and $kD \ll 1$ respectively, when plotted for $f = 2000\ Hz$.

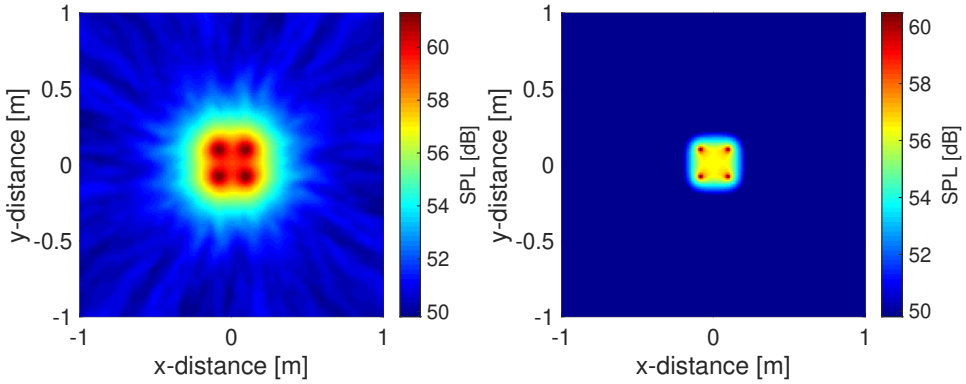

(a) (b)

Figure 4.10: Performance of Conventional Beamforming (a) and Functional Beamforming (b) ($\nu = 40$) on four Monopole Noise Sources

Figure 4.10 shows that CB and FB have a good performance and the locations and powers are accurately found for a set of monopole sources.

After creating the dipoles (see Figure 4.11), the same decrease in FB performance can be observed as in the case of one source. The location is indeed discovered, however, the powers are not accurate anymore. Applying DB on these dipole noise sources does however give good results (Figure 4.12). The beamforming outputs in both the conventional and functional case yield approximately the same values as the expected 37.3752 dB.

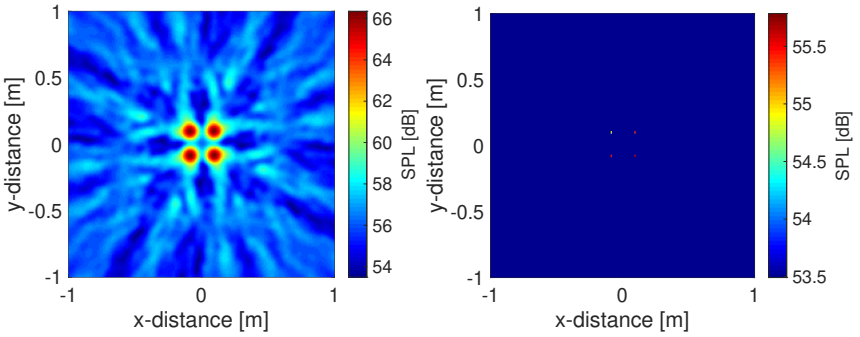

(a) (b)

Figure 4.11: Performance of Conventional Beamforming (a) and Functional Beamforming (b) ($\nu = 40$) on four Dipole Noise Sources

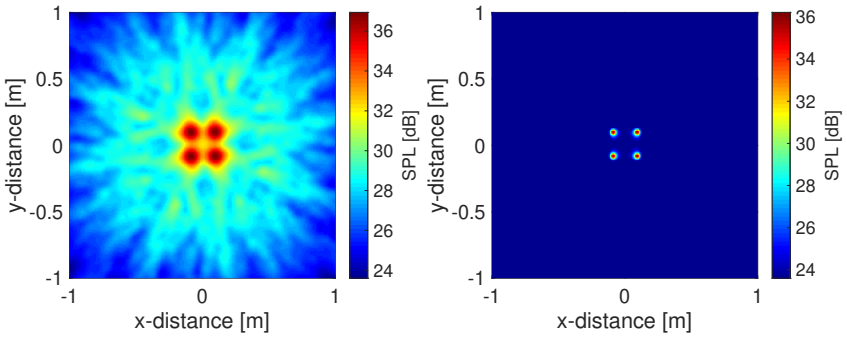

(a) (b)

Figure 4.12: Performance of Dipole Beamforming (a) and Dipole Functional Beamforming (b) ($\nu = 40$) on four Dipole Noise Sources

After creating the quadrupoles, the same decay in performance of the FB is observed, with inaccurate results (Figure 4.13). CB does, however, identify the locations of the poles with their deviation on the x-axis. However, the functional beamforming does not give accurate results.

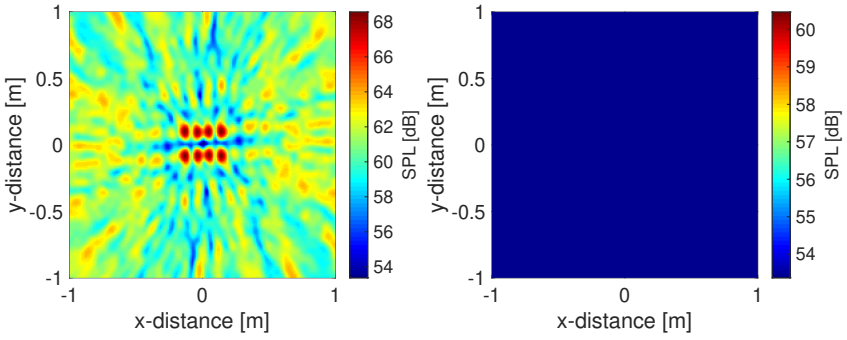

(a) (b)

Figure 4.13: Performance of Conventional Beamforming (a) and Functional Beamforming (b) ($\nu = 40$) on four Quadrupole Noise Sources

However, after applying the QB (Figure 4.14), the four quadrupole sources are correctly identified with a strength approximately equal to the expected 26.79 dB. The same can be observed for QFB, as well as the reduction of the side lobes appearing along the x-axis (due to the definition of **D**).

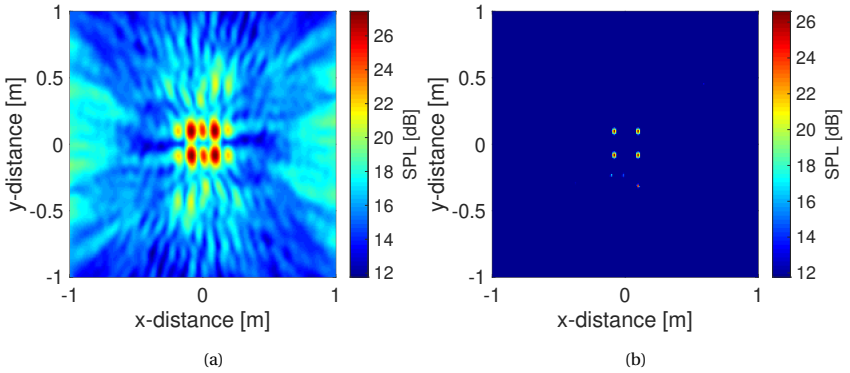

Figure 4.14: Performance of Quadrupole Beamforming (a) and Quadrupole Functional Beamforming (b) ($\nu = 40$) on four Quadrupole Noise Sources

4.2.3. Performance Assessment and Potential Error Sources

As concluded from related literature, drones contain a complex combination of noise sources. Due to this, the typical conventional beamforming might not be appropriate to accurately image these sources. Thus, when moving to real-life data, the monopole representation might not be good enough. Therefore, dipole and quadrupole beamforming have been implemented.

Regarding the dipole beamforming algorithm, its dependency on the prior knowledge of the real dipole positioning (knowing $\mathbf{d}$) should be noted. It is unlikely to have this knowledge beforehand, thus the approximation of this distance vector can be a source of errors in the output beamformer. These errors are also at risk of propagating (and possibly enhancing) to the quadrupole beamforming algorithm, as it follows the same methodology.

An interesting observation is the behavior of the FB as it does not perform well when the correct type of source is not accounted for. The location identification is unreliable and the strengths deviate greatly deviated from reality. When however, FB is coupled with either DB or QB (thus developing DFB and QFB) on dipoles or quadrupoles, respectively, it provides the best of both worlds. These combination output the correct strength and location, while greatly reducing the side-lobes occurring with these sophisticated algorithms. For a detailed performance of these algorithms on synthetic data for both the single source and the multi-source cases, Table 4.2 and Table 4.3 provide the deviation in dB of each algorithm from the calculated expected strength (according to subsection 3.3.5). Overall, the new algorithms are more efficient in the cases of their corresponding multipoles. Their performance is slightly decreased in the case of four sources as compared to a single source. However, this might be explained by the presence of interference between the sources.

		Monopole	Dipole	Quadrupole
Monopole Beamforming Techniques	Expected Strength [dB]	83	83	83
	Deviation CB [dB]	0	-1.22	-2.57
	Deviation FB [dB]	0	-78.2	-98.35
Dipole Beamforming Techniques	Expected Strength [dB]	-	60.38	60
	Deviation DB [dB]	-	-0.09	-1.98
	Deviation DFB [dB]	-	-0.09	-56.31
Quadrupole Beamforming Techniques	Expected Strength [dB]	-	-	49.80
	Deviation QB [dB]	-	-	-0.23
	Deviation QFB [dB]	-	-	-1.14

Table 4.2: Performance of all beamforming techniques on synthetic data: Deviation in dB from expected beamforming output values for a single source

		Monopoles	Dipoles	Quadrupoles
Monopole Beamforming Techniques	Expected Strength [dB]	60	60	60
	Deviation CB [dB]	1.3	6.34	8.56
	Deviation FB [dB]	0.48	-4.21	0.46
Dipole Beamforming Techniques	Expected Strength [dB]	-	37	37
	Deviation DB [dB]	-	-0.43	-0.1
	Deviation DFB [dB]	-	-1.15	13.83
Quadrupole Beamforming Techniques	Expected Strength [dB]	-	-	26.8
	Deviation QB [dB]	-	-	0.65
	Deviation QFB [dB]	-	-	-0.19

Table 4.3: Performance of all beamforming techniques on synthetic data: Deviation in dB from expected beamforming output values for a synthetic drone

4.3. Beamforming and Spectral Analysis on Real-Life Data

For a more in-depth look at how the noise behaves for each maneuver (i.e. hovering, flyovers, increasing altitude, decreasing slope flyover, various thrust settings), the beamforming plots and spectrograms have been examined in this section. First, the performance of all the beamforming techniques mentioned in section 3.3 will be tested on real-life data. Assessing this will help to decide which of the methods is, in the end, more appropriate to use for the rest of the analysis.

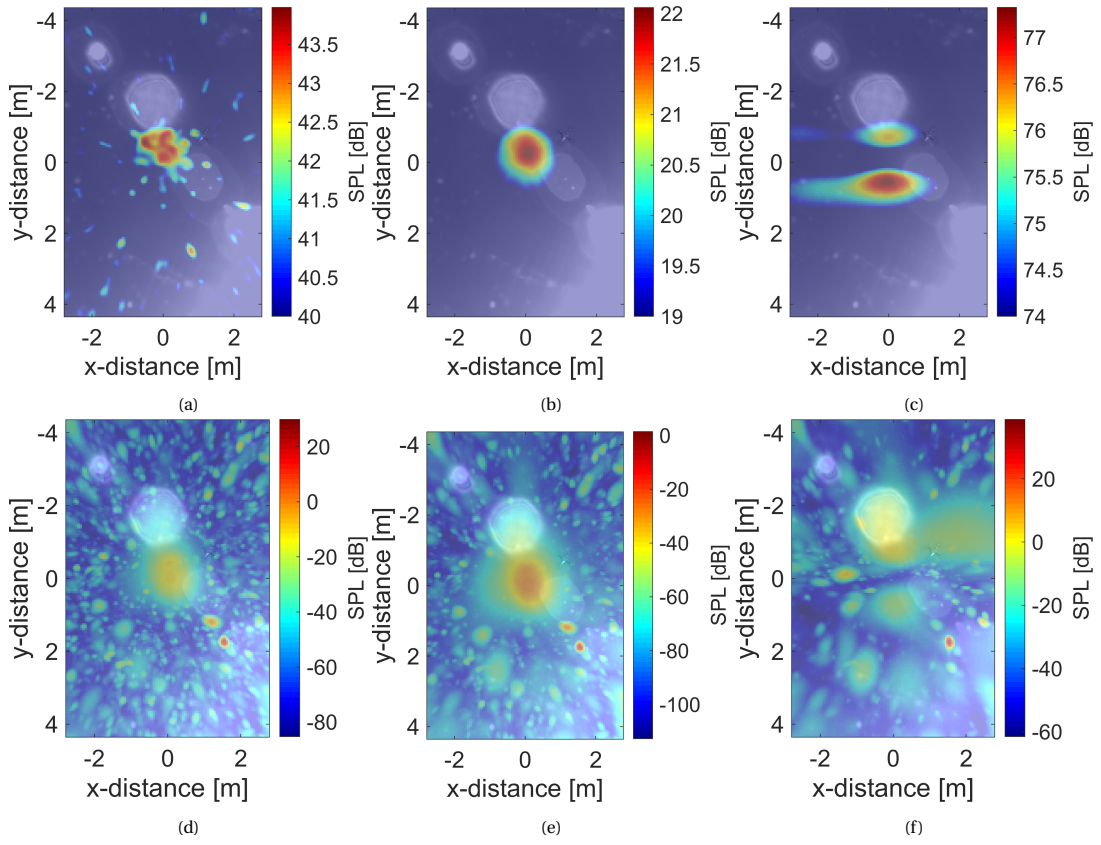

Figure 4.15: Comparison of different beamforming techniques on a hovering SUAV ($v = 30$) (a) CB, (b) DB, (c) QB, (d) FB, (e) DFB, (f) QFB.

Figure 4.15 shows a set of results that is representative for the full data set. The selected experiment is

captures the hover of the SUAV at approximately 10 m. CB presents satisfactory results. The drone and its rotors are distinguishable and the strengths reflect a situation in accordance with reality (see Figure 4.15a). However, FB (Figure 4.15d) does not identify the sources, and the strengths drop to negative values of SPL. For the DB (Figure 4.15b), although the location is still noticeable, some side-lobes overpower this location. In addition, the sources of the drone (the separated rotors) are not visible individually but appear grouped as one. DFB (see Figure 4.15e) exhibits a similar output as the FB, however, a slightly better localization is performed. The outputted sound levels are however negative. On the other hand, the QB is dependent on the quadrupole input distance. In these cases, $\mathbf{D} = [0, 0.002, 0]m$. This selection is visible in Figure 4.15c with a separation along the y-axis. A similar pattern is apparent in Figure 4.15f, but with even worse performance.

In stark contrast to the promising results on synthetic data of all beamforming algorithms, the accuracy of both Dipole Beamforming (DB) and Quadrupole Beamforming (QB), and their FB combinations, thus greatly decreases when analyzing real-life data.

To quantitatively assess the performance of all algorithms on real-life data, 25 samples from the measured experiments (as described in Appendix C) have been beamformed and the overall SPL in time domain has been calculated for the same time instant. Comparing the OSPL with the identified beamformer output in dB at the source, resulted in the deviations as shown in Figure 4.16. While most algorithms underestimated the source strength, CB appears to be the most robust method overall, however comprising deviations of about -25%.

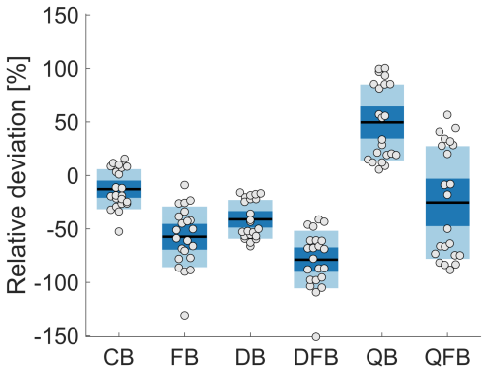

Figure 4.16: Performance of all beamforming techniques on the real-life measurements. Shown is the mean (solid line), the 95% confidence interval (dark blue) and the standard deviation (light blue). Individual measurements (see Appendix C) are shown as dots.

In conclusion, due to the sensitivity of the signals stemming from dipoles and quadrupoles to the angle of observation, interference, and distance between their poles, the performance of and QB algorithms greatly decreases. Although for the selected frequency range (200 to 3000 Hz) the Fresnel distance is not surpassed (the near-field is considered), it seems that the individual rotor sources in these measurements were small enough such that the multipoles can act as monopoles. In conclusion, the robust CB remains the method of source location identification on these UAVs. However, a considerable discrepancy regarding the actual noise levels should be expected.

CB is thus pursued in order to analyze individual operations, such as hovering and altitude change. First, the spectra will be plotted such that the frequency ranges of interest are identified. Afterward, the beamforming will be performed and the sources acknowledged from the plots.

4.3.1. Hover

The experimental measurements contain hovering maneuvers only for the MUAV and the SUAV. Thus only these two drones shall be analyzed in this section. Hovering is an operational maneuver specific to rotorcraft, which requires maintaining the same position for an extended period, by working with the rotary lift system.

Depending on the analyzed drone, a MUAV and a SUAV hovering at around 3 m show a similar pattern. Two frequency ranges of interest can be identified at [200 3000] Hz and [3000 7500] Hz since they seem to contain the most dominant signal strength.

As expected, the values will be higher for the bigger drone (green line in Figure 4.17), since it has to generate more lift to stay up in the same hovering position as the smaller drone (blue line). Furthermore, the pattern of the SUAV seems to be shifted to slightly lower frequencies.

Spectrograms from Figure 4.18 bringing forth the component of time as well, have shown to be consistent

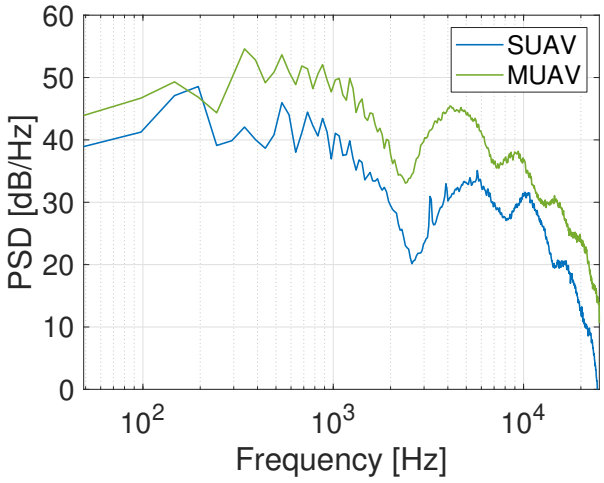

Figure 4.17: Spectral Analysis of SUAV (blue line) and MUAV (green line) hovering drones of different sizes at 3m

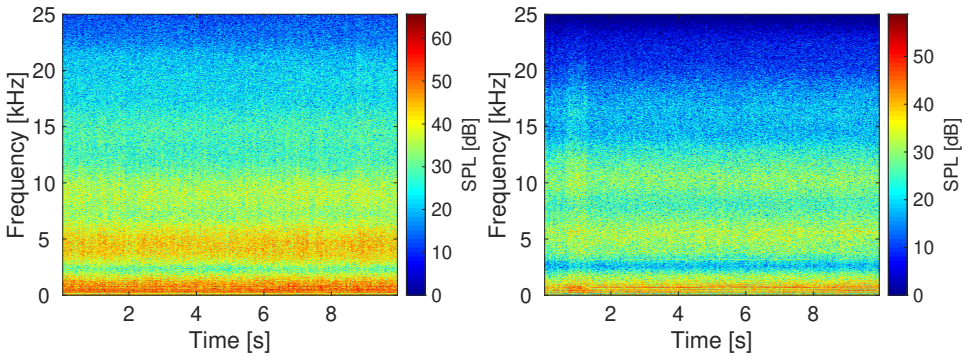

Figure 4.18: Spectrogram Analysis of hovering at 3 m for (a) MUAV and (b) SUAV

with the spectral plots as it can be noticed in the case of both drones in Figure 4.17. However, an interesting observation can be extracted regarding the blade passage frequencies. The predominant lines in the plots show the Blade Passage Frequency (BPF) of each rotor (Figure 4.19). In hover, the drone ideally uses consistent thrust levels throughout all its rotors. In this case, the BPF should be overlapping. However, in real life, as in this case with outdoor measurements, the effect of wind can be noticeable through the distinguishable BPFs for each of the rotors. Each rotor exhibits different thrust in order to counteract the wind and keep the vehicle as steady as possible.

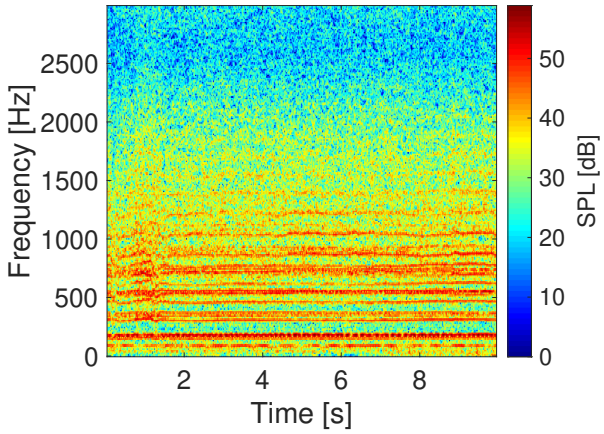

Figure 4.19: Hovering SUAV Spectrogram in [200 3000] Hz frequency range

Noise source locations are examined using beamforming techniques. Figure 4.20 shows the results for both the MUAV and the SUAV in hover performed with both CB and FB.The frequency range selected is 200 to 3000 Hz. The dynamic range of the color axis has been set to approximately 2 dB for all cases.

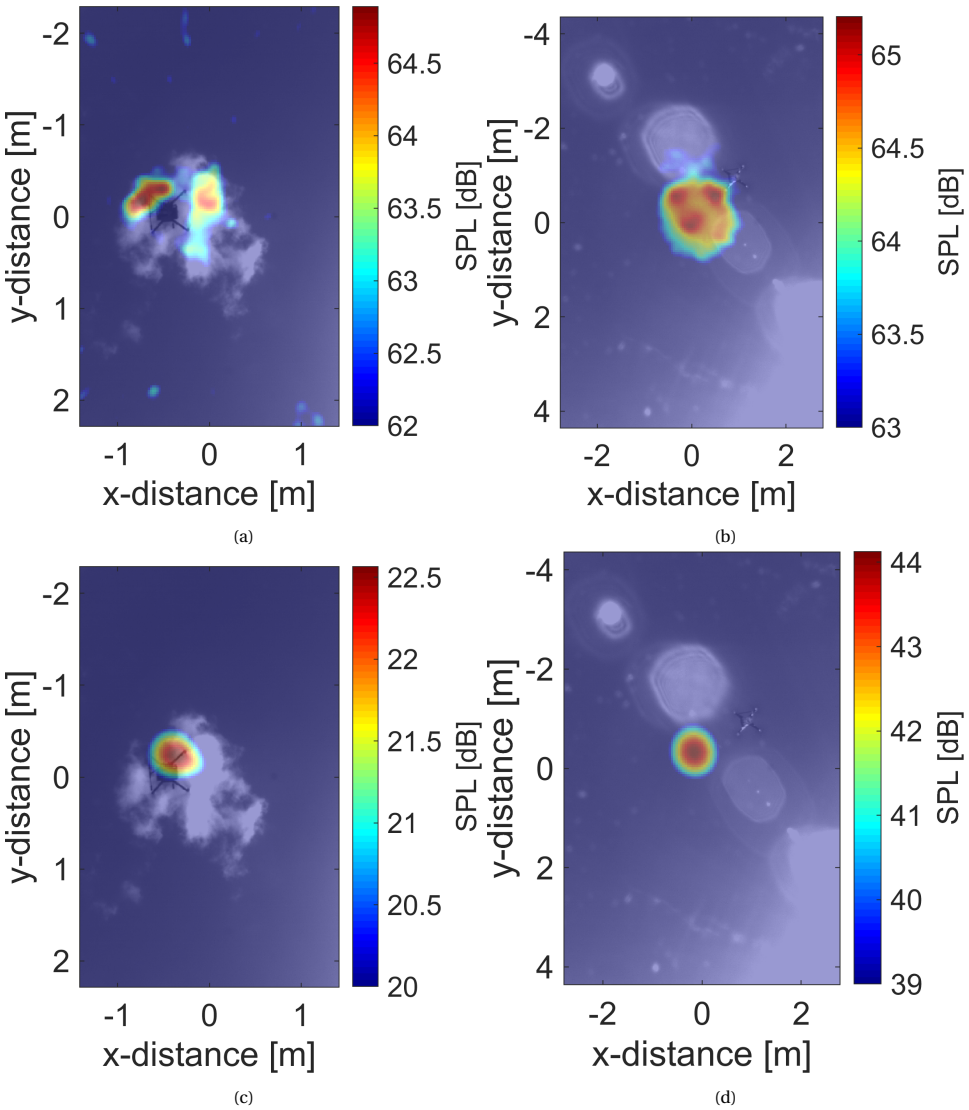

Figure 4.20: Conventional and Functional Beamforming ($v = 20$) of the MUAV (left) and SUAV (right) hovering at approximately 3m above the microphone array. There is a discrepancy between the values from CB vs FB in the the cases of both drones

CB reveals the noise sources on the UAVs, and as it seems, in the frequency range 200 to 3000 Hz, the rotors are the dominant source of noise. The drones have been correctly identified, but slightly more accurate for the MUAV (Figure 4.20a). For the SUAV, there seems to have been an issue related to the frame rate of the optical camera. Thus, there is no video snapshot perfectly corresponding to the same time instant used in the beamforming. The next frame was selected and thus there is a discrepancy in location (Figure 4.20b and Figure 4.20d).

FB on the other side, although the overall location is accurate, does cluster the sources together by identifying them as side lobes. This way, a broader main lobe is formed "integrating" the other 4 sources. This can be observed in both cases. In addition, the output beamforming powers are inaccurate. With the experience gained from testing synthetic data, this shows that indeed the noise sources on the drone are of a more complex type, and thus not only monopoles. Due to this, the FB performance greatly decreases.

Next, beamforming for the second frequency range will be performed. The spectrogram (Figure 4.18b)indicates that there is a lot of (experimental) noise in this range. This is indeed confirmed by the beamforming plots as no source can be pinpointed Figure 4.21. This means that further beamforming with this range is futile.

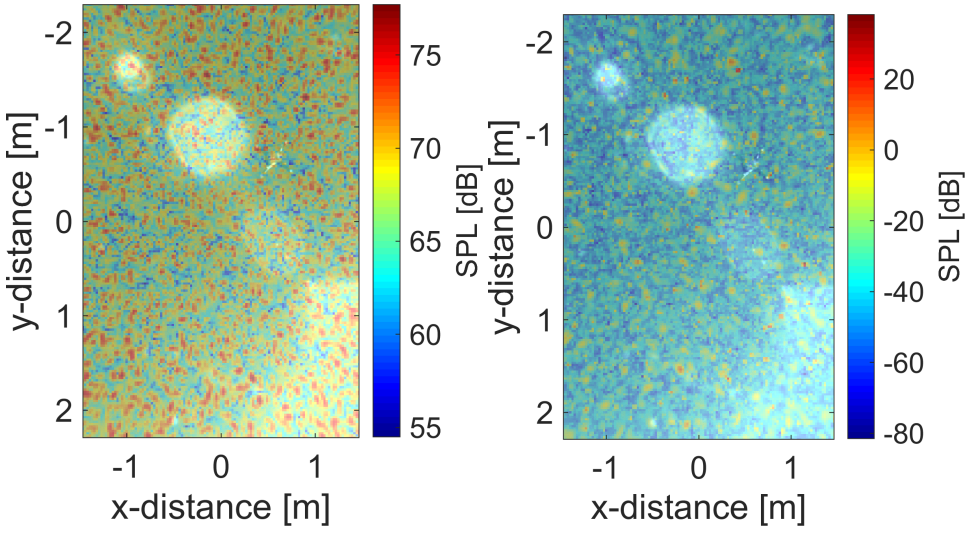

Figure 4.21: Conventional (left) and Functional (right) Beamforming ($\nu = 20$) on SUAV on [3000 7500] Hz range hovering at approximately 3m above the microphone array. The amount of broadband noise makes the identification of sources impetuous

4.3.2. Flyover

Noticeable, flyover maneuvers for SUAV and MUAV exhibit drastically different noise levels (Figure 4.22). However, it should be noted that the flyovers for the two different drones take place at different altitudes (unlike the analysis in hover at the same height). Although for lower frequencies the powers are similar, the differences start being noticeable after 1000 Hz, with a faster decay in the case of flyovers. Thus a hover is expected to have higher powers if analyzed at higher frequencies. This behavior is similar to manned aircraft as well. A prominent BPF harmonic at 6000 Hz in the case of the SUAV (Figure 4.22; blue line) is noted. The same BPF harmonic is noticeable in the spectrogram (Figure 4.23a). This occurrence might happen due to the increased thrust and thus higher Revolutions Per Minute (RPM) for each rotor. The higher RPM will result in higher frequency BPFs. In conclusion, beamforming shall also be applied to this 6000 Hz frequency.

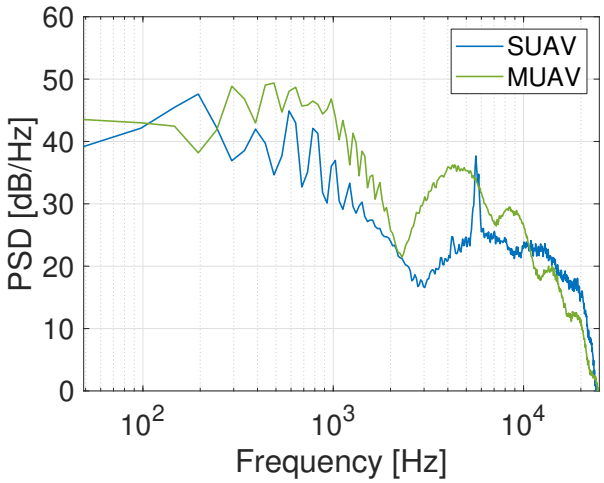

Figure 4.22: Spectral Analysis of SUAV (blue line) and MUAV (green line) flyovers

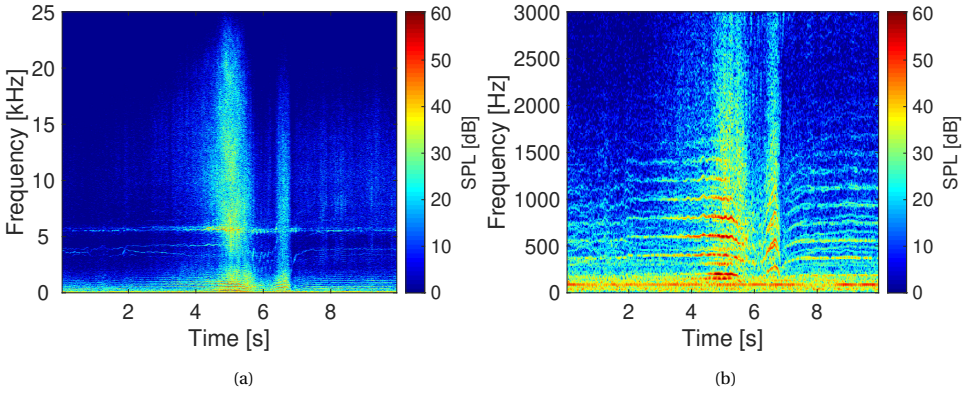

(a) (b)

Figure 4.23: Spectrograms (10 sec) of SUAV in flyover at 4 m at (a) full frequency range and (b) frequencies till 3000 Hz.

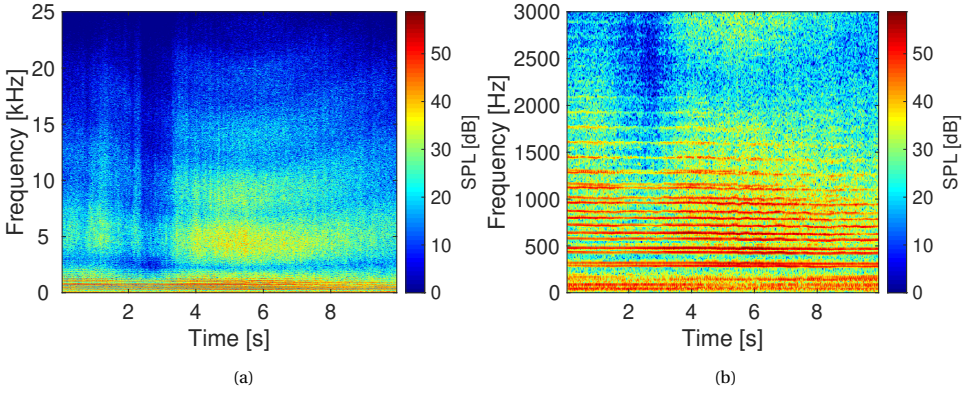

(a) (b)

Figure 4.24: Spectrograms (10 sec) of MUAV in flyover at 10 m at (a) full frequency range and (b) frequencies till 3000 Hz.

Figure 4.24 shows a different situation for the MUAV. The spectrogram is defined by the U-shaped patterns. These shapes might be the outcome of predominant broadband noise, occuring due to ground reflections. It creates destructive interference with the harmonics of the BPF and thus the harmonics are not distinguishable anymore. However, this only occurs at frequencies above 2500 Hz. Below this limit, the BPF harmonics are visible (see Figure 4.24b).

4.3.3. Change in Altitude

Due to the fundamental Rayleigh limit, a source moving away from its observer along the z-direction, changes its appearance from a noise source composed of four multipoles into a single monopole source. This quantity describes the distance between two sources for which they can still be resolved as individuals [38]. When the main lobes of two sources overlap, they create a combined, broader lobe which will make them indistinguishable from each other. The main lobe width is thus a factor in this limit. This main lobe width is determined by the aperture of the array as well as the frequency of interest [38, 12]:

$$RL = 1.22\frac{cz}{Lf} \tag{4.3}$$

where c is the speed of sound in the medium, z is the height of the source approximately above the measurement array, f is the frequency and L is the aperture of the array. In this thesis, the aperture of the array is the maximum diameter of the array (approximately 3.6 m). In the Fraunhofer approximation, the diffraction pattern of a circular aperture can be described analytically using the Bessel function of the first kind. Two sources can be resolved if the distance between them coincides with (or is further away than) the distance between the maximum and the first minimum of the diffraction pattern. These considerations applied to the Bessel function of the first kind give rise to the numerical factor 1.22 in Equation 4.3 [39].

For the low-frequency range used in the previous analysis (up until 2000 Hz), knowing the imposed Rayleigh distance and the length of the drone, the maximum height for which the sources can be resolved span from 0.83 to 12.5 m (lowest to highest frequency). Since the drone starts at a 3 m height, the sources can

be resolved only by using frequencies above 720 Hz. For an altitude of 10 m, the corresponding frequency is 2400 Hz and for 20 m and 30 m, the drone is already a point source. This behavior can be observed in Figure 4.25.

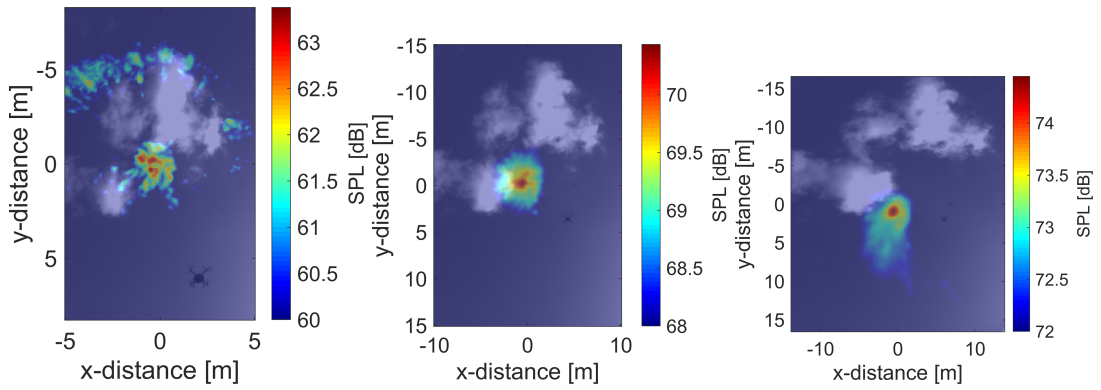

Figure 4.25: Conventional Beamforming on MUAV with increasing altitude from (a) 3 to 10 m, (b) 10 to 20 m, (c) 20 to 30 m. Note that the discrepancy in the location of the drone is caused by the frame setting of the optical camera.

In addition, it seems that with increasing altitude, frequencies below 200 Hz seem to become the most dominant range (Figure 4.26).

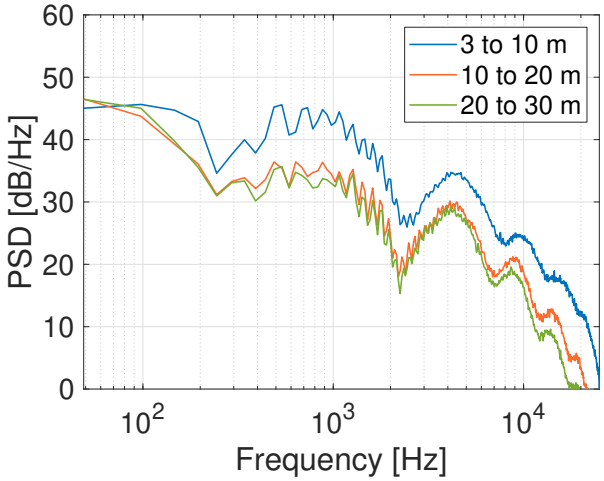

Figure 4.26: Spectra of MUAV increasing in altitude from 3 to 10 m (blue line), 10 to 20 m (orange line), 20 to 30 m (green line).

Upon descend of the drone, the same dominant low frequencies are present (Figure 4.27), with the PSD decaying across the whole spectrum. As expected, the overall PSD increases with decreasing height, and vice versa for increasing height (Figure 4.26).

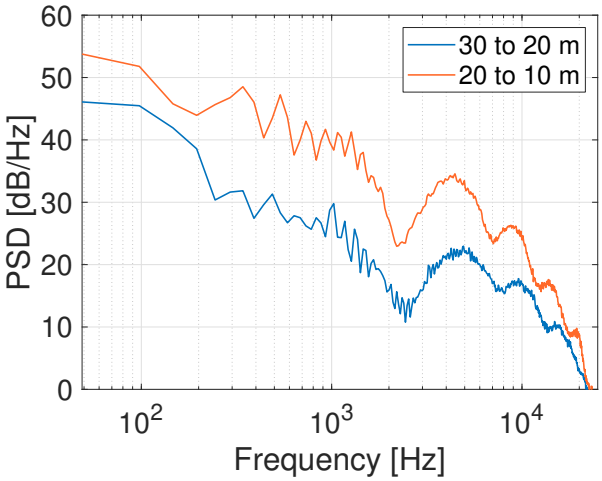

Figure 4.27: Spectra of MUAV in decreasing slope flyovers from 30 to 20 m (blue line) and 20 to 10 m (orange line).

4.4. Assessment of Appropriate Modeling Parameters

In this section, the assessment of appropriate modeling parameters shall be discussed, starting with the design parameters. Afterward, the influence of operational parameters (such as distance, angle of observation and thrust settings) are assessed.

4.4.1. Design Parameters

Design parameters, such as the overall size of the drone or the number of rotors can greatly influence its noise characteristics. Therefore, this section will present how noise behaves with changes in parameters. The candidates for this analysis were chosen such that the rest of the overall contextual parameters are the same except these design parameters.

The MUAV and the SUAV have been flown at the same height in roughly the same weather conditions in a hovering operation. Thus, the difference between the two drones from a size point of view can be assessed. All metrics appear to be consistent with expectations (Table 4.4). The roughness is greater for the smaller drone, while the complementary fluctuation strength is smaller. For this drone, the tonality also has higher values, implying non-uniform rotational speeds of the rotors, as tones are harmonics of the BPFs of the rotors. This might either be due to deviations from an idealistic design of the drone or to the wind during the measurements. Due to its size, the medium drone is louder, also leading to higher values of the OASPL and of the Psychoacoustic Annoyance . With respect to Sharpness, the difference between the two drones is insignificant.

Drone:	MUAV	SUAV	Relative Difference (%)
Roughness (R_5) [asper]	0.47	0.60	+27.69
Fluctuation Strength (FS_5) [vacil]	0.10	0.04	-59.98
Tonality (K_5) [t.u.]	0.14	0.15	+5.17
Loudness (N_5) [sone]	24.17	19.95	-17.44
Sharpness (S_5) [acum]	1.99	1.93	-3.11
Psychoacoustic Annoyance (PA)	43.60	35.90	-17.65
OASPL [dBA]	68.94	65.64	-4.78

Table 4.4: Size Difference Influence on Values of Noise Spectral Characteristics for hovering MUAV and SUAV at 3 m above microphone array

4.4.2. Operational Parameters

The contextual parameters are likewise analyzed to assess their impact on the sound behavior. Monopoles, dipoles, and quadrupoles all behave differently with varying distances and angles of observation. In addition, thrust is also expected to influence this behavior.

Distance

The most accurate log files are available for the MUAV and thus, in consequence, these will be used for this analysis. The distance for every log sampling point is computed, binned and the mean OSPL of each bin is computed. Figure 4.28 shows the relation between the distance and the OSPL.

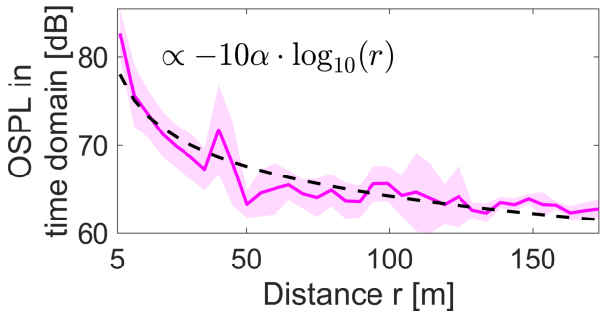

Figure 4.28: Relationship between distance and OSPL. The lighter area represents the variance of the OSPL value for each distance bin. This difference in levels is explained by the angle of observation, and the fact that the drone is not an omnidirectional source

Overall, the OSPL decreases with increasing distance. The sound intensity $I = W/(4\pi r^2) \propto p^2$ depends on the inverse squared distance. Therefore, the pressure p scales with the inverse distance ($p \propto r^{-1}$) and the OSPL, according to Equation 2.3, evaluates as

$$OSPL(r) \propto -\alpha \cdot 10\log_{10}(r), \tag{4.4}$$

where $\alpha = 2$ in theory. Unexpectedly however, the experimental data is best described by a value $\alpha = 1.13 \pm 0.08$, thus indicating that the pressure depends on the distance approximately as the inverse square root ($p \propto r^{-1/2}$). The OSPL thus decays slower over distance as expected, giving rise to a higher noise level at larger distances. This result, if further confirmed, indicates a considerable noise load even if drone are seemingly far away.

The variance in SPL levels per bin can be explained by considering the angle of observation. Since an UAV is composed of multipole sources, the radiated intensity varies with the observed angle. Thus, at the same distance, different values of noise can be perceived, depending on the observation position.

The effects of distance on noise metrics were computed per type of drone Table 4.4. This shows the relative increase or decrease in the values of the sound quality metrics in hovering at 3 m versus at 10 m above the microphone array. As expected, most metrics show a decrease in values in the case of both drones. The only metric which exhibits a contrary behavior is the Tonality (K_5). An explanation for this might be related to the presence of slightly stronger winds at higher altitudes. The winds would cause the drone to exert different RPM for each rotor in order to stabilize and maintain a constant position. This leads to different BPFs and BPF harmonics for each drone, creating a series of distinguishable tones in the spectra.

The difference in wind strength at these two heights can also explain the undeniable contrast in the relative difference of the OASPL between the 2 drones. From Table 4.5, the MUAV will exhibit a significant drop of the OASPL with increasing height while, for the SUAV it remains approximately constant. The SUAV might need to exert stronger thrust on the rotor in order to counteract the wind effect. This would inadvertently lead to higher values of the OASPL.

Drone:	Relative Difference (%) MUAV	Relative Difference (%) SUAV
Roughness (R_5) [asper]	-8.76	-13.10
Fluctuation Strength (FS_5) [vacil]	-39.03	-55.28
Tonality (K_5) [t.u.]	+6.66	+1.33
Loudness (N_5) [sone]	-36.26	-21.69
Sharpness (S_5) [acum]	-3.97	-25.18
Psychoacoustic Annoyance (PA)	-37.05	-23.21
OASPL [dBA]	-11.66	-0.64

Table 4.5: Influence of Distance on Values of Noise Spectral Characteristics for hovering MUAV and SUAV at 3 m vs 10 m above microphone array

Angle of Observation

Since the research is dealing with various multipoles, the angle of observation shall result in a multitude of different powers from the beamforming image for the same source. Using the available log files, the OSPL can be segmented per angle of observation. To find the corresponding angle of observation in the log file, the previously computed distance r is used alongside the available height values, z, using

$$\theta = \arcsin\left(\frac{z}{r}\right) \tag{4.5}$$

where $\theta = 90°$ corresponds to the drone being directly above the array. The relationship between distance, angle and OSPL is visualized in Figure 4.29.

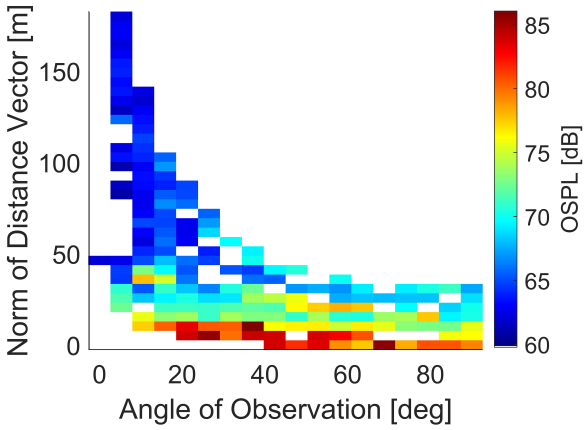

Figure 4.29: Relationship between distance, angle of observation and OSPL

Since the largest range of angles was available for distances of approximately 30 m, a polar plot to construct the radiation in the southern hemisphere of the UAV was envisioned (Figure 4.30).

As expected, the closer the source, the stronger the sound. It is interesting to notice slightly higher values of OSPL for the angles between 40 and 60 degrees (with a peak at approximately 54 degrees) rather than overhead, as initially expected. This might be due to the whole drone acting as a quadrupole radiator (due to the four rotors).

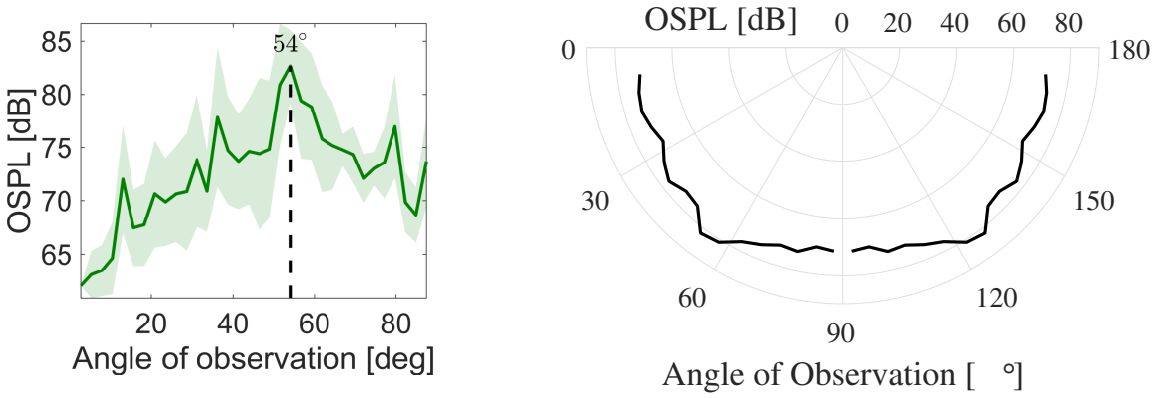

Figure 4.30: Sound Radiation Plotted over the Angle of Observation (left) and in the Southern Hemisphere (right) of a MUAV at an Observation Distance of Approximately 30 m.

Thrust / Engine Power / Velocity

The dependency of drone noise on thrust can be especially observed from the SUAV's two fly-overs at 4m. One was done using a normal throttle setting (actual velocity unknown), while the latter was performed at full throttle, generating a velocity at around 16 m/s.

Thrust:	Normal Thrust Setting	Full Thrust Setting	Relative Difference (%)
Roughness (R_5) [asper]	0.24	0.22	-7.95
Fluctuation Strength (FS_5) [vacil]	0.34	0.50	+48.98
Tonality (K_5) [t.u.]	0.21	0.20	-8.61
Loudness (N_5) [sone]	17.46	19.40	+11.09
Sharpness (S_5) [acum]	2.35	2.03	-13.37
Psychoacoustic Annoyance (PA)	37.06	37.03	-0.09
$OASPL$ [dBA]	64.22	71.98	+12.07

Table 4.6: Values of Noise Spectral Characteristics for SUAV Flyover at 4m with different Thrust settings

Table 4.6 shows that except for an increase in loudness and fluctuation strength, the other sound quality metrics seem to be lower in the full thrust case. The OASPL however exhibits a 12% increase. This is a significant difference and it is an important observation as the A-weighted scale best resembles the human perception. However, the psychoacoustic annoyance seems to not differ critically, while the perception differs greatly (but subjectively) when listening to the recorded acoustic files. This might insinuate that the current Psychoacoustic Annoyance calculation might not be fit to accurately portray the effects of drone noise.

Figure 4.31 shows in both cases a dominant harmonic of the BPF visible at around 6000 Hz. When beamforming around this frequency (5000 to 6000 Hz range), the broadband noise is too dominant and thus the source is not identifiable (see Figure 4.32).

4.5. Sound Quality Metrics

The metrics have been computed using the Audio Assessment Model as developed in [10]. The selected time range in all presented cases is 2 seconds and most of the metrics are the values of the metrics exceeded 5% of the time. The results for all maneuvers have been plotted per metric. This way, a sense of how the context influences the output value for a metric is created. To this list of measurements, the recording of a vacuum cleaner measured from 20 cm away, as well as an aircraft fly-over have been added (marked with yellow and respectively blue stars). The altitude of the measured aircraft is unknown. This was done to give a sense of the viable metric ranges when comparing the sounds to familiar noises from day to day life. A first observation in all plots is the effect of altitude on the SPL. This lies in shifting the plots upwards on the Y-axis with smaller heights. This is quite straightforward as lower altitudes would imply a smaller distance to the sensors.

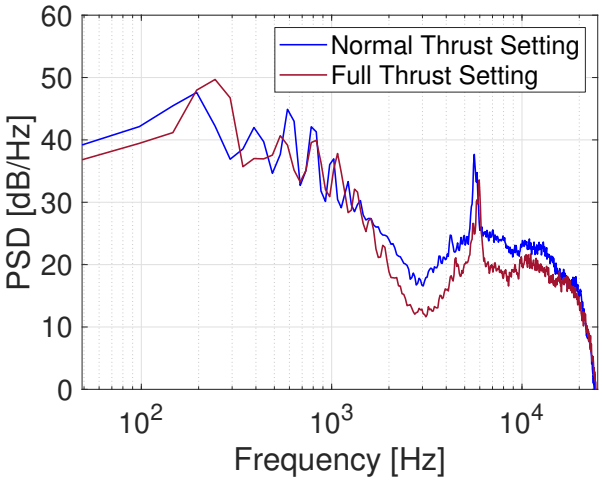

Figure 4.31: Spectra of a SUAV in normal (blue) vs full thrust (red) setting flyover

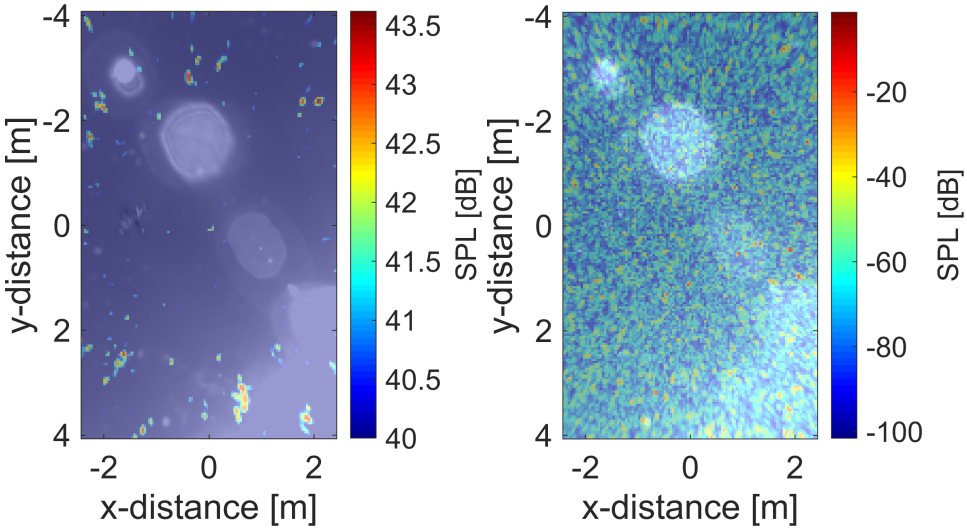

(a) CB on Hovering SUAV (b) FB on Hovering SUAV

Figure 4.32: Conventional (left) and Functional (right) Beamforming on [5000 6000] Hz range of SUAV in full thrust. The amount of broadband noise makes the identification of sources impossible

4.5.1. Roughness

In general, flyovers (Figure 4.33: yellow markers) present lower roughness than hovers (blue markers). This means that in hover, the perceived loudness fluctuates more. This is due to the static nature of the hover in time, as opposed to the short exposure of the microphones during a fly-over.

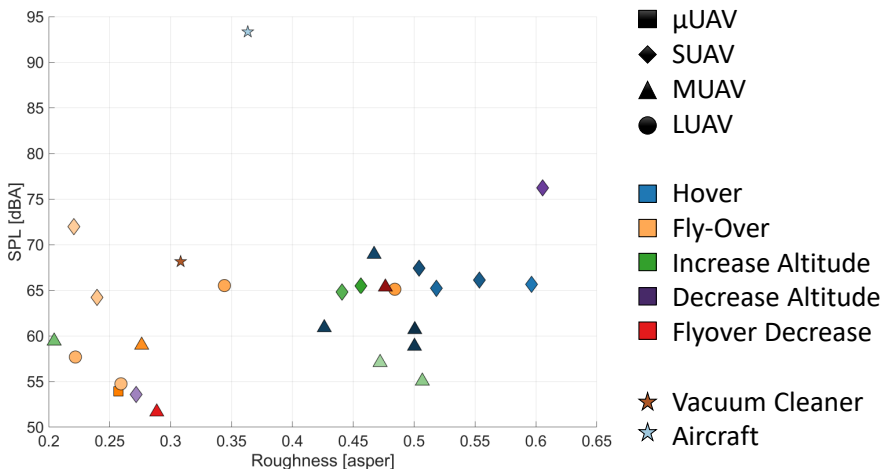

Figure 4.33: Roughness vs OASPL of Measured Maneuvers (Colors - Hovers: blue; Flyover: orange; Altitude Decrease: red; Altitude Increase: green; Change in Maneuver: Purple; Shapes - μUAV: square; SUAV: diamond; MUAV: triangle; LUAV: circle)

4.5.2. Fluctuation Strength

It is expected that the Fluctuation Strength will behave in an antagonistic way to the roughness. By comparing the two metrics (Figure 4.33 and Figure 4.34), indeed such behavior is observable, as most of the measurement cluster to the left side of the fluctuation plot. Out of all maneuvers, it seems that the outliers are the SUAV's flyovers at both half and full thrust, which seem to have less roughness and more fluctuation strength. This might be the case due to the non-static behavior of the flyover, and thus less exposure of noise on the sensors. Another explanation for this behavior might be the varying thrust that these maneuvers exhibit which is unique to them in comparison to the other cases.

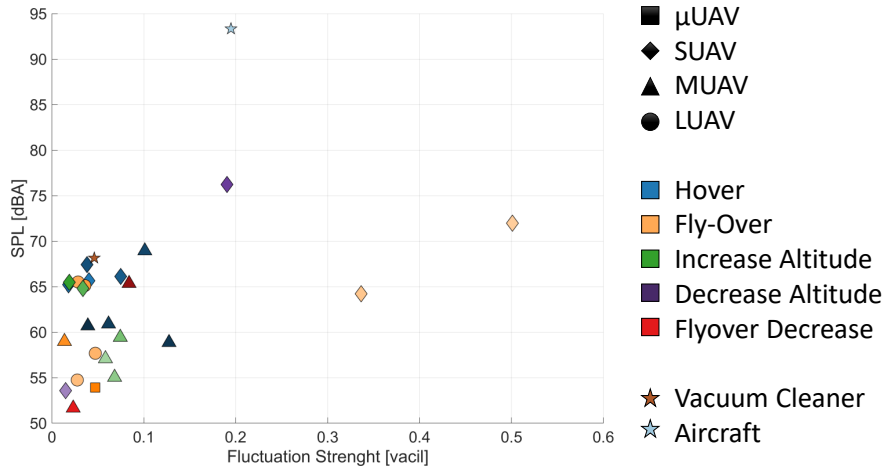

Figure 4.34: Fluctuation Strength vs OASPL of Measured Maneuvers (Colors - Hovers: blue; Flyover: orange; Altitude Decrease: red; Altitude Increase: green; Change in Maneuver: Purple; Shapes - μUAV: square; SUAV: diamond; MUAV: triangle; LUAV: circle)

4.5.3. Tonality

For tonality, it appears that hovers exhibit lower values, followed by altitude increasing operations and lastly by flyovers (Figure 4.35). This outcome could be explainable by the increased thrust of the rotor to produce the forward motion. The rotors will not present the same RPM and thus the BPF and their harmonics will be distinguishable per rotor at different tones, and thus increasing the tonality of the sound.

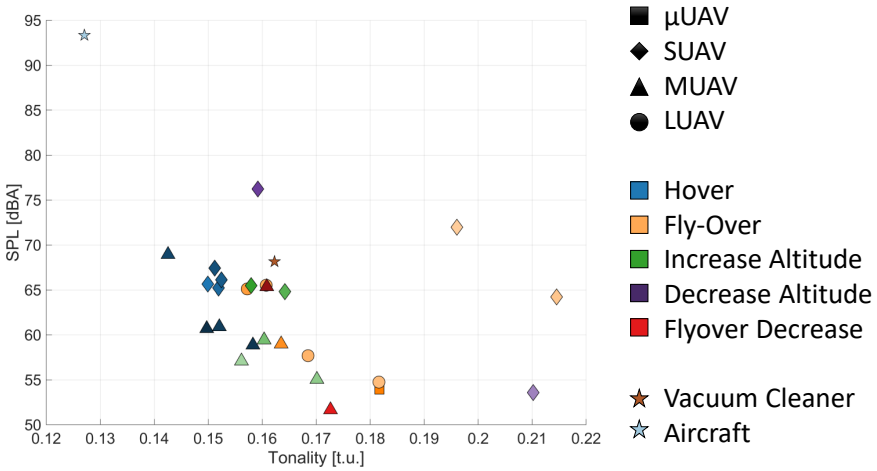

Figure 4.35: Tonality vs OASPL of Measured Maneuvers (Colors - Hovers: blue; Flyover: orange; Altitude Decrease: red; Altitude Increase: green; Change in Maneuver: Purple; Shapes - μUAV: square; SUAV: diamond; MUAV: triangle; LUAV: circle)

4.5.4. Loudness

In the case of loudness, the results, as can be noticed in Figure 4.36, present a logarithmic behavior in relation to the OASPL. This is a straightforward conclusion as both these metrics are loudness metrics exhibiting similar behavior.

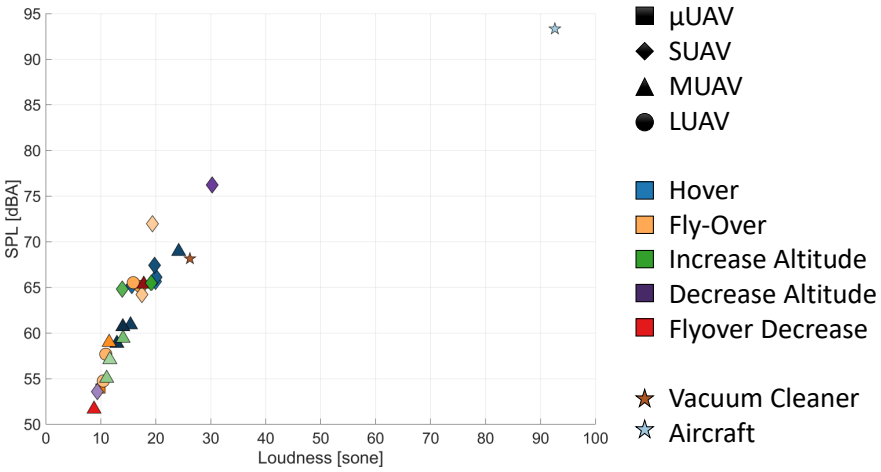

Figure 4.36: Loudness vs OASPL of Measured Maneuvers (Colors - Hovers: blue; Flyover: orange; Altitude Decrease: red; Altitude Increase: green; Change in Maneuver: Purple; Shapes - μUAV: square; SUAV: diamond; MUAV: triangle; LUAV: circle)

4.5.5. Sharpness

The sharpness (Figure 4.37) brings forth a new dimension to the discussion, namely that of size. This pattern can be observed as the smaller lighter drones exhibiting sharper characteristics than the larger heavier drones. This suggests that smaller drones will exhibit high rather than low-frequency content and a more 'bee-like' sound. The sharpness of the aircraft confirms this behavior as it is the lowest.

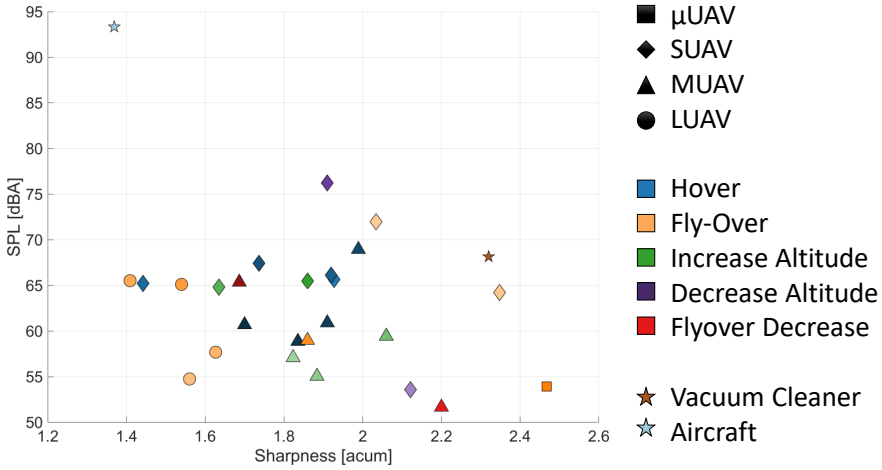

Figure 4.37: Sharpness vs OASPL of Measured Maneuvers (Colors - Hovers: blue; Flyover: orange; Altitude Decrease: red; Altitude Increase: green; Change in Maneuver: Purple; Shapes - μUAV: square; SUAV: diamond; MUAV: triangle; LUAV: circle)

4.5.6. Psychoacoustic Annoyance

The psychoacoustic annoyance is incorporating previously analyzed sound quality metrics. It is a multiple of loudness with a coefficient that describes the effects of the other metrics. The loudness has the heaviest weight in the calculation of this annoyance. Thus it shall also exhibit a logarithmic behavior with respect to the OASPL (see Figure 4.38) as in the case of loudness. This calculation of annoyance might not be suitable for drones which are not as loud in comparison to aircraft. This does not however invalidate their annoyance. This could be corrected probably by offering more weighting to the roughness element. This modification to the calculation is however deviating too much from the scope of this thesis.

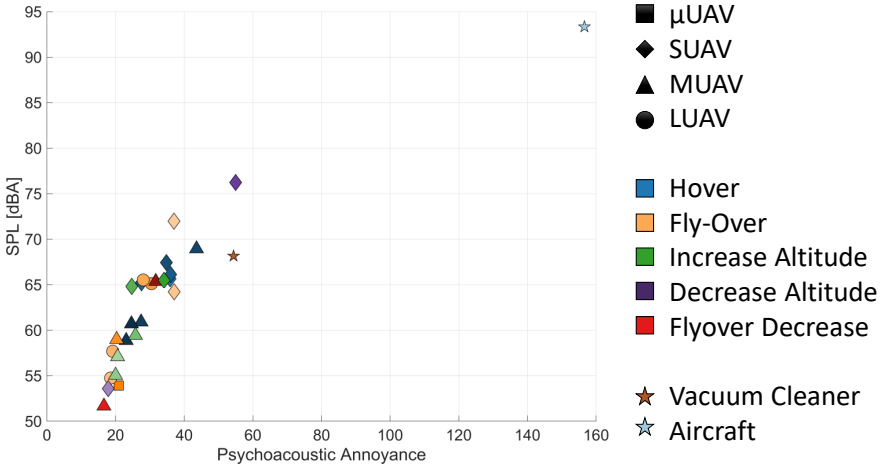

Figure 4.38: Psychoacoustic Annoyance vs OASPL of Measured Maneuvers (Colors - Hovers: blue; Flyover: orange; Altitude Decrease: red; Altitude Increase: green; Change in Maneuver: Purple; Shapes - μUAV: square; SUAV: diamond; MUAV: triangle; LUAV: circle)

Another observation regards the sudden decrease in altitude of the SUAV as it has shown interesting noise characteristics throughout all the plots. This can be explained by the broadband noise that might have been created. As the rotor's RPM is suddenly decreased, the weight of the drone is bringing it down. The influx of air

going in a counter direction to the still (but slowly) rotating propellers creates a high amount of turbulence. Hence, this turbulence generates these high amounts of broadband noise.

4.6. Concluding Remarks

This chapter presented the overall results of analyzing drone noise for varying maneuvers and operational contexts, including the performance of beamforming techniques on these vehicles. Despite the expected complexity of drone noise, CB is still outperforming more sophisticated algorithms, although the latter ones have shown great potential when tested on synthetic data. This unfortunate situation can, however, be explained as being the cause of DB's and QB's dependency on a pre-known directionality of the noise source and the distance between these poles. However, the available plots have shown the present noise sources for two frequency ranges, [0 to 3000] Hz and [3000 to 7500] Hz. It is noticeable that the clear noise sources are distinguishable in the first frequency range and less on the latter. The latter seems full of experimental noise and the sources, including the whole drone, are unidentifiable. Nonetheless, the spectra have been analyzed and the metrics have been computed for different parameters, and thus a full picture of the situation can be drawn. This can help put in place a suggested noise model.

The presented and applied analysis may suffer from various influences such as the quality of the measurement data to the limits of the applied beamforming algorithms. When considering the Scan Grid Estimator used to set the scan plane for the beamforming plots, this function might also give inaccuracies in estimating the x and y boundaries of the scan grid, as sometimes the video data is not sufficient for an accurate estimation (low frame rate, fast unsteady drone), or the quality of the camera is too low (high exposure, too much light, too cloudy). That is however only reasonable if one can assume that the drone altitude doesn't change much within 30 frames (1 s for a frame rate of 30 Hz, thus indeed reasonable).

Concerning the implemented algorithms, the *a priori* definition of the multipole positioning is an origin for possible errors, as the angle of observation is crucial in these methods. This aspect coupled with the presence of experimental noise in the real-life measurements hinders a proper performance of these analyzed imaging techniques.

5

Conclusions and Recommendation

5.1. Appropriate modeling parameters

An understanding of the interesting modeling parameters is established throughout this thesis. Thus, some of these variables can be selected for a future empirical model. This section shall expose these variables, explain their choice and the modalities of calculating them if they are not readily available.

It seems that some of the most important parameter which influences noise behavior is distance. The angle of observation also has a slight influence however not as impactful as distance. These are followed by the thrust of the vehicle, which is a relation between the velocity (or either Mach or propeller RPM) and the mass of the vehicle. In consequence, this implies the effects of the number of rotor/blades of the drone as these are proportional to the amount of thrust the vehicle achieves. Last but not least the atmospheric conditions must be taken into account. All the influencing variables will be described here and categorized.

5.1.1. Variable Definition

A first step in defining a model is deciding which are the appropriate dependent and independent values. This way, it is known before the experiment which factors must be taken into consideration. The variables are presented in Table 5.1. Some basic parameters present in the table are explained in paragraphs **Atmospheric Factors**, **Directivity Index** and **UAV dimensions and specifications**. These are parameters computed relative to the experimental context.

Atmospheric Factors

Using the flight altitude, as well as the atmospheric conditions on the day of the experiment (i.e. temperature, humidity, wind direction, and velocity), the speed of sound (c), air density (ρ_∞) and atmospheric sound absorption (α_{atm}) coefficient are computed according to [40].

The absorption coefficient is a function of frequency f and also depends on temperature *Temp* and relative humidity *RH* as can be seen in Appendix D.

Directivity Index

The directivity index is a function of θ, the angle radiation, as it is determined by deducting the steered SPL from the average SPL. However, it can also be determined from the radiated intensity [41] by using the intensity at a certain angle θ and the mean acoustic intensity of the source (I_{av}) [12].

$$DI(\theta) = 10\log_{10}\frac{I(\theta)}{I_{av}} \tag{5.1}$$

To determine this Directivity index, The SPL is used to determine the Power Watt Level (PWL) [12]:

$$\text{SPL}(r) = \text{PWL} - 10.8 - 20\log_{10}(r) - \alpha_{atm} r \Rightarrow \text{PWL} = \text{SPL}(r) + 10.8 + 20\log_{10}(r) + \alpha_{atm} r \tag{5.2}$$

where α_{atm} represents the atmospheric sound absorption coefficient and r is the distance between the source and the microphone array. Next, the acoustic power can be determined [12].

$$\text{PWL} = 10\log_{10}\left(\frac{W}{W_0}\right) \tag{5.3}$$

with $W_0 = 10^{-12}$ Watts, the reference acoustic power [12].

From this, by dividing by $4\pi r^2$, the radiated intensity specific to either monopole, dipole or quadrupole noise source can be computed. This intensity stands for the I_{av} in the directivity index equation. In order to determine the $I(\theta)$, first the volume velocity Q can be determined for the selected frequency band for either the monopole, dipole or quadrupole [12] by using the acoustic power W from Equation 5.3:

$$Q_{Mono} = \sqrt{\frac{8W\pi c}{\rho_\infty \omega^2}} \tag{5.4}$$

$$Q_{Di} = \sqrt{\frac{24W\pi c^3}{\rho_\infty \omega^4 d^2}} \tag{5.5}$$

$$Q_{Qua} = \sqrt{\frac{60W\pi c^5}{\rho_\infty \omega^6 d^2 D^2}} \tag{5.6}$$

With the appropriate Q, the θ dependent intensity ($I(\theta)$) can be computed for angles from 0° to 360° for each pole case using Equation 2.16 for the monopole case, Equation 2.20 for the dipole situation and Equation 2.25 for the quadrupole case. Knowing the angle dependent intensities and the average intensity, the directivity index can be computed, depending on the type of noise source which the user desires to take into consideration. The directivity index can be used to compute the SPL depending on the angle of observation.

UAV dimensions and specifications

The mass, diameter of rotors, number of blades and rotors must be documented as they are used in relation to the other variables. Among these, the distance to microphones, vehicle velocity and the number of revolutions per minute per rotors would be an advantage. However, in some cases, this is not possible in the experiments without pre-conceived log files on drones' positions and metrics. Thus, in case of absence, for the distance, the altitude shall be considered. The revolutions can be determined by checking the spectrogram and noting the frequencies at which the fundamental BPF appears. Using Equation 5.7 (where f_1 is the fundamental BPF, B is the number of blades per rotor and RPM is the number of revolutions per minute) the RPM is approximately determined [12].

$$f_1 = N_b \frac{RPM}{60} \iff RPM = \frac{60 f_1}{N_b} \tag{5.7}$$

In case that the BPF is not readily available, it can be determined using the methodology from [36]. This method begins by selecting the overhead time from the spectrogram, and afterwards averaging the Doppler-corrected spectra over time. A polynomial fit is applied to this average, the resulting polynomial is subtracted from the spectrum and the difference is squared to clearly identify the peaks. Three methods can be used subsequently to determine the most likely BPF candidates. The candidates are filtered by either selecting the BPF with most harmonics explained or by the maximum correlation with the given experimental data. These methods will not be further explained as they exit the scope of the study. However, this shows that the RPM can be computed by analyzing the data in case the exact values are not found in the drone log files.

5.1.2. Dependent vs. Independent Variables

Table 5.1 lists both independent and dependent variables suitable for a future drone noise model.

The tip Mach Number is dependent on the diameter, speed of sound and revolutions per minute of the blade as can be noticed in its equation. Thus, with all these variables known, the tip Mach Number M_t can be easily determined

$$M_t(Diam, c, RPM) = \frac{\pi \times Diam}{c} \frac{RPM}{60} \tag{5.8}$$

Next, for hover conditions, the thrust can be determined according to

Independent Variables		Dependent Variables	
Distance to Microphone Array [m]	r	Tip Mach Number	$M_t(Diam, c, RPM)$
Diameter of Rotor [m]	$Diam$	Thrust [N]	$TR(m, g)$
Number of Rotors	N_r	Air density dependent coefficient	$\eta(\rho_\infty)$
Revolutions per Minute [rpm]	RPM	Engine Power [kW]	$P_{br}(TR, V)$ or $P_{br}(TR, \eta, Diam)$
Number of Blades	N_b		
Mass [kg]	m		
Vehicle Velocity [m/s]	V		

Table 5.1: Independent and Dependent Variables for a Future Drone Noise Model

$$TR(m, g) = m \times g_{acc} \tag{5.9}$$

where g_{acc} is the gravitational acceleration computed according to the geographical positioning and m is the mass of the drone. Both variables are available.

Depending on the availability of data, such as velocity (V) and thrust (TR), the engine power (P_{br}) can be determined according to

$$P_{br}(TR, V) = TR \times V \tag{5.10}$$

If the velocity is not known, then the engine power can be determined using a different set of variables:

$$P_{br}(TR, \eta, Diam) = \eta \cdot \frac{TR^{3/2}}{Diam/2} \tag{5.11}$$

where $Diam$ is the rotor diameter and η is an air dependent coefficient:

$$\eta(\rho_\infty) = \sqrt{\frac{1}{2\pi\rho_\infty}} \tag{5.12}$$

The derivation for P_{br} and η can be find in Appendix E.

Suggested SPL Equation

With all the variables set up, a suggested equation of the modeled SPL can be built based on previous propeller noise models [12]. The equation takes the form:

$$\begin{aligned} SPL(\theta, r) = & \\ & \Gamma_0 + \Gamma_1 \log_{10} P_{br} + \Gamma_2 \log_{10} Diam + \Gamma_3 M_t \\ & + \Gamma_4 N_b + \Gamma_5 \log_{10} N_r + \Gamma_6 \alpha_{atm} r \\ & - 20 \log_{10} r + DI(\theta) \end{aligned} \tag{5.13}$$

where P_{br} is the engine power in kW, $Diam$ is the diameter of the propeller, N_b is the number of blades per propeller, N_p is the total number of propellers.

All in all, the variables of this model can be computed and used for coefficient optimization. The coefficient optimization can be performed through various optimization methods. The final product should be a reliable empirical model.

5.2. Conclusions

The objective of this research was to create the fundamental understanding of drone noise. Throughout the study, the spectral analysis of different UAVs was performed to determine how either design or operational parameters influence the generated noise. This work is done as a preamble to future studies related to drone noise modeling and imagining, in a world where UAV sighting are steadily increasing. With this unavoidable new infrastructure certainly being introduced in the next years to come, the understanding of drone noise is fundamental before the world actually starts experiencing the unpreventable.

In achieving this overall view on drone noise, measurements with UAVs from different categories are carried out. The drones were flown in various operations such as hover, fly-over or altitude changes. The appropriate time instances of each experiment were selected and the spectrograms and power spectral densities were investigated for each drone per maneuver. This step unravels the frequency ranges of interest which were further investigated through beamforming. While it is perceivable that drone noise is strongly characterized by non-negligible multipole sources due to the presence of rotors, several sophisticated multipole beamforming techniques were explored. In particular, Functional, Dipole, and Quadrupole Beamforming were implemented and verified via synthetic data. Subsequently, those are applied to real-life data on the frequency ranges determined from the spectral analysis. Lastly, the sound quality metrics of these time instances are computed and the contextual parameters are also observed, thus, leading to the selection of possible candidates for a future noise model. This results in a frequency range of interest, determination of noise sources strengths and locations on the drone, and values of the sound quality metrics for each maneuver.

The spectral analysis in all cases has shown dominant harmonics of the blade passage frequencies of the rotors in the lower frequency range (up to 3000 Hz). Above 3000 Hz, the broadband noise hinders the proper identification of noise sources, as is later proven with the application of beamforming techniques. Although a good performance of the sophisticated beamforming techniques was recognized on synthetic data, their accuracy greatly decreases when working with real-life measurements. Validation with synthetic data has shown that Functional Beamforming (FB) works best on a source if the correction for the type of source is given first. Thus, the qualities of FB will not be effective if it is applied as Monopole Functional Beamforming to a dipole source. Otherwise, the techniques gave values corresponding to the expected outputs (deviation $< 1\%$). With real-life data, CB still presents itself as the best technique to identify the sources, while the remaining beamforming methods do not perform as well. This can potentially be attributed to the multitude of external environmental and contextual factors, as well as the dependency of the Dipole Beamforming (DB) and Quadrupole Beamforming (QB) on the prior information on the multipole orientations on the rotors, which are generally unknown.

Beamforming analysis in two frequency ranges (0 to 3000 and 3000 to 7500 Hz) revealed that the clear noise sources are distinguishable in the lower frequency range and less on the higher. The higher frequency range appears noisy and the sources, including the whole drone, are unidentifiable.

All in all, when using CB, it has been noticed that between airframe and rotors, the latter prove to be the main sources of noise in hovering and increasing height from hover. The source identification becomes, however, unreliable when the drone's altitude varies due to the apparent motion in x-y of the drone (given that the drone is not perfectly located above the camera). Using the limited data set allowed nevertheless to suggest an empirical noise model, based on identified key operational parameters (distance and angle from drone to observer, thrust and velocity of the drone), as well as design and environmental variables.

The Sound Quality Metrics have also been calculated per maneuver. For each metric, a certain pattern has been observed. For example, Roughness and Tonality are dependent on the type of maneuver which is performed. Roughness is likely influenced by the temporal nature of the operation, while tonality is influenced by the difference in rotational speed of the vehicles. Concerning Fluctuation Strength, the harmonic peaks created by varying thrust give higher values of fluctuation. Lastly, regarding Sharpness, it has been observed that smaller drones exhibit pronounced higher frequency noise than bigger ones. This is potentially influenced by the rotational speed of the rotor, inversely proportional to the rotor diameter.

5.3. Recommendations

As a last step of this research, a set of recommendations were determined which could lead to future research topics. First of all, it is suggested to further develop these pole-dependent beamforming algorithms. A new promising beamforming algorithm has emerged in the time this research took place, which makes use of a modified Orthogonal Beamforming [42]. This new algorithm is built such that it can identify the correct location and strength of a varied amount of types of multipoles. A first unsuccessful attempt to implement this method has been made, however, due to time constraints the idea has been deserted.

In addition to this, further investigation into the higher frequency ranges (3000 to 7500 Hz) should be done, as this might expose interesting sources of noise. The bad resolution at this frequency range might be due to limitations of the measurement equipment. To test this issue, it would be recommended to further perform more experimental campaigns either using a different microphone array (preferably with more microphones in order to reduce the side lobes). Another issue for this poor performance at this frequency range might be due to the environment. It would be preferential to organize measurement campaigns in an ane-

choic room where the influencing external factors are not present. This controlled environment might help to verify the algorithm or test certain influencing parameters of the drone.

The measurement equipment may be also adjusted for reliable synchronization of the microphone array with the optical camera for enhanced beamforming. Furthermore, a synchronization of the drone position in three dimensional space with the data acquisition will yield a better understanding of drone noise characteristics at specific maneuvers.

With regards to a future noise model, a suggestion on potential parameters has been presented. The coefficients of such parameters can be reliably determined by performing sufficient measurements and basic optimization such as linear regression. This would result in a reliable empirical model to eventually predict drone noise for various types of drones and maneuvers.

Concerning the current psychoacoustic annoyance calculations, its calculation is built on an empirical basis and is formulated for aircraft noise. For drones however, it might not reflect the real human response, as the nature of these vehicles' noise is different. The exposure time of drones must be taken into consideration (for the cases of hovering and loitering around in one spatial position) such that the calculation can reflect the real human perception of drone noise. A suggestion to this adaptation would be applying more weight to the Roughness metric of the sound. Further experimental data will strengthen the interpretation of psychoacoustic metrics.

Bibliography

[1] Federal Aviation Administration. *UAS Sightings Report*. Tech. rep. 2019. URL: https://www.faa.gov/uas/resources/public_records/uas_sightings_report/.

[2] Airport Council International. "Drones Policy Paper". In: July (2018), pp. 1–10. URL: https://aci.aero/wp-content/uploads/2018/08/ACIPolicyPaper_Drones_2018.pdf.

[3] Andrew Christian and Randolph Cabell. "Initial investigation into the psychoacoustic properties of small unmanned aerial system noise". In: *23rd AIAA/CEAS Aeroacoustics Conference, 2017*. Apr. 2017. ISBN: 9781624105043. DOI: 10.2514/6.2017-4051.

[4] *Regulators and industry unite in need to address societal concerns on drones | EASA*. URL: https://www.easa.europa.eu/newsroom-and-events/press-releases/regulators-and-industry-unite-need-address-societal-concerns.

[5] UAV Systems International. *UAV Systems International | X8 Long Range Ready to Fly Drone*. URL: https://uavsystemsinternational.com/collections/fixed-wing-long-range-drones/products/x8-long-range-ready-to-fly-drone.

[6] Unmanned Systems Technology. *Airbus and Local Motors Launch Crowdsourced Commercial Drone Project | Unmanned Systems Technology*. URL: https://www.unmannedsystemstechnology.com/2016/04/airbus-and-local-motors-launch-crowdsourced-commercial-drone-project/.

[7] DJI. *DJI | Phantom 4*. URL: https://www.dji.com/nl/phantom-4%20https://www.dji.com/nl/phantom-4?site=brandsite&from=insite_search.

[8] Nicola Kloet et al. "Drone on: A preliminary investigation of the acoustic impact of unmanned aircraft systems (UAS)". In: *24th International Congress on Sound and Vibration, ICSV 2017*. March 2019. 2017, pp. 1–8.

[9] Stephen A. Rizzi et al. "Annoyance to noise produced by a distributed electric propulsion high-lift system". In: *23rd AIAA/CEAS Aeroacoustics Conference, 2017*. June. 2017, pp. 1–17. ISBN: 9781624105043. DOI: 10.2514/6.2017-4050.

[10] Umair Mehmood. *Development of an Audio Assessment Module (MSc Thesis)*. 2018.

[11] Hugo Fastl and Eberhard Zwicker. *Psychoacoustics: Facts and models*. Springer Berlin Heidelberg, 2007, pp. 1–463. ISBN: 3540231595. DOI: 10.1007/978-3-540-68888-4. URL: https://doi.org/10.1007/978-3-540-68888-4.

[12] Dick G. Simons. *Aircraft Noise and Emissions - Lecture Notes Course AE4431*. Delft University of Technology.

[13] Brian R. Glasberg and Brian C.J. Moore. "A model of loudness applicable to time-varying sounds". In: *AES: Journal of the Audio Engineering Society* 50.5 (2002), pp. 331–342. ISSN: 00047554.

[14] Birgitta Berglund and Thomas Lindvall. "Community noise. Archives of the Centre for Sensory Research." In: *Archives of the Center for Sensory Research* 2.1 (1995), pp. 1–195.

[15] Brian C.J. Moore. *An Introduction to the Psychology of Hearing*. Fifth Edit. Academic Press, 2003. ISBN: 0125056281. DOI: 10.1016/j.tins.2007.05.005.

[16] Aaron Hastings. "Sound Quality of Diesel Engines". PhD thesis. 2004, p. 393. ISBN: 9780496151721.

[17] Kenneth S. Brentner. "5 th Transformative Vertical Flight Workshop". In: (2018), pp. 1–17. URL: www.JobyAviation.com.

[18] Ana Alves Vieira, Fernando Lau, and Pedro Mort. "A New Computational Framework for UAV Quadrotor Noise Prediction". In: *5th CEAS Air & Space Conference* (Apr. 2015), pp. 1–14.

[19] Alexandru Dumitrache et al. "Design and Analysis Methods for UAV Rotor Blades". In: *Scientific Research and Education in the Air Force* 19.1 (2017), pp. 115–126. ISSN: 22473173. DOI: 10.19062/2247-3173.2017.19.1.48.

[20] Kenneth S. Brentner, Bolor E. Zolbayar, and Thomas F. Jaworski. “An investigation of noise from electric, low-tip-speed aircraft propellers”. In: *Proceedings of the AHS International Technical Meeting on Aeromechanics Design for Transformative Vertical Flight 2018*. August. 2018.

[21] Ana A. Vieira. *Helicopter Rotor Noise : Development of an Acoustic Software Tool (MSc Thesis)*. November. 2013.

[22] Daniel A. Russell, Joseph P. Titlow, and Ya-Juan Bemmen. “Acoustic monopoles, dipoles, and quadrupoles: An experiment revisited”. In: *American Journal of Physics* 67.8 (1999), pp. 660–664. ISSN: 0002-9505. DOI: 10.1119/1.19349.

[23] Roberto Merino-Martínez, Mirjam Snellen, and Dick G. Simons. “Functional beamforming applied to imaging of flyover noise on landing aircraft”. In: *Journal of Aircraft* 53.6 (2016), pp. 1830–1843. ISSN: 00218669. DOI: 10.2514/1.C033691.

[24] Triyambak Tripathy. “Acoustic Beamforming”. In: March (2017). URL: https://www.researchgate.net/publication/315695379_Acoustic_Beamforming.

[25] *Point Spread Function - acoustic-camera.com*. URL: https://www.acoustic-camera.com/en/support/frequently-asked-questions/knowledge-base/point-spread-function.html.

[26] Randolph Cabell, Robert Mcswain, and Ferdinand Grosveld. “Measured noise from small unmanned aerial vehicles”. In: *NOISE-CON Paper 20160010139* (2016), pp. 1–10.

[27] Nicola Kloet, Simon Watkins, and Reece A. Clothier. “Acoustic signature measurement of small multi-rotor unmanned aircraft systems”. In: *International Journal of Micro Air Vehicles* 9.1 (2017), pp. 3–14. ISSN: 17568307. DOI: 10.1177/1756829316681868. URL: https://doi.org/10.1177/1756829316681868.

[28] Teng Zhou and Ryu Fattah. “Tonal noise characteristics of two small-scale propellers”. In: *23rd AIAA/CEAS Aeroacoustics Conference, 2017* August (2017).

[29] Nikolas S. Zawodny and Douglas D. Boyd. “Investigation of rotor-airframe interaction noise associated with small-scale rotary-wing unmanned aircraft systems”. In: *Annual Forum Proceedings - AHS International*. 2017.

[30] Zebb Prime and Con Doolan. “A comparison of popular beamforming arrays”. In: *Annual Conference of the Australian Acoustical Society 2013, Acoustics 2013: Science, Technology and Amenity*. 2013, pp. 151–157. ISBN: 9781632662682.

[31] Parrot Official. *Parrot Mambo Fly | Parrot Store Official*. URL: https://www.parrot.com/global/drones/parrot-mambo-fly%20https://www.parrot.com/jp/doron/parrot-mambo-fly.

[32] Delft Dynamics. *Delft Dynamics | RH4 'Spyder'*. URL: https://www.delftdynamics.nl/?page_id=542.

[33] AceCore Technologies. *AceCore Technologies | NEO*. URL: https://acecoretechnologies.com/neo.html.

[34] Pieter Sijtsma. “Experimental techniques for identification and characterisation of noise sources”. In: *Advances in Aeroacoustics and Applications, VKI Lecture Series* (2004).

[35] Peter D. Welch. “The Use of Fast Fourier Transform for the Estimation of Power Spectra: A Method Based on Time Averaging Over Short, Modified Periodograms”. In: *IEEE Transactions on Audio and Electroacoustics* (1967). ISSN: 00189278. DOI: 10.1109/TAU.1967.1161901.

[36] Mirjam Snellen, Roberto Merino-Martínez, and Dick G. Simons. “Assessment of noise variability of landing aircraft using phased microphone array”. In: *Journal of Aircraft* (2017). ISSN: 00218669. DOI: 10.2514/1.C033950.

[37] Yu Liu et al. “Beamforming correction for dipole measurement using two-dimensional microphone arrays”. In: *The Journal of the Acoustical Society of America* 124.1 (2008), pp. 182–191. ISSN: 0001-4966. DOI: 10.1121/1.2931950.

[38] Salil Luesutthiviboon et al. “Improving source discrimination performance by using an optimized acoustic array and adaptive high-resolution CLEAN-SC beamforming”. In: *7th Berlin Beamforming Conference*. 2018.

[39] John William Strutt Lord Rayleigh. “XXXI. Investigations in optics, with special reference to the spectroscope”. In: *The London, Edinburgh, and Dublin Philosophical Magazine and Journal of Science* 8.49 (1879), pp. 261–274. ISSN: 1941-5982. DOI: 10.1080/14786447908639684.

[40] ISO. *Acoustics - Attenuation of sound during propagation outdoors – Part 1: Calculation of the absorption of sound by the atmosphere*. 1996. URL: https://www.iso.org/standard/17426.html.

[41] Robert D. Christ and Robert L. Wernli. "Underwater Acoustics". In: *The ROV Manual*. Elsevier Ltd, 2014, pp. 369–385. DOI: 10.1016/b978-0-08-098288-5.00014-2. URL: http://dx.doi.org/10.1016/B978-0-08-098288-5.00014-2.

[42] Xingjian Pan, Haijun Wu, and Weikang Jiang. "Multipole orthogonal beamforming combined with an inverse method for coexisting multipoles with various radiation patterns". In: *Journal of Sound and Vibration* 463 (2019), p. 114979. ISSN: 10958568. DOI: 10.1016/j.jsv.2019.114979. URL: https://doi.org/10.1016/j.jsv.2019.114979.

[43] European Commission. *Commission Delegated Regulation (EU) 2019/945 of 12 March 2019 on unmanned aircraft systems and on third-country operators of unmanned aircraft systems*. 2019. URL: http://data.europa.eu/eli/reg_del/2019/945/oj.

[44] Keith Attenborough. "Sound Propagation in the Atmosphere". In: *Handbook of Noise and Vibration Control*. 2008. ISBN: 9780471395997. DOI: 10.1002/9780470209707.ch5.

[45] Starlino Electronics. *Starlino Electronics | How much power is needed to hover?* URL: http://www.starlino.com/power2thrust.html.

A

Outlining Derivation of the Dipole Characteristic Term

A brief derivation is presented in [37]. Here, solutions to the convective wave equation for monopole and dipole sources are adapted from [37]. A more detailed derivation on this is given, building on solutions to the mentioned convective wave equations.

A.1. The Monopole Source

An ideal monopole is located at position $\mathbf{R}$ and immersed in a medium with a constant flow U. The acoustic pressure $p(\mathbf{x}, t)$ at the receiver $\mathbf{x}$ satisfies the following convective wave equation [34]:

$$\frac{1}{c^2}\left(\frac{\partial}{\partial t}+\mathbf{U}\cdot\nabla\right)^2 p(\mathbf{x},t)-\nabla^2 p(\mathbf{x},t)=-Q(t)\delta(\mathbf{x}-\mathbf{R}), \tag{A.1}$$

where c is the speed of sound in free field, $Q(t)$ is the monopole strength and $\delta(\mathbf{x}-\mathbf{R})$ is the Dirac delta function. One strategy to solve such a partial differential equation is to transform the equation into the frequency domain via a Fourier transform. Equation A.1 reads then:

$$\frac{1}{c^2}\left(i\omega+\mathbf{U}\cdot\nabla\right)^2 p(\mathbf{x},\omega)-\nabla^2 p(\mathbf{x},\omega)=-a(\omega)\delta(\mathbf{x}-\mathbf{R}), \tag{A.2}$$

where $a(\omega)$ is the Fourier transform of $Q(t)$. The solution in frequency domain is given in [37] as:

$$p(\mathbf{x},\omega)=\frac{-a(\omega)e^{-i\omega\Delta t_e}}{4\pi r\alpha}, \tag{A.3}$$

with $\alpha=\sqrt{(\mathbf{M}\cdot\mathbf{r}/r)^2+\beta^2}$, $M=\mathbf{U}/c$, a vector of mean flow Mach number, and $\beta=1-|\mathbf{M}|^2$. The emission time delay Δt_e appears which can be derived from the relations:

$$\begin{cases} t_r-t_e=\frac{\|\mathbf{r}_e\|}{c}=\frac{\|\mathbf{x}_0-\mathbf{R}_j+\mathbf{U}_e\|}{c} \\ \mathbf{r}=\mathbf{x}_0-\mathbf{R}_j+\mathbf{U}t_e+\mathbf{U}(t_r-t_e)=\mathbf{x}_0-\mathbf{R}_j+\mathbf{U}t_r \end{cases} \tag{A.4}$$

where t_r is the time at which the signal is received, t_e is the time where the signal is emitted, $\mathbf{x}_0$ is the origin of the microphone array, $\mathbf{R}_j$ is the microphone position vector and $\mathbf{r}$ is the updated distance of the moving source between the source and microphone at $\mathbf{R}_j$. By substituting $\mathbf{x}_0-\mathbf{R}_j$:

$$t_r-t_e=\frac{\|\mathbf{r}-\mathbf{U}(t_r-t_e)\|}{c} \tag{A.5}$$

Squaring and multiplying by the denominator, Equation A.5 becomes

$$\begin{aligned} c^2(t_r-t_e)^2 &= (\mathbf{r}-\mathbf{U}(t_r-t_e))\cdot(\mathbf{r}-\mathbf{U}(t_r-t_e)) \\ &= \|\mathbf{r}\|^2+\|\mathbf{U}\|^2(t_r-t_e)^2-2\mathbf{r}\cdot\mathbf{U}(t_r-t_e) \end{aligned} \tag{A.6}$$

Rearranging this equation yields:

$$\left(c^2 - \|\mathbf{U}\|^2\right)(t_r - t_e)^2 + 2\mathbf{r}\cdot\mathbf{U}(t_r - t_e) - \|\mathbf{r}\|^2 = 0 \tag{A.7}$$

The solution of this equation gives the final form of the delay time, by taking into account the $\mathbf{U} = \mathbf{M}c$ and $\beta^2 = 1 - \|\mathbf{M}\|^2$:

$$\Delta t_e = \frac{1}{c\beta^2}\left(-\mathbf{M}\cdot\mathbf{r} + \sqrt{(\mathbf{M}\cdot\mathbf{r})^2 + \beta^2|\mathbf{r}|^2}\right) \tag{A.8}$$

A.2. The Dipole Source

A dipole source can be modeled as two coherent monopole sources at a distance $\mathbf{d}$ from each other. For small d ($kd << 1$), the dipole strength can be expressed as $\mathbf{F} = -\nabla\cdot[\mathbf{D}(t)\delta(\mathbf{R})]$, where $\mathbf{D}(t) = Q(t)\mathbf{d}$ is the dipole strength vector. The convective wave equation is thus modified to:

$$\frac{1}{c^2}\left(\frac{\partial}{\partial t} + \mathbf{U}\cdot\nabla\right)^2 p(\mathbf{x},t) - \nabla^2 p(\mathbf{x},t) = -\nabla\cdot[\mathbf{D}(t)\delta(\mathbf{R})]\,. \tag{A.9}$$

Solving the equation analogously to the monopole case and transforming the solution back to the time domain [37], one arrives at:

$$p(\mathbf{x},t) = -\nabla\left[\frac{\mathbf{F}(t-\Delta t_e)}{4\pi r\alpha}\right] = -\left[\frac{\nabla(\mathbf{F}(t-\Delta t_e))}{4\pi r\alpha} + \frac{\mathbf{F}(t-\Delta t_e)}{4\pi}\nabla\left(\frac{1}{r\alpha}\right)\right] \tag{A.10}$$

The nominator of the first term is computed as:

$$\nabla(\mathbf{F}(t-\Delta t_e)) = \nabla(t-\Delta t_e)\frac{\partial\mathbf{F}(t-\Delta t_e)}{\partial t} = 0 - \nabla\Delta t_e = -\nabla\Delta t_e \tag{A.11}$$

and the derivative in the second term evaluates to:

$$\nabla\left(\frac{1}{r\alpha}\right) = -\frac{\nabla(r\alpha)}{r^2\alpha^2}. \tag{A.12}$$

This second term depends inversely quadratically on the distance between source and receiver and can thus be neglected in the far field. The solution to Equation A.9 reads then

$$p(\mathbf{x},t) = \frac{\nabla(\Delta t_e)}{4\pi r\alpha}\frac{\partial\mathbf{F}(t-\Delta t_e)}{\partial t}. \tag{A.13}$$

To derive an expression for $\nabla(\Delta t_e)$, the derivative is applied to the individual terms:

$$\nabla(\Delta t_e) = \frac{1}{c\beta^2}\left[-\nabla(\mathbf{M}\mathbf{r}) + \nabla\left(\sqrt{(\mathbf{M}\cdot\mathbf{r})^2 + \beta^2|\mathbf{r}|^2}\right)\right] \tag{A.14}$$

The first term is evaluated as

$$\nabla((\mathbf{M}\mathbf{r})(\mathbf{M}\mathbf{r})) = 2(\mathbf{M}\mathbf{r})\nabla(\mathbf{M}\mathbf{r}) = 2(\mathbf{M}\mathbf{r})\mathbf{M} \tag{A.15}$$

and the second term is computed as

$$\nabla\left(\sqrt{(\mathbf{M}\cdot\mathbf{r})^2 + \beta^2|\mathbf{r}|^2}\right) = \frac{2\nabla(\mathbf{M}\mathbf{r}) + \nabla(\beta^2)|\mathbf{r}|^2 + \beta^2\nabla\left(|\mathbf{r}|^2\right)}{2\sqrt{(\mathbf{M}\cdot\mathbf{r})^2 + \beta^2|\mathbf{r}|^2}} = \frac{\mathbf{M} + \beta^2\mathbf{r}}{2\sqrt{(\mathbf{M}\cdot\mathbf{r})^2 + \beta^2|\mathbf{r}|^2}} \tag{A.16}$$

where $\nabla(\beta^2) = 0$ and $\nabla\left(|\mathbf{r}|^2\right) = \nabla\left(\sqrt{x^2+y^2+z^2}\right) = (2x, 2y, 2z)^T = 2\mathbf{r}$. Equation A.14 then reads

$$\nabla(\Delta t_e) = \frac{1}{c\beta^2}\left[-\mathbf{M} + \frac{\mathbf{M} + \beta^2\mathbf{r}}{\sqrt{(\mathbf{M}\cdot\mathbf{r})^2 + \beta^2|\mathbf{r}|^2}}\right] = \frac{1}{c\beta^2}\left[-\mathbf{M} + \frac{\mathbf{M} + \beta^2\mathbf{r}}{r\alpha}\right] \tag{A.17}$$

Finally, to compare the monopole and dipole solution, we transform the dipole solution in Equation A.13 into the frequency domain:

$$p(\mathbf{x},\omega) = \frac{\nabla(\Delta t_e)}{4\pi r\alpha} i\omega a(\omega)\mathbf{d}e^{-i\omega\Delta t_e} = \frac{a(\omega)e^{-i\omega\Delta t_e}}{4\pi r\alpha}\left[i\omega\mathbf{d}\cdot\nabla(\Delta t_e)\right]. \tag{A.18}$$

The dipole characteristic term DPL is obtained as the ratio of Equation A.18 and Equation A.3:

$$DPL = -i\omega\mathbf{d}\cdot\nabla(\Delta t_e) \tag{A.19}$$

B

Contemporary UAV Legislative Measures

In May 2019, EASA released a first bill [43] on drone operations regulation. Part 13, entitled *Noise test code* lays the standards of measuring the emission of these vehicles and the usage of A-weighted sound power level. The measurements are to be done at with the drone positioned 0.5 m above the microphones. Categorization per class of the UAVs is done with respect to their size and weight. Table B.1 summarizes this classification.

Class	**MTOM (including payload) and Size**
C0	< 250 g
C1	< 900 g
C2	< 4 kg
C3	< 25 kg (or max size < 3 m)
C4	> 25 kg

Table B.1: UAV classes as defined by [43]

In Part 15, the maximum admitted sound power levels per class of UAV are stated (Table B.2). However, only the noise standards for C1 and C2 have been published at the moment. The values are given for L_{wa} which represents the Equivalent A-weighted sound level (also denoted in literature as $L_{\text{Aeq,Time}}$ or EAL). Equivalent A-weighted sound level (EAL), is a metric for assessing non-stationary noise signals, such as aircraft fly-overs and the effect of noise duration can be easily quantified.

$$L_{wa} = L_{\text{AE}} = 10\log\left[\frac{1}{T}\int_0^T 10^{\frac{L_{\text{A}}(t)}{10}}\,dt\right] \tag{B.1}$$

Where T is the integration time and $\text{L}_{\text{A}} = 10\log\sum_i 10^{\frac{\text{SPL}(i)+\Delta\text{L}_{\text{A}}(i)}{10}}$ is the overall A-weighted sound pressure Level (in [dBA]) with $\Delta_{\text{A}}(i) = -145.528 + 98.262\log f(i) - 19.509(\log f(i))^2 + 0.975(\log f(i))^3$ the A-weighted function for a frequency $f(i)$.

UAV class	MTOM, m in grams	Maximum sound power level L_{AE} in dBA		
		as from entry into force	as from 2 years after entry into force	as from 4 years after entry into force
C1	$250 \le m < 900$	85	83	81
C2	$900 \le m < 4000$	$85 + 18.5log_{10}\frac{m}{900}$	$83 + 18.5log_{10}\frac{m}{900}$	$81 + 18.5log_{10}\frac{m}{900}$

Table B.2: Maximum sound power levels per class (including transition periods) as admitted by [43]

In conclusion, it can be noted that there is a clear lack of regulations on drone noise. The rules are only created for the designing step of UAV, and less on the operational restrictions.

C

Data Tables of Measurements' Analysis

All measurements were analyzed and snapshots of the relevant time instances were selected. A total of 25 experiments were isolated for various maneuvers, drone or altitudes. These are detailed in Table C.1.

No.	Data file name	Frame Rate	Video Frame	Second [s]	Operation	Drone	z [m]
1	2019-09-10_14-31-21	6	172	28.67	Hover	Spyder	3
2	2019-09-10_14-31-21	6	361	60.167	Increase	Spyder	7.5
3	2019-09-10_14-31-21	6	438	73	Hover	Spyder	10
4	2019-09-10_14-31-21	6	483	80.5	Increase	Spyder	15
5	2019-09-10_14-31-21	6	528	88	Hover	Spyder	20
6	2019-09-10_14-31-21	6	585	97.5	Increase	Spyder	25
7	2019-09-10_14-31-21	6	636	106	Hover	Spyder	30
8	2019-09-10_14-31-21	6	927	154.5	Flyover Decrease	Spyder	25
9	2019-09-10_14-31-21	6	1134	189	Flyover Decrease	Spyder	15
10	2019-09-10_14-31-21	6	2025	337.5	Flyover	Spyder	10
11	2019-09-10_15-18-14	6	120	20	Flyover	Neo	59
12	2019-09-10_15-18-14	6	163	27.167	Flyover	Neo	60
13	2019-09-10_15-18-14	6	320	53.33	Flyover	Neo	61
14	2019-09-10_15-18-14	6	2300	383.33	Flyover	Neo	61
15	2019-09-10_15-50-54	12	78	6.5	Hover	Phantom	3
16	2019-09-10_15-50-54	12	342	28.5	Increase	Phantom	4
17	2019-09-10_15-50-54	12	426	35.5	Hover	Phantom	5
18	2019-09-10_15-50-54	12	642	53.5	Increase	Phantom	7.5
19	2019-09-10_15-50-54	12	702	58.5	Hover	Phantom	10
20	2019-09-10_15-50-54	12	822	68.5	Decrease	Phantom	7
21	2019-09-10_15-50-54	12	906	75.5	Hover	Phantom	4
22	2019-09-10_15-50-54	12	978	81.5	Fly-away	Phantom	4
23	2019-09-10_15-50-54	12	1086	90.5	Fly-over	Phantom	4
24	2019-09-10_15-50-54	12	1698	141.5	Fly-over FT	Phantom	4
25	2019-05-02_14-32-28	30	185	6.167	Flyover	Parrot	0.6

Table C.1: All 25 experiments considered for the analysis

D

Effects of Atmospheric Conditions

A pressure wave passing through a viscous medium, such as earth's atmosphere will experience attenuation of the high frequencies, as they lose more acoustic energy. The derivation of this appendix are heavily based on the calculations from [44] and validated by the standards from [40].

To quantify this attenuation, a loss factor, commonly denoted as α_{atm}, has been developed through semi-empirical means. This factor is used to correct the output SPL according to the correct atmospheric conditions (such as humidity, pressure and temperature) and frequency of interest.

The computation of α_{atm} is done through the relaxation frequencies of nitrogen, $f_{r,N}$, and oxygen, $f_{r,O}$, using $p_{ref,0}$ the reference pressure of 100kPa and p_{air} the air pressure at the time of the measurements as follows for nitrogen:

$$f_{r,N} = \frac{p_{\text{air}}}{p_{\text{ref},0}} \sqrt{\frac{T_0}{T_{\text{air}}}} \left(9 + 2.8 \cdot 10^4 \text{He}^{-4.17\left((T_0/T_{\text{air}})^{1/3}-1\right)}\right) \tag{D.1}$$

with T_{air} the temperature at the time of the measurements and T_0 the reference temperature of 293.16 K, and for oxygen:

$$f_{r,O} = \frac{p_{air}}{p_{ref,0}} \left(24.0 + 4.04 \cdot 10^6 \text{H} \frac{0.02 + 100H}{0.391 + 100H}\right) \tag{D.2}$$

with H the absolute humidity at the time of the masurments. This H can be computed as:

$$\begin{aligned} H &= \frac{10^{C_{\text{sat}}} RH p_0}{100 p_{\text{air}}} \\ \text{and } C_{sat} &= -6.8346 \left(\frac{T_{\text{sat}}}{T_{\text{air}}}\right)^{1.261} + 4.6151 \end{aligned} \tag{D.3}$$

using RH the relative humidity at the time of the measurements, p_0 as the standard atmospheric pressure equal to 101.325 kPa and the saturation constant (C_{sat}) equivalent to the saturation temperature ($T_{sat} = 273.16K$).

Inputting this into the below equation yield the atmospheric attenuation α_{atm} in natural logarithmic scale.

$$\alpha_{atm}(f) = f^2 \left(\left(\frac{1.84 \cdot 10^{-11}}{\sqrt{\frac{T_0}{T_{air}}} \frac{p_{air}}{p_0}} \right) + \left(\frac{T_0}{T_{air}}\right)^{2.5} \left(\frac{0.10680 e^{-3352/T_{air}} f_{r,N}}{f^2 + f_{r,N}^2} + \frac{0.01278 e^{-2239.1/T_{air}} f_{r,O}}{f^2 + f_{r,O}^2} \right) \right) \tag{D.4}$$

Correction in base-10 logarithmic scale can be done by multiplying the α_{atm} with the factor $\frac{20}{\ln 10}$ yielding an output of unit dB/m.

E

Derivation of the Engine Power

In this appendix, the derivation of the Engine Power dependent on thrust and velocity (thus only applicable for hovers) shall be explained. This is applicable only in hover because in this case it can be assumed that to keep a steady position in space, the Thrust (TR) must counteract the gravitational pull which is $TR = m \times g_{acc}$. The equations in this appendix are based on the findings of [45].

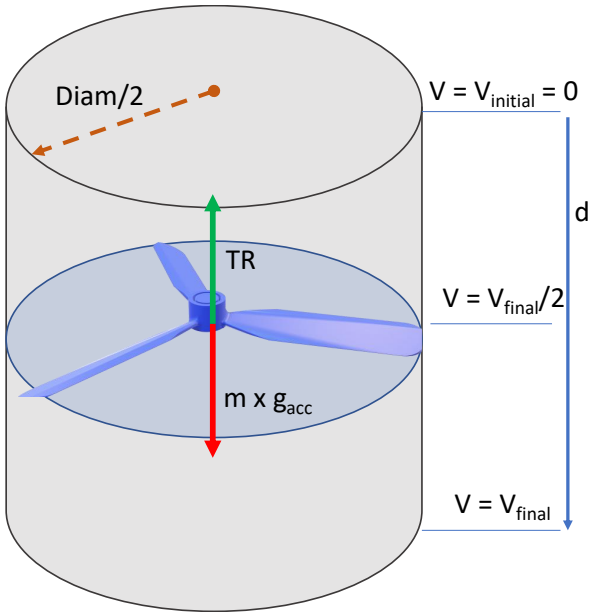

Figure E.1: Volume of airflow and the acting forces on a rotor adapted from [45]

Figure E.1 shows the forces acting on a moving rotor as well as the velocity of the air flow. The volume of this cylinder of air can be computed as:

$$Vol = \pi(Diam/2)^2 d = \pi(Diam/2)^2 Vt \tag{E.1}$$

where t is the period of time necessary for a particle to travel from the top to the bottom of the cylinder. Knowing the density of air ρ_∞, The mass of this volume of air is

$$m_{air} = \rho_\infty Vol = \rho_\infty \pi(Diam)^2 Vt \tag{E.2}$$

Since the air starts at $V_{initial} = 0$, its starting momentum is also zero, thus it's momentum change will be equal to final momentum $m_{air} \times V_{final}$, where V_{final} is the final speed. Using the theory of momentum conservation, the force applied on a mass is equal to the rate of change of momentum:

$$TR = \frac{m_{air} V_{final}}{t} = \frac{m_{air} 2V}{t} \tag{E.3}$$

The last two equations will yield:

$$TR = \frac{\rho_\infty \pi (Diam/2)^2 V t 2V}{t} = 2\rho_\infty \pi (Diam/2)^2 V^2 \tag{E.4}$$

Resulting in the equation for velocity:

$$V = \sqrt{\frac{TR}{2\rho_\infty \pi (Diam/2)^2}} \tag{E.5}$$

Next let's note that the power is equal to the rate at which work is done or in other words rate at which energy is consumed. Work is given by the formula $Work = Force * d$ (where d is the distance and Force is the acting force, in this case the thrust *TR*), thus power is $P_{br} = \frac{Work}{t} = \frac{TR \times d}{t} = TR \times V$:

$$P_{br} = TR \times V = TR \sqrt{\frac{TR}{2\rho_\infty \pi (Diam/2)^2}} = \sqrt{\frac{TR^3}{2\rho_\infty \pi (Diam/2)^2}} \tag{E.6}$$

Denoting $\eta = \sqrt{\frac{1}{2\pi\rho_\infty}}$, the resulting equation for the engine power becomes:

$$P_{br} = \eta \frac{TR^{3/2}}{Diam/2} \tag{E.7}$$